

# Magnetically Enhanced Microflow Cytometer for Bead-based Immunoaffinity Measurements in Whole Blood Samples



Scientific thesis for the attainment of the academic degree  
Master of Science (M.Sc.)  
of the Department of Electrical and Computer Engineering  
at the Technical University of Munich.

**Supervised by** Dr.-Ing. Mathias Reisbeck  
Prof. Dr. rer. nat. Oliver Hayden

**Submitted by** Johann Alexander Brenner  
Weisbergerstraße 5a  
85053 Ingolstadt  
03662733

**Submitted on** December 4<sup>th</sup>, 2020 at Munich





# Contents

<b>List of Abbreviations .....</b>	<b>0</b>
<b>1 Abstract .....</b>	<b>1</b>
<b>2 Theory .....</b>	<b>2</b>
2.1 Microfluidics .....	2
2.1.1 Incompressibility of Fluid Flows .....	2
2.1.2 Flow and Shear in Microchannels with Viscous Fluids .....	3
2.1.3 Force Equilibrium of Microbeads .....	5
2.1.4 Rolling Motion and Surface Interaction of Beads.....	11
2.2 Surface Chemistry .....	16
2.2.1 Surface Oxidation Methods.....	16
2.2.2 Silane Chemistry .....	19
2.2.3 Carbodiimide Crosslinker Chemistry .....	20
2.2.4 The Biotin-Avidin-System .....	23
2.3 Magnetoresistive Sensing .....	24
<b>3 Materials and Methods .....</b>	<b>27</b>
3.1 Magnetic Sensor Device .....	27
3.1.1 Assembly of Sensor.....	27
3.1.2 Design and Fabrication of Microfluidics .....	27
3.1.3 Peripheral Components and Optical Readout.....	30
3.2 Magnetic Beadometry .....	32
3.2.1 Bead Capture Assay .....	33
3.3 Surface Bio-Functionalization .....	33
3.3.1 Surface Activation.....	33
3.3.2 Chemical Surface Functionalization .....	34
3.3.3 Surface Bioconjugation .....	35
3.3.4 Particle Functionalization.....	36
<b>4 Results .....</b>	<b>40</b>
4.1 Virtual Prototyping of Cell Signals .....	40
4.1.1 Numerical investigation of immunomagnetic label density and size on quantitative magnetoresistive sensing of single cells and cell aggregates .....	40

4.1.2	Single Cell Signal .....	43
4.1.3	Cell Aggregates .....	45
4.2	The MRCyte Simulation Framework .....	47
4.2.1	Fluid Fields inside the Microchannel .....	47
4.2.2	Modelling the Force-Equilibrium of a Rolling Bead over a Biofunctionalized Surface .....	49
4.3	Reference Bead Surface Functionalization.....	51
4.3.1	Amine-Surface Biotinylation .....	51
4.4	Concentration Measurements in MRCyte.....	54
4.4.1	Measurement Error Sources and Calibration of Flow Field.....	57
4.4.2	Concentration Measurement in Diluted Whole Blood.....	60
4.4.3	Surface Magnetization of Biofunctionalized Beads .....	60
4.4.4	Count Stability.....	63
4.4.5	Differential Counting Setup .....	64
4.5	Surface Modification and Biofunctionalization of the Sensor Chip Substrate	69
4.5.1	Physisorption .....	69
4.5.2	Covalent Attachment.....	69
<b>5</b>	<b>Discussion.....</b>	<b>72</b>
<b>6</b>	<b>Outlook.....</b>	<b>75</b>
<b>7</b>	<b>Appendix .....</b>	<b>76</b>
<b>List of Figures</b>	.....	<b>87</b>
<b>List of Tables</b>	.....	<b>88</b>
<b>Bibliography</b>	.....	<b>89</b>
<b>Statement</b>	.....	<b>97</b>





# List of Abbreviations

## Symbols

$A$ - area .....
$C_{const}$ - linear fit correction factor.....
$C_{rr}$ - rolling resistance factor.....
$C_{velocity}$ - velocity correction factor.....
$Q$ - flow rate.....
$\chi$ - magnetic susceptibility.....
$\eta$ - dynamic viscosity.....
$\mu F$ - microfluidic .....
$\omega$ - angular rotation frequency .....
$\tau$ - surface stress tensor.....
$\tau_{pressure}$ - pressure stress tensor.....
$\tau_{viscous}$ - viscous stress tensor.....
$\varepsilon$ - shear stress tensor .....
$B$ - magnetic flux density.....
$\mathbf{F}_{buoyancy}$ - buoyancy.....
$\mathbf{F}_{drag}$ - Stoke's drag force .....
$\mathbf{F}_{el}$ - Coulomb's force.....
$\mathbf{F}_{grav}$ - gravity .....
$\mathbf{F}_{magnus}$ - Magnus lift force .....
$\mathbf{F}_{mag}$ - magnetic force .....
$\mathbf{F}_{protein}$ - protein-bond force.....
$\mathbf{F}_{saffman}$ - Saffman lift force.....
$\mathbf{F}_{shear}$ - shear-induced lift force .....
$\mathbf{M}$ - magnetization.....
$T_{crit}$ - critical tension.....
$\Omega$ - rotation vector .....
$\mathbf{m}$ - magnetic dipole moment .....
$\mathbf{u}$ - flow field.....
$\mathbf{u}_s$ - sedimentation velocity.....
$Re$ - Reynolds number .....

$Re_{particle}$	- particle Reynolds number.....
$\bar{u}$	- mean fluid velocity.....
$\vec{n}$	- unit outward normal .....
$\rho$	- density .....
$d_{GMR}$	- GMR bridge distance.....
$f_s$	- sampling frequency.....
$v_c$	- bead velocity.....

## A

AcOH	- acetic acid.....
adj. $R^2$	- adjusted coefficient of determination.....
$Al_2Ox_3$	- aluminium oxide.....
amine	- $-NH_2$ .....
APTES	- 3-triethoxysilylpropan-1-amine .....

## C

carboxamide	- $R_1-CONH-R_2$ .....
carboxyl	- $-COOH$ .....
CV	- coefficient of variance .....

## D

diH <sub>2</sub> O	- deionized water .....
DMSO	- dimethyl sulfoxide.....

## E

EDC	- 3-(Ethyliminomethyleneamino)-N,N-dimethylpropan-1-amine .....
EDTA	- 2,2',2'',2'''-(ethane-1,2-diyl)dinitrilo)tetraacetic acid.....
ethoxy	- $-O-CH_2-CH_3$ .....
EtOH	- ethanol .....

## F

FWHM	- full width at half maximum.....
------	-----------------------------------

## G

GMR	- giant magneto resistance .....
-----	----------------------------------

## H

H <sub>2</sub> O <sub>2</sub> - hydrogen peroxide .....
H <sub>2</sub> SO <sub>5</sub> - Caro's acid.....
H <sub>2</sub> SO <sub>4</sub> - sulfuric acid.....
HCl - hydrochloric acid.....
HF - hydrofluoric acid.....
hydroxyl - –OH.....

## I

IPA - isopropanol.....
------------------------

## K

K <sub>d</sub> - dissociation constant.....
---

## M

MACS - MACS running buffer.....
MeOH - methanol.....
MES - 2-(N-morpholino)ethanesulfonic acid.....
MEST - 2-(N-morpholino)ethanesulfonic acid (MES) buffer with Tween 20 .....
methylene - –CH <sub>2</sub> –.....
MFI - median fluorescence intensity.....
MFLI - multi frequency lock-in .....
MNP - magnetic nanoparticle.....
MR effect - magneto-resistive effect.....

## N

N <sub>2</sub> - nitrogen gas.....
NHS - 1-Hydroxy-2,5-pyrrolidinedione .....
NSE - Navier-Stokes-Equation .....

## O

O <sub>2</sub> - oxygen gas .....
-----------------------------------

## P

PAA - poly(acrylic) acid .....
PBS - phosphate buffered saline .....
PBST - phosphate buffered saline (PBS) with Tween 20 .....

PCB - printed circuit board.....  
PDMS - poly(dimethylsiloxane).....  
PE - phycoerythrin.....  
PEG - poly(oxyethylene).....  
piranha - a mixture from hydrogen peroxide with excess of sulfuric acid.....

## R

RBC - red blood cell.....

## S

SAM - self-assembled monolayer .....

SEM - standard error of the mean.....

$\text{Si}_3\text{N}_4$  - silicon nitride.....

silanol - Si–OH.....

siloxane - Si–O–Si.....

SNR - signal-to-noise ratio.....

sulfo-NHS - 1-hydroxy-2,5-dioxopyrrolidine-3-sulfonate.....

## V

$V_{pp}$  - peak-to-peak voltage.....  
 $V_p$  - peak voltage.....

## Z

z - approach .....



# 1. Abstract

## 2. Theory

The main measurement principle of a microfluidic channel in connection with a giant magneto resistance (GMR)-Sensor has been already described and characterized exhaustively by Helou [1], Reisbeck [2] and others.[3, 4] Therefore, this theoretical part will focus on (bio-)physical aspects of a cell rolling motion inside a microfluidic channel and surface modification chemistry.

### 2.1. Microfluidics

#### 2.1.1. Incompressibility of Fluid Flows

The main experiments of this work were carried out in microfluidic environments, which exhibit favorable properties compared to common macrofluidic systems. From a fluid-mechanical standpoint, shrinking the scales makes interfacial as well as electrokinetic phenomena much more significant, and reduces the importance of pressure and gravity.[5] However, electrodynamics, chemistry and fluid dynamics are inextricably intertwined, so that fluid flow can create electric fields (and vice versa), with a degree of coupling driven by the surface chemistry. Many of the resulting phenomena arise or can be explained by the conservation of mass described by the continuity equation (Eq. 1.1), the conservation of momentum described by the Cauchy-Momentum equation (Eq. 1.4), and the resulting Navier-Stokes equation(Eq. 1.8).

$$\frac{\partial}{\partial t} \iiint \rho \, dV = - \iint \rho \mathbf{u} \cdot \vec{n} \, dA \quad 1.1$$

$$\nabla \cdot \mathbf{u} = 0 \quad 1.2$$

$$\frac{\partial}{\partial t} \iiint \rho \mathbf{u} \, dV = - \iint \rho \mathbf{u} \mathbf{u} \cdot \vec{n} \, dA + \iint \boldsymbol{\tau} \cdot \vec{n} \, dA + \iiint \sum_i \mathbf{f}_i \, dV \quad 1.3$$

$$\rho \frac{\partial \mathbf{u}}{\partial t} + \rho \mathbf{u} \cdot \nabla \mathbf{u} = \nabla \cdot \boldsymbol{\tau} + \sum_i \mathbf{f}_i \quad 1.4$$

$$1.5$$

The foremost assumption in fluid dynamics is termed “incompressibility”, when density gradients are negligibly small to assume a uniformity thereof. This leads to a significant

simplification of the conservation equations, because any transfer from kinetic to internal energy can be ignored.<sup>1</sup> This equation states that the mass of a control volume (in this case the volume integral over the density ( $\rho$ )) can only change by the mass flux over its unit outward normal ( $\vec{n}$ ) transported by the flow field ( $\mathbf{u}$ ). For constant  $\rho$  the mass does never change over time. This finding and the application of Gauss's theorem yields the conservation of mass in an incompressible fluid. (Eq. 1.2)

### 2.1.2. Flow and Shear in Microchannels with Viscous Fluids

The final equation and Gauss's theorem can now be applied to the conservation of momentum relation. (Eq. 1.3) Integration yields then the Cauchy momentum equation which states that any change in momentum inside a control volume ( $\rho \frac{\partial \mathbf{u}}{\partial t}$ ) is caused by convective transport for or to the volume ( $\rho \mathbf{u} \cdot \nabla \mathbf{u}$ ), surface stresses ( $\nabla \cdot \boldsymbol{\tau}$ ), and the volumetric net body forces ( $\mathbf{f}_i$ ) such as gravity or electrostatics.

Hereby, the surface stress surface stress tensor ( $\boldsymbol{\tau}$ ) can be further decomposed into the pressure stress tensor ( $\boldsymbol{\tau}_{pressure}$ ) and viscous stress tensor ( $\boldsymbol{\tau}_{viscous}$ ) as shown in the equations Eq. 1.6. Characteristically, the pressure related contributions act normal and independently from  $\mathbf{u}$  whereas viscous forces act normal and tangential, and are dependent on  $\mathbf{u}$ . The  $\boldsymbol{\tau}_{pressure}$  can therefore be expressed by a scalar pressure acting in every spatial dimension which is spanned by the identity.

The viscous stresses however can not be described by a continuum equation but only by a constitutive relation of atomistic processes. The underlying fundamental model of Newton's mechanics assumes that dynamic viscosity ( $\eta$ ) is neither dependent on any velocity nor on the strain rate. Therefor, fluids which satisfy this condition are called "Newtonian fluids". Omitting special cases such as shear-thinning, -thickening or complex colloidal fluids such as undilute blood,  $\eta$  is the scalar proportionality that relates the strain rate to surface stress.[5] This is captured in the equation  $\boldsymbol{\tau}_{viscous} = 2\eta\boldsymbol{\epsilon}$ . Thereby, the shear stress tensor ( $\boldsymbol{\epsilon}$ ) is part of the decomposition of an unidirectional flow field. It resembles on the one hand side any stretching or squeezing of fluid by *extensional*

---

<sup>1</sup> For sake of completeness, it should be mentioned that viscous forces can also transfer energy irreversibly to internal energy. However, they are inversely proportional to the system's size, and hence omitted.

*strain* and on the other hand side *shear strain* which is responsible for skewing.[5]

$$\boldsymbol{\tau} = \boldsymbol{\tau}_{viscous} + \boldsymbol{\tau}_{pressure} = 2\eta\boldsymbol{\epsilon} - p\mathbf{I}_{3\times 3} \quad 1.6$$

$$\nabla \cdot \boldsymbol{\tau}_{viscous} = \nabla \cdot 2\eta\boldsymbol{\epsilon} = \nabla \cdot \eta \nabla \mathbf{u} \stackrel{\text{only if } \eta \text{ uniform}}{=} \eta \nabla^2 \mathbf{u} \quad 1.7$$

$$\underbrace{\rho \frac{\partial \mathbf{u}}{\partial t}}_{\text{Transient}} + \underbrace{\rho \mathbf{u} \cdot \nabla \mathbf{u}}_{\text{Convection}} + \underbrace{-\nabla p}_{\text{Pressure}} + \underbrace{\eta \nabla^2 \mathbf{u}}_{\text{Viscous}} + \underbrace{\sum_i \mathbf{f}_i}_{\text{Body Forces}} \quad 1.8$$

The divergence of  $\boldsymbol{\tau}_{viscous}$ , as used in the incompressible Cauchy momentum equation (Eq. 1.4), can then be simplified with Eq. 1.7 further by taking advantage of the anti-transpose symmetry of the flow field. If  $\eta$  is also uniform respectively isotropic across the channel, the divergence is completely independent of the scalar viscosity. Applying all assumptions to the Cauchy momentum equation (Eq. 1.4) yields as final result the Navier-Stokes-Equation (NSE). (Eq. 1.8)

However, the NSE has no analytic solution yet and can in consequence only solve defined boundary problems. The two most common boundary conditions herefore are the “no-penetration condition” ( $\mathbf{u} \cdot \vec{n} = 0$ ) and the “no-slip condition” ( $\mathbf{u}_t = \mathbf{u} - (\mathbf{u} \cdot \vec{n}) \vec{n} = 0$ ), which state that the normal and tangential components of fluid velocity are per definition zero at motionless, impermeable walls.

Besides these conditions, many problems arise due to turbulent flow and therefor transient effects. Mathematically, this can be avoided by simply neglecting the time-dependent term in the NSE. Also, it can be argued from a systematic point of view that, for viscosity-dominated flows, fluid moves in isoplanar “lamina”. In experimental observations, these laminar flows then proved to be steady to perturbations.

$$Re = \frac{\text{fluid density} \cdot \text{velocity} \cdot \text{size}}{\text{viscosity}} \quad 1.9$$

In a first order approximation, the dimensionless Reynolds number ( $Re$ ), which compares the inertia to viscous forces, allows a qualitative prognosis about the flow regime. (Eq. 1.9) If it results below a threshold of 2300, laminar flow can be assumed in Hagen-Poiseuille flows. This holds true for the utilized microfluidic with the dimensions 15 800  $\mu\text{m}$  x 700  $\mu\text{m}$  x 150  $\mu\text{m}$  (l x w x h) and aqueous buffer solutions, where the channel width considered as *characteristic size*. Hence, several fluidic phenomena such as deter-

ministic pathlines as well as simplifications of the NSE can be exploited in the present system.

In the model case of a flow through a rectangular channel, no analytical solution of the NSE exists, but a Fourier Series expansion if the width is larger than height of a channel as shown in Bruus [6]. Equation Eq. 1.10 determines the magnitude of the flow field parallel to the pressure gradient in relation to the horizontal dimension  $y$  and vertical dimension  $z$  with respect to the channel dimensions height  $h$  and width  $w$ . An integration over the flow field in the channel cross section yields the flow rate ( $Q$ ). (Eq. 1.11)<sup>2</sup>

$$\mathbf{u}_x(y, z) = \frac{4h^2\Delta p}{\pi^3\eta l} \sum_{n, odd}^{\infty} \frac{1}{n^3} \left( 1 - \frac{\cosh(n\pi\frac{y}{h})}{\cosh(n\pi\frac{w}{2h})} \right) \sin(n\pi\frac{z}{h}) \quad 1.10$$

$$Q = \int_{-\frac{1}{2}w}^{\frac{1}{2}w} \int_0^h u_x(y, z) \, dz \, dy \approx \frac{h^3 w \Delta p}{12\eta l} \left( 1 - \frac{h}{w} \right), \text{ for } h < w \quad 1.11$$

### 2.1.3. Force Equilibrium of Microbeads

Although microfluidic systems mostly operate in a low inertia regimes as specified by low  $Re$ , the force equilibrium  $\sum_i \mathbf{F} = 0$  and subsequently the velocity of any particle in the fluid stream is influenced as it moves closer to the boundaries. Several models have already been implemented with a part of the mentioned forces. Lee and Balachandar [7] compared the importance of translation, rotation and shear forces. Dong and Lei [8] evaluated cell rolling characteristics, and Wu and Voldman [9] proposed a model for bead-based immunoassays in microfluidics. Therefore, an overview over all (inter-)acting forces shall be given here.

$$Re_{particle} = \frac{r^2}{\frac{2wh}{w+h}} Re \quad 1.12$$

Additionally to the channel Reynolds number  $Re$ , describing the ratio between inertial force and viscous force of fluid in a flow, Di Carlo et al. [10] proposed a particle Reynolds number ( $Re_{particle}$ ) considering the size ratio of particle to channel. At  $Re_{particle} \ll 1$ ,

---

<sup>2</sup> The equation Eq. 1.10 shows that height deviations can have prominent influence on a channel velocity simulation as it is proportional to  $h^2$ . Further, the flow rate depends even on  $h^3$ .

particles are subjected to the dominant viscous drag to follow fluid streamlines. In the contradictory case, inertia becomes prominent. However, on increasing  $Re_{particle}$  to the order of 1, inertial lift forces become dominant and lateral migration of particles across streamlines becomes visible. For a micrometer sized bead and a channel as referred to in Sec. 2.1.2, the pre-factor is in the range of  $1 \times 10^{-5}$  to  $1 \times 10^{-7}$  hence viscous drag overweighs inertial lift of a particle.

### Stoke's Drag

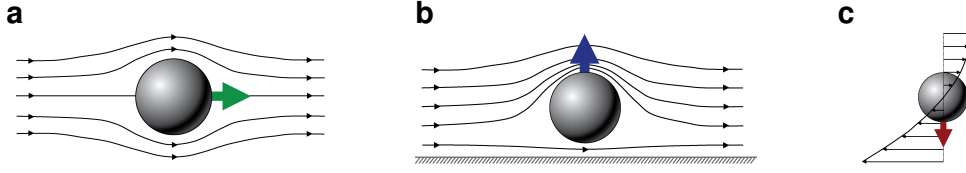


**Figure 1: Particle Drag and Lift Behavior**

(a) Bulk Drag: Force acts on a particle caused by the displacement of fluid stream lines. (b) Wall-lift Drag Force: In a special case of drag, where streamlines cannot be displaced further, a pressure gradient forms in front of the sphere. This forces a motion directed perpendicularly from the wall. (c) Shear-induced force: The curvature of the flow profile exhibits a translation and rotation due to inhomogeneously distributed shear on the surface.[11]

The foremost force to actuate particles inside a microfluidic channel is Stoke's drag force ( $\mathbf{F}_{drag}$ ). (Eq. 1.13) It originates from viscous fluid moving past the sphere surface, where a slip condition has to be applied. The fluid therefor has to displace its elements in front of the movement direction.[12] A particle with the surrounding streamlines is depicted in Fig. 1a for the bulk case and in Fig. 1c for adjacent walls.

$$\mathbf{F}_{drag,wall} = -6\pi\eta r \bar{\mathbf{u}} K \quad 1.13$$

$$K = \frac{4}{3} \sinh \alpha \sum_{n=0}^{\infty} \left( \frac{n(n+1)}{(2n-1)(2n+3)} \cdot A \right) \quad 1.14$$

$$\alpha = \cosh^{-1} \frac{z}{r}, \quad 1.15$$

$$A = \frac{2 \sinh((2n+1)\alpha) + (2n+1) \sinh 2\alpha}{(2 \sinh((n+0.5)\alpha))^2 - ((2n+1) \sinh \alpha)^2} - 1 \quad 1.16$$

$$K_{approx} = \frac{24}{Re} * \left( \frac{1 + \frac{2}{3}\lambda}{1 + \lambda} \right), \text{ with } \lambda = \frac{\eta_{fluid}}{\eta_{particle}} \quad 1.17$$

$$v_z = \frac{3}{64} Re_s \mathbf{u}_s = \frac{3}{64} \frac{\rho_{fluid} r \mathbf{u}_s}{\eta} \mathbf{u}_s, \left( \frac{\rho_{fluid} l_w \mathbf{u}_s}{\eta} \right) \ll 1 \quad 1.18$$

$$\omega = \frac{3\mathbf{u}}{32r} \left( \frac{r}{l} \right)^4 \left( 1 - \frac{3}{8} \frac{r}{l} \right), \text{ for } \left( \frac{r}{l} \right)^2 \ll 1 \quad 1.19$$

In the proximity of a channel wall, where no fluid can be displaced further, a correction factor was determined by Happel and Brenner [13] that approximates drag in a perpendicular direction.(Eq. 1.14) Repulsion velocity can then be defined by the Reynolds number calculated with a sedimentation velocity ( $u_s$ ) if the particle center has a distance  $l_w \ll 1$  from the wall.[14, 15] A phenomenological approximation of the correction factor yields equation Eq. 1.17, when viscosity dominates the difference. Adapted to an example, a spherical air-bubble inside a water flow feels only 67.4 % of the drag by surrounding fluid.

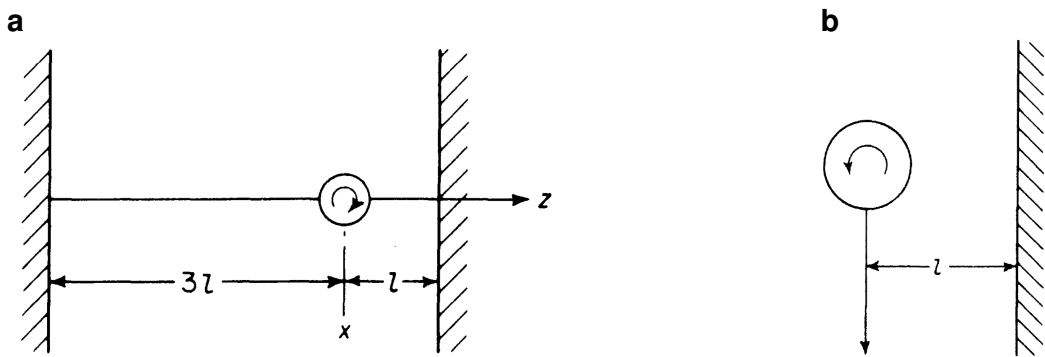


**Figure 2: Particle Rotation Behavior**

(a) Direction of rotation of a sphere settling in eccentric position between parallel walls. (b) Direction of rotation of a sphere settling in the presence of a single plane wall far from the other side.[10]

The considerations of Stoke's drag force above were limited for only linear translation cases. However, fluid drag also imposes a non-negligibly torque on particles if a particle moves nearer than 10 diameters to the wall. Happel and Brenner [13] mention an experimentally determined formula in 1.19 to calculate a drag-related angular rotation frequency ( $\omega$ ). Counter-intuitively, the direction of rotation in the bulk fluid (Fig. 2a) is opposite than from the rotation direction near or touching the wall (Fig. 2c). This can be explained by a complex superposition of tangential components from later mentioned forces and will not be explained to any more extent here.

### Gravity and Buoyancy

On every mass in our environment acts gravity ( $\mathbf{F}_{grav}$ ) to pull it along its gradient. In a medium, notwithstanding, it is balanced by the displacement of the same in the counter-direction called buoyancy ( $\mathbf{F}_{buoyancy}$ ). As a microparticle made from a co-polymer - especially when it carries magnetic momentum - has a significantly higher density than water,  $\mathbf{F}_{grav}$  (Eq. 1.21) outperforms  $\mathbf{F}_{buoyancy}$  (Eq. 1.20), which in term causes a particle

to sink to the channel floor.

$$\mathbf{F}_{buoyancy} = -\frac{4}{3}\pi r^3 \rho_{fluid} g \quad 1.20$$

$$\mathbf{F}_{gravity} = +\frac{4}{3}\pi r^3 \rho_{particle} g \quad 1.21$$

### Magnetic Force

The - during the course of this thesis - strongest acting force is exhibited by the magnetic flux density ( $\mathbf{B}$ ), which acts on paramagnetic particles with a magnetic dipole moment ( $\mathbf{m}$ ). When an external magnetic field is non-uniform, there will be a magnetic force ( $\mathbf{F}_{mag}$ ), proportional to the magnetic field gradient, acting on the magnetic dipole moment.(Eq. 1.24) For particles that carry magnetite or similar ferrimagnetic material in their polymer shell, the magnetic momentum can be inferred by the relation  $\mathbf{m} = MV$  if the magnetization ( $\mathbf{M}$ ) of a volume  $V$  is known. However, the more exact approach is a comparison of magnetic susceptibilities ( $\chi$ ) as described in Eq. 1.22. Consequently, if the particle susceptibility is greater than the fluid's, a microbead will move towards the field maximum. Calculated for an  $8 \mu\text{m}$  bead with  $1.12 \times 10^{-12} \text{ A m}^2$  saturation magnetization,  $\mathbf{F}_{mag}$  results in  $\sim 45 \text{ pN}$  for a field gradient of  $5 \text{ T m}^{-1}$ .

$$\mathbf{F}_{mag} = \frac{V_p (\chi_p - \chi_f)}{\mu_0} (\mathbf{B} \cdot \nabla) \mathbf{B} \quad 1.22$$

$$\mathbf{F}_{dipole} = (\mathbf{m} \cdot \nabla) \mathbf{B} = -\nabla \mathbf{E}_{dipole} \quad 1.23$$

$$\mathbf{E}_{dipole} = \sum_{i=1}^n \frac{\mu_0}{4\pi r_i^3} \left( \mathbf{m}_i \cdot \mathbf{m}_{ref} - \frac{3}{|\mathbf{r}_i|^2} (\mathbf{r}_i \cdot \mathbf{m}_i) (\mathbf{r}_i \cdot \mathbf{m}_{ref}) \right) \quad 1.24$$

Additionally, the magnetic beads interact with each other according to the dipolar interaction. In that case, a reference bead with magnetic momentum  $\mathbf{m}_{ref}$  at distance  $\mathbf{r}_{ref}$  feels the force of all surrounding particles. (Eq. 1.24)

### Electrostatic Interaction

The microchannel - as well as a particle in it - carries an electrical double layer on the surface due to present surface charges. The net charge acquired by the particles can be computed by integrating the particles' surface charge densities over their surfaces as described by Gauss's Law. However, as Coulomb's force ( $\mathbf{F}_{el}$ ) on charge  $q_1$

is square dependent of the distance from the secondary charge  $q_2$  at the respective locations  $\mathbf{r}_1$ ,  $\mathbf{r}_2$ . (Eq. 1.25) This, and the fact that the surface net charge in a buffer solution is insignificant, lead to the assumption that  $\mathbf{F}_{el}$  plays a minor role in this force equilibrium.

$$\mathbf{F}_{el} = \frac{q_1 q_2}{4\pi\epsilon_0} \frac{\mathbf{r}_1 - \mathbf{r}_2}{|\mathbf{r}_1 - \mathbf{r}_2|^3} \quad 1.25$$

### Magnus Lift Force

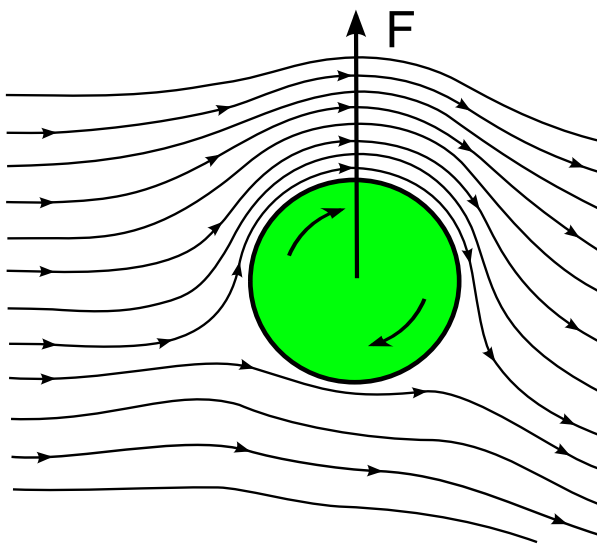


**Figure 3: Magnus Effect on a Particle in Laminar Flow**

The intrinsic rotation of a particle inside a laminar flow field causes a pressure gradient to the side whose tangential rotation vector is parallel to the stream lines.

The Magnus lift force ( $\mathbf{F}_{magnus}$ ) is a rotation-induced variable as a result of the pressure difference induced by streamline asymmetry.[16] For a spinning particle in a fluid as shown in Fig. 3, the streamline density and therefore the pressure on the one side of the particle is lower relative to the other side. The main driver of this effect is again the no-slip boundary, where fluid on the front side of the particle is dragged down whereas the fluid on the bottom side is slowed down. As a result, this leads to a lift force perpendicular to the flow direction.

$$\mathbf{F}_{magnus} = \frac{1}{8}\pi r^3 \rho_{fluid} (\mathbf{u} \times \boldsymbol{\Omega}) \quad 1.26$$

### Saffman Lift Force

When the rotation speed of a particle in shear rate direction is much greater,  $\Omega > 12\nabla\mathbf{u}$ , for a freely rotating particle Saffman lift force ( $\mathbf{F}_{saffman}$ ) will begin to act. Depending on the interaction of slip velocity and shear, it will counteract any movement to the planar surface. Hence, at high gradients the center of rotation causes a shift to the maximum shear.

Scaling with  $\omega$ , it will generally be at least one order of magnitude larger than Magnus force. Especially for electrically or magnetically actuated particles, shear-induced lift force ( $\mathbf{F}_{shear}$ ) is more relevant in the case of non-neutrally buoyant spheres.[16]

$$\mathbf{F}_{saffman} = \frac{81.2}{4}(\mathbf{u} - \mathbf{u}_p)r^2 \sqrt{\frac{\rho_{fluid}}{\eta} \nabla \mathbf{u}} \quad 1.27$$

### Shear-induced Lift Force

This  $\mathbf{F}_{shear}$  particles to migrate toward walls until the wall lift force repels and balances it. In contrast, if the curvature of  $\mathbf{u}$  is zero, it collapses to a simple shear flow. Then the pressure will be higher on the far from the center pushing particles to the centerline of channel. As shown in Fig. 1e the magnitude of  $\mathbf{u}$  in particle is much higher on the top side of particle than that on the bottom side, due to the parabolic nature of velocity profile. Similar to Saffman force, the dissymmetry of relative velocity causes a lower pressure on the wall side, generating a shear gradient lift force which is opposite to the Saffman force.[16]

$$\mathbf{F}_{shear} = K\rho_{fluid}(\nabla \mathbf{u})^2 r^4, \text{ with } K \text{ from Eq. 1.17} \quad 1.28$$

### Deformability-Induced Lift Force

Although solidity can assumed in the first order to the study of hydrodynamic behaviour of particles in a microchannel, cells and vesicles are not rigid but deformable. The deformability will induce an additional lift forces on the particles, which is perpendicular to the main streamline, and it is subjected nonlinearities caused by the matching of velocities and stresses at the deformable particle interface.

$$\mathbf{F}_{deformation} = \mu U r \left( \frac{r}{H} \right)^2 \frac{l_w}{H} f(\lambda) \quad 1.29$$

$$f(\lambda) = \frac{16\pi}{(\lambda+1)^3} \left[ \frac{11\lambda+10}{140} (3\lambda^3 - \lambda + 8) + \frac{3}{14} \frac{19\lambda+16}{3\lambda+2} (2\lambda^2 - \lambda - 1) \right] \quad 1.30$$

For example, deformability-induced lift force has been used already to separate and enrich malaria-infected red blood cell (RBC) from normal healthy RBC for the diagnosis of malaria. The parasite releases proteins that trigger the cross-linking of the spectrin network of the membrane, thus increases the rigidity of the infected cells.[17] Mach and Di Carlo [18] reported a parallelized microfluidic device that passively separates pathogenic bacteria from the diluted blood by the use a unique differential transit time due to channel height differences which in turn caused size-dependent inertial lift forces to obtain cell separation.

### **Fåræus and Fåræus-Lindquist Effect**

Often confused, the Fåræus and Fåræus-Lindquist effect constitute two different hemodynamic properties relevant for microfluidics with blood samples. Whereas the Fåræus effect states that RBCs are depleted in the wall regions of capillaries (due to the lift forces mentioned before), the Fåræus-Lindqvist effect describes the behavior of blood to decrease its viscosity in narrow channels.[19, 20] Thereby, the latter effect is not solely driven by the first, but also the Segré-Silberberg effect, who discovered that for neutrally buoyant particles an equilibrium at exact  $0.6r$  from a tubing center forms.[21] To model this effect, Chebbi [22] developed a cell-free marginal layer model.

#### **2.1.4. Rolling Motion and Surface Interaction of Beads**

A nice intro goes here

#### **Contact Area of a Sphere and Flat Surface**

Once the acting forces brought the bead in contact with a wall or the channel bottom, it starts to move forward in a rolling motion. In a simple model, rolling on a plane without slipping is constrained by a sphere's translation ( $\mathbf{F}_{||}$ ,  $\mathbf{F}_{\perp}$ ), rotation ( $\omega$ ), and shear. Nevertheless, due to the rigid nature of the sphere, any shear will be omitted in further models.[23] The no-slip boundary condition has to be applied also here by the require-

ment that the points of the sphere momentarily in contact with the plane are at rest. However, rolling contact problems are dynamic because the contacting bodies are continuously moving with respect to each other. The contact patch in a sliding problem continuously consists of the same particles. In contrast, particles enter and leave the contact area during rolling. Moreover, in a sliding problem the surface particles in the contact patch are all subjected the same tangential shift everywhere, whereas in a rolling problem the surface particles are stressed in different ways. During rolling, they are free of stress when entering the contact, then stick to a particle of the opposing surface, and are strained by the overall motion difference between the two bodies, until the local traction bound is exceeded and local slip sets in.[24]

In a real world, pressing two bodies with rough surfaces against each other limits the contact between the two bodies to a value, which is much smaller than the nominal contact area. Additionally, on natural and engineering surfaces Lennard-Jones potential, wetting, and molecular interactions start to play a role on the spectated microscale.[25]

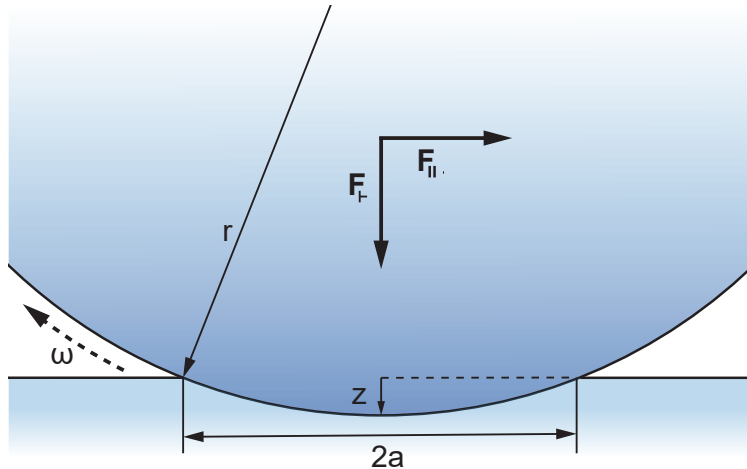


**Figure 4: Rolling Mechanics of a Sphere**

Penetration model of a sphere with radius  $r$  adapted from Azad and Featherstone [25] and Waters and Guduru [26]. The top body moves into the elastic bottom body for an approach ( $z$ ) and a contact area  $\pi a^2$ .

In reality, with elastic effects taken into consideration, a different situation occurs. If an elastic sphere is pressed onto an elastic plane (ideally of the same material), both bodies deform and a Hertzian pressure distribution arises. The center of the sphere is moved down by an approach ( $z$ ) as shown in Fig. 4 that can also be described as “maximum penetration distance”. It can now be calculated that the normal contact area between the bodies follows  $A_{contact} = \pi a^2 = \pi (2rz - z^2) = 2\pi rz (1 - \frac{z}{2r})$ . Assuming

that  $z \ll 2r$  and considering that  $A_{contact}$  must be zero for all  $z < 0$ , the following equation for the contact area arises. (Eq. 1.31) The spherical contact surface can be calculated analogous Eq. 1.32.[25]

$$A_{contact} = 2\pi r z, \text{ for } z \geq 0 \quad 1.31$$

$$S_{contact} = \pi r(2z + a^2) = \pi z(4r - z), \text{ for } z \geq 0 \quad 1.32$$

For a  $8\mu\text{m}$  microbead and a penetration depth  $z$  of  $100\text{ nm}$  this yields for example an interaction with  $6.84\%$  of the total sphere and a total area of  $13.753\mu\text{m}$ . Several methods and experiments have already been developed in the literature to measure the resulting friction and penetration parameters. A general model of a sphere in contact with a wall was optimized by Krishnan and Leighton [27]. Experimentally, Waters and Guduru [26] developed a microtribometer in PDMS to evaluate adhesion properties and validate their model's predictions.

### **Protein interaction during Rolling**

In the attempt to mimic rolling adhesion on vascular surfaces which is the first step in recruiting circulating leukocytes and other cells into the tissue, protein-protein-interactions as driver for microbead motions have been studied extensively in this thesis. Statistically, a cell flowing near the vessel wall is able to attach if its adhesion receptors contact ligands on the wall. Bond formation, anyhow, involves distinct steps: transport, which brings two molecules into close proximity, and reaction, during which the molecules dock. Faster cell velocity produces more collisions but also limits the interaction time between interaction molecules. Thus, the relative timescales for transport and docking affect the efficiency of tethering a flowing cell to the surface.[28]

For these properties, Dembo et al. [29] developed a detailed physical description of membrane adhesion and detachment kinetics. Wu and Voldman [9] then proposed an integrated model for bead based rolling mechanisms under the influence of protein interaction. The key for interaction thereby is the specific *affinity* respectively *avidity* of the protein and its ligand. In general, high-affinity ligand binding results from greater attractive ligand-receptor-forces and results in a higher tenancy of the receptor. However,

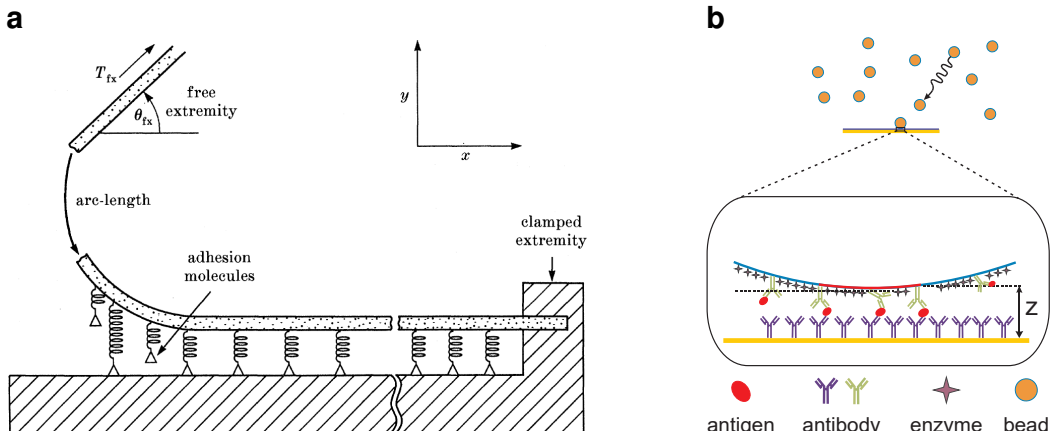


**Figure 5: Membrane Adhesion and Detachment Models**

a Adhesion Model after Dembo et al. [29]: Every interaction is viewed as spring-damper-model in superposition. b Surface Coverage Assay Model: In a stochastic approach, analyte molecules and their interactions are modeled between a planar and a spherical surface. Adapted from Wu and Voldman [9]

lifetime of a formed complex does not correlate. The net ligand affinities are unitized by the dissociation constant ( $K_d$ ), which relates the reverse reaction rate ("the dissociation of the bond") to the forward reaction rate ("the formation of the bond"). Therefore high-affinity results in low  $K_d$ .

On a bead and microchannel surface, however, not only one but multiple protein-ligand complexes are formed and dissociated simultaneously. This is described by *avidity*. Through single binding events elevate the likelihood of other interactions, avidity is not relating the sum of its ingredient affinities but can rather be seen as the combined effect of all affinities participating in the biomolecular interaction.[30]

Main factor for the method in this thesis is now the critical tension ( $T_{crit}$ ). A particle - cell or bead - flowing in a low-Reynolds number environment, experiences a  $F_{shear}$  and a torque rotation vector ( $\Omega$ ), which both reach maximum when the particle stops. For this, the two forces must be counteracted by a tensile force on the adhesive bonds and a compressive force at the bottom of the particle. Moreover, these forces affect the forward and reverse reaction rates of the bonds. Any rolling motion stops when the adhesion can withstand the force required to counteract the maximal other forces. After break-up of these bonds the particle begins to accelerate downstream until a newly formed bond develops sufficient strength. Consequently, the intrinsic mechanics of these bonds and how their respective off-rates act under force critically determines whether and how bead roll in a flow field.[28]

There exist two distinct bond types that take effect during the above processes: *Slip*

*bonds* are linkages whose lifetime is shortened to some extent by external force whereas *catch bonds* lock more tightly upon deformation stress.

In biological systems, for example selectines, another effect arises. Upon increasing external stress, bond lifetimes with the ligand are first prolonged until a threshold where bonds are starting to decease. In contrast, if an antibody is the ligand only slip bonds are formed in response to force.[31, 32] By studying the exact forces acting on a particle-protein interaction system affinity based sorting and ultrasensitive assays can be established.[33]

## 2.2. Surface Chemistry

Introducing biological samples, such as peripheral whole blood and -plasma, into microsystems needs careful consideration of surface modification compared to buffered samples of adjusted pH containing cells or polymeric beads. Blood-material contact most often initiates surface-mediated reactions that lead to cell activation, blood clotting or biofilm formation.[34, 35] In order to minimize unspecific interactions on surfaces, most contact faces are passivated with chemically and biologically inert materials or even composed entirely from it. In any use case, where a surface has to be functionalized with biomolecules, the intrinsic inertness then requires specialized methods for permanent and reproducible adhesion.[36, 37]

Molecules can be immobilized through various mechanisms on surfaces to achieve a biological or chemical functionality. The most simple is physisorption. Here, a biomolecule is bonded only by weak electrostatic, van-der-Waals or dipole-dipole interaction with a adsorption enthalpy below  $50 \text{ kJ mol}^{-1}$ .[37] In contrast, this yields fast reaction rates, because no activation energy has to be overcome. Although a large number of molecules can be captured with this method, several drawbacks have been identified.[38–41] Therefore, most functionalization approaches rely on chemisorption where molecules are covalently bound to a surface. Due to the higher activation energy barrier this bonding mechanism works slower in comparison to physisorption, though higher temperatures or catalysts can promote an equilibrium. One of the most well-known strategies to bring reproducible thin films on surfaces is the formation of self-assembled monolayers (SAMs) where a dense layer of single molecules with high internal order forms upon dipping into a surface-active substance.[42]

### 2.2.1. Surface Oxidation Methods

Modifying a surface with functional silanes, requires oxidized sites, for example  $-\text{OH}$  (hydroxyl) resp.  $\text{Si}-\text{OH}$  (silanol) groups. In order to increase the presence of those reactive groups on substrates, various activation methods such as a mixture from hydrogen peroxide with excess of sulfuric acid (piranha) and sulfuric acid ( $\text{H}_2\text{SO}_4$ ), oxygen gas ( $\text{O}_2$ ) - plasma treatment or an hydrofluoric acid (HF) dip can be chosen.[43]

Critical for any surface engineering is the internal structure and in consequence the binding energies of the surficial groups. The three mainly used substrates in this work,

glass, poly(dimethylsiloxane) (PDMS) and silicon nitride ( $\text{Si}_3\text{N}_4$ ), contain highly conserved, homogeneous surfaces and are mostly well characterized. The surface of glass exhibits already silanol groups intrinsically and consequentially demands only a removal of impurities. PDMS and  $\text{Si}_3\text{N}_4$  however have different compositions as shown in Fig. 6 and ?? hence requiring a strong oxidation agents to completely exchange its interface to hydroxyl.[44–46]

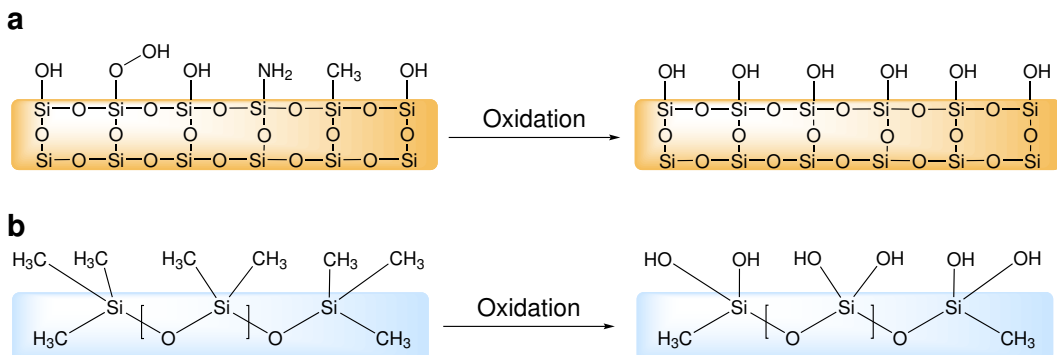
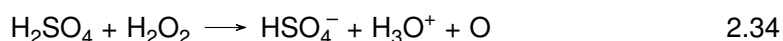
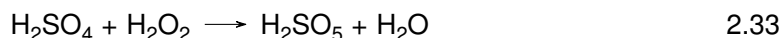


**Figure 6: Different Substrate Surfaces: Glass, PDMS and  $\text{Si}_3\text{N}_4$**

Surface groups and internal structure of quartz glass (a), PDMS (b), and silicon nitride (c). After an oxidation step, the methyl groups are converted to hydroxyl.

### Piranha Solution

Piranha is an oxidizer composed of hydrogen peroxide ( $\text{H}_2\text{O}_2$ ) and  $\text{H}_2\text{SO}_4$ , typically in volume ratios between 1:3 and 1:7. The effectiveness of piranha in removing organic residues and creating hydroxyl groups is induced by two distinct processes. First, hydrogen and oxygen are removed as units of water by the concentrated  $\text{H}_2\text{SO}_4$  in a comparably fast process.( Eq. 2.33) This occurs due to the thermodynamically favorable reaction with an enthalpy of  $-880 \text{ kJ mol}^{-1}$  and produces Caro's acid ( $\text{H}_2\text{SO}_5$ ), one of the strongest oxidants known.[47]



Second, the sulfuric acid boosts hydrogen peroxide from a mild oxidizer into the more aggressive atomic oxygen by the dehydration of  $\text{H}_2\text{O}_2$ . (Eq. 2.34) These two dehy-

dration processes result on the one hand in a highly corrosive nature against organic materials, particularly against the difficult to remove carbon. On the other hand, it is strongly acidic and oxidizing.

### **Hydrofluoric Acid**

One of the substrates used in this work is  $\text{Si}_3\text{N}_4$  as passivation layer above magnetic sensors as it has a significant better diffusion barrier against water or sodium ions and is chemically inert.[48] However, due to its complex crystal structure it is also difficult to modify by common chemicals and the exact surface composition still subject to scientific discussion.[49] Apart from cleaning the surface with piranha, few other modification methods have been reported, but only one suitable for the direct generation of hydroxyl groups.[42, 49–51]

As depicted in Fig. 6, the reaction  $\text{Si}-\text{OH} + \text{HF} \leftrightarrow \text{Si}-\text{F} + \text{H}_2\text{O}$  takes place reversibly due to the coincidence that  $\text{Si}-\text{O}$  and  $\text{O}-\text{H}$  as well as  $\text{Si}-\text{F}$  and  $\text{H}-\text{F}$  bonds have similar binding energies. Hence, the forward and reverse reactions require a low activation energy. After Le Chatelier's principle, a depletion of HF in the bulk leads then to an increase in surficial hydroxyl groups.[52] It was revealed that an oxidation with a similar protocol based on aqueous HF yields a variable  $\text{Si}-\text{O}-\text{Si}$  (siloxane) coverage with  $37 \pm 17\%$  of a monolayer, which can be used for stable, covalent attachment of silanes. Nominally, the same surface coverages of silicon oxide and nitride surfaces could be achieved by ethoxy- and chlorosilanization.[53] As shown by Gustavsson et al. [54], the subsequent surfaces exhibit beneficial biological properties and can be modified by further standard procedures.

### **Oxygen Plasma**

Apart from wet chemistry methods, the exposure of a surface to oxygen plasma yields hydroxyl groups as well. In a plasma chamber, a low-pressure gas is irradiated by kHz to MHz waves to excite and ionize its atoms. In consequence, the UV-radiation emitted by the gas can photolyse typical organic bonds and remove surface contaminations. Additionally, reactive oxygen species such as  $\text{O}_2^+$ ,  $\text{O}_2^-$ ,  $\text{O}_3$  or  $\text{O}$  oxidize the surface or bind dissociated components with low vapor pressure. During an evacuation in the process, these molecules are removed from the chamber intrinsically.[55]

## 2.2.2. Silane Chemistry

By the use of silane chemistry a surface is rendered organofunctional with alkoxy silane molecules. Since glass, silicon, alumina, titania, and quartz surfaces, as well as other metal oxide interfaces, are rich in hydroxyl groups, silanes are particularly useful for modifying these materials.[56]

The general formula for a silane coupling agent (Fig. 7a) typically shows the two classes of functionality. X is a hydrolyzable group typically alkoxy, acyloxy, halogen or amine.

Following hydrolysis, a reactive silanol group is formed, which can condense with other silanol groups to form siloxane linkages. (Fig. 7) Stable condensation products are also formed with other oxides such as those of aluminum, zirconium, tin, titanium, and nickel. Less stable bonds are formed with oxides of boron, iron, and carbon, whereas alkali metal oxides and carbonates do not form stable bonds with siloxanes at all. The R group (Fig. 7a) is a nonhydrolyzable organic radical that may possess a functionality that imparts desired characteristics. One of the more common silanes is 3-triethoxysilyl-propan-1-amine (APTES), where the X group consists of an  $-\text{O}-\text{CH}_2-\text{CH}_3$  (ethoxy) group, the organic rest R is substituted by an  $-\text{NH}_2$  (amine) and the 3  $-\text{CH}_2-$  (methylene) groups alter n to 3.[57]

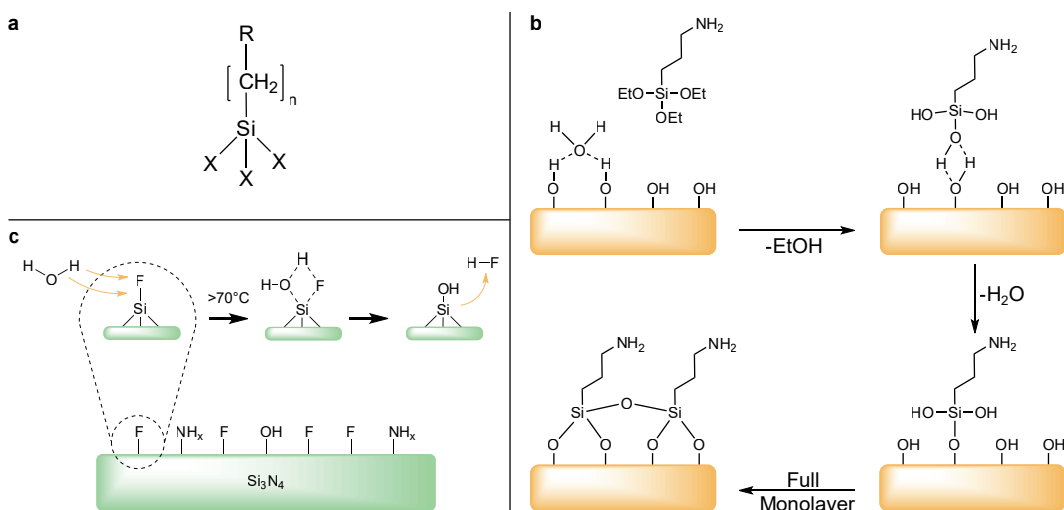


**Figure 7: Surface Oxidation and Modification by APTES**

(a) Structure of a typical trialkoxysilane, X: hydrolyzable group, R: non-hydrolyzable organic radical, n: methylene chain-length. (b) Before the condensation reaction, the oxidized surface has formed hydrogen bonds with water molecules while the silane molecules are in the bulk solution. The hydrolyzed silanol group adsorbs onto the surface and forms hydrogen bridges with the silicon bound oxygen atom. In a condensation reaction, under the loss of water, a covalent bond to the surface forms. After the SAM assembly the surface is saturated with a covalent-bound, crosslinked silane film.[58] (c) Proposed oxidation of  $\text{Si}_3\text{N}_4$  with HF: Due to similar activation energies water can displace HF in a competitive manner effectively above a temperature above 70 °C.

The final result of reacting an organosilane with a substrate ranges from altering the adhesion characteristics, catalyzing chemical transformation at the heterogeneous interface, ordering the interfacial region, and modifying its partition characteristics. Significantly, it includes the ability to effect a covalent bond between organic and inorganic materials. Especially in optical or biological sensors, silane modifications open a broad range of applications.[42, 59, 60]

However, the silanization reactions bear a few drawbacks which are often neglected. For instance, silane chemistry is strongly temperature and pH-dependent.[61, 62] Further, in a process to build SAMs from APTES, the reaction must be catalyzed by water. But already small changes in the water content cause dramatic deviations in layer thickness.[63] Additionally, silanes can crosslink to themselves through side reactions. (Fig. 7b) [64]

### **2.2.3. Carbodiimide Crosslinker Chemistry**

By APTES amine-terminated films form the basis of many reactions and open the possibility to various applications, such as the direct attachment of biofunctional molecules by carbodiimide crosslinking chemistry.[65] Here,  $-COOH$  (carboxyl) groups are modified by 3-(Ethyliminomethyleneamino)-N,N-dimethylpropan-1-amine (EDC) and 1-Hydroxy-2,5-pyrrolidinedione (NHS) to form a stable secondary  $R_1-CONH-R_2$  (carboxamide) bond with any primary amine.

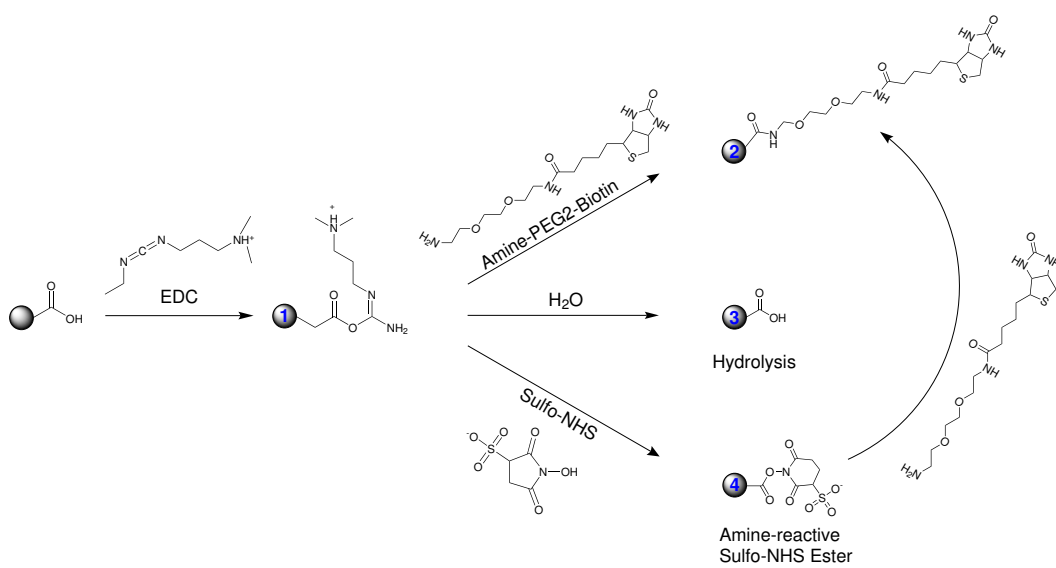


**Figure 8: Carboxyl bead modification with EDC/NHS**

The carboxyl groups on the bead are activated with EDC to an active O-acylisourea intermediate. This can then either be nucleophilically attacked by a primary amine of the amine-PEG<sub>2</sub>-biotin reactant or - due to its instability - hydrolyzed back to a regenerated carboxyl surface. A present NHS-ester can also displace the O-acylisourea to form a considerably more stable intermediate which then itself reacts with any primary amine.

The general reaction mechanism is depicted in Fig. 8 for the example of a particle surface, but it can equivalently be applied to any other modified surface or molecule. The initial carboxyl group is esterified by EDC to an active o-acylisourea intermediate and leaves rapidly upon nucleophilic attack of an amine with release of an iso-urea byproduct. A zero-length amide linkage is formed. (Fig. 8, 1->2) Sulphydryl and hydroxyl groups also will react with such active esters, but the products of such reactions, thioesters and esters, are relatively unstable compared to an carboxamide bond. (Fig. 8, 1)[65]

However, this reactive complex is slow to react with amines and can hydrolyze in aqueous solutions. If the target amine does not find the active carboxyl before it hydrolyzes (Fig. 8, 3), the desired coupling cannot occur. This is especially a problem when the target molecule is in low concentration compared to water, as in the case of protein molecules. Notwithstanding, forming a NHS ester intermediate from the reaction of the hydroxyl group on NHS with the EDC active-ester complex increases the resultant amide bond formation remarkably. (Fig. 8, 4->2) [66]

Another critical point in carbodiimide chemistry is the solubility of the compounds. EDC, NHS and 1-hydroxy-2,5-dioxopyrrolidine-3-sulfonate (sulfo-NHS) are soluble in aqueous and organic solvents. Nevertheless, activation with non-sulfonate NHS decreases water-solubility of the modified carboxylate molecule, while activation with sulfo-NHS preserves or increases its water-solubility by virtue of the charged sulfonate group.[67]

## 2.2.4. The Biotin-Avidin-System

Until now, the interaction of the homotetrameric protein avidin and its ligand biotin forms one of the strongest known non-covalent bonds in biological systems characterized by a  $K_d$  in the range of  $10^{-15}$  M.[68] First isolated from chicken egg white, it became a standard to use in biotechnology when researchers found a similar bacteria protein - streptavidin - in *Streptomyces* strains.[69] However, the charged glycoprotein avidin exhibits unspecific binding in some assays in comparison to streptavidin. Therefor, several companies developed deglycosylated forms of avidin with a neutral isoelectric points to minimize unspecificity. (NeutrAvidin, Extravidin, NeutraLite) In recent studies, a mutant streptavidin called "Traptavidin" exhibited an even 10 times dissociation rate.[70] As discovered in the early 1990s, biotin is bound inside a highly stable  $\beta$ -barrel structure, and stabilized by hydrogen bonds and van der Waals forces.[71] In a unique mechanism, a side group of biotin (valerate) binds to a neighboring monomer of streptavidin and therefor stabilizes the dimer complex intrinsically.[72, 73] From a thermodynamical point-of-view, the interaction of the vitamin and protein is described by a total free binding energy of  $300\text{ kJ mol}^{-1}$  to  $330\text{ kJ mol}^{-1}$  for a tetrameric protein.[73] All these aspects lead to a significant rupture force for the biotin-release of  $250\text{ pN}$ .[74]

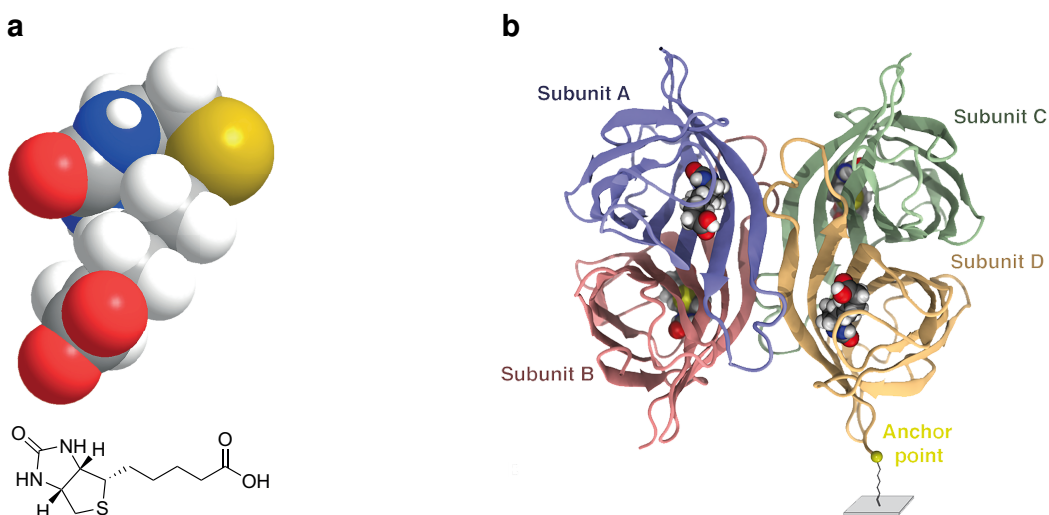


**Figure 9: Functional Structures of Biotin and Streptavidin**

(a) Two- and three dimensional chemical structure of the biotin molecule. (b) Homotetrameric streptavidin with four subunits and four bound biotin-ligands. The molecule is attached with the anchor point at one terminus to a surface.[75]

### 2.3. Magnetoresistive Sensing

The measurement system's main component is a GMR-sensor stack with a measured magnetoresistive effect of ~8 %. GMR is a quantum mechanical magnetoresistance effect observed in multilayers composed of alternating ferromagnetic and non-magnetic conductive layers. The driving factor for this resistance is anisotropy of a soft ferromagnetic layer. Two ferromagnetic layers with a thin conducting, non-magnetic spacer in the center build the base of the GMR stack.[76] One ferromagnetic layer has a so called pinned magnetization by exchange coupling, which is insensitive to outer magnetic fields. The second, "easy" layer is soft magnetic. Hence, it modulates its orientation in dependence to small coercive forces. [77]

In the case if both layers are aligned parallel, applying a current to the sensor allows majority charge carriers to pass through the layers with less impact into electrons on either sides. Accordingly, the overall resistance is low compared to another extremum in the antiparallel alignment. The magnetization direction can be controlled, for example, by applying an external magnetic field.[78, 79]

In the present system, GMR stacks were used in a Wheatstone configuration, where two bridges act as a reference for bridge balancing. In front of the sensor, nickel-based chevron patterns act as pre-enrichment for magnetic particles. These structures are driven by an external permanent magnet hence imposing a high flux density gradient on particles. Above these patterns, previously mentioned  $\text{Si}_3\text{N}_4$  passivation has been deposited in various thicknesses to achieve inertness. On top of the sensor chip, a straight microfluidic channel is mounted to execute flow cytometry experiments.[80, 81]

In order to measure the change in resistance sensitively, the lock-in principle is used. Here, an amplifier extracts signals in a defined frequency band around a reference frequency. This efficiently filters all other frequency components. Thereby a lock-in amplifier performs a multiplication of its input  $V_s(t)$  with a reference signal  $V_r(t)$  and low-pass filters the result  $Z(t)$ . In most integrated cases, the reference signal is generated additionally by the lock-in amplifier itself. Using a pure sine wave as reference enables a selective measurement at the fundamental frequency or its harmonics.[82]

At a measurement,  $V_s(t)$  is split and separately multiplied with the reference signal and

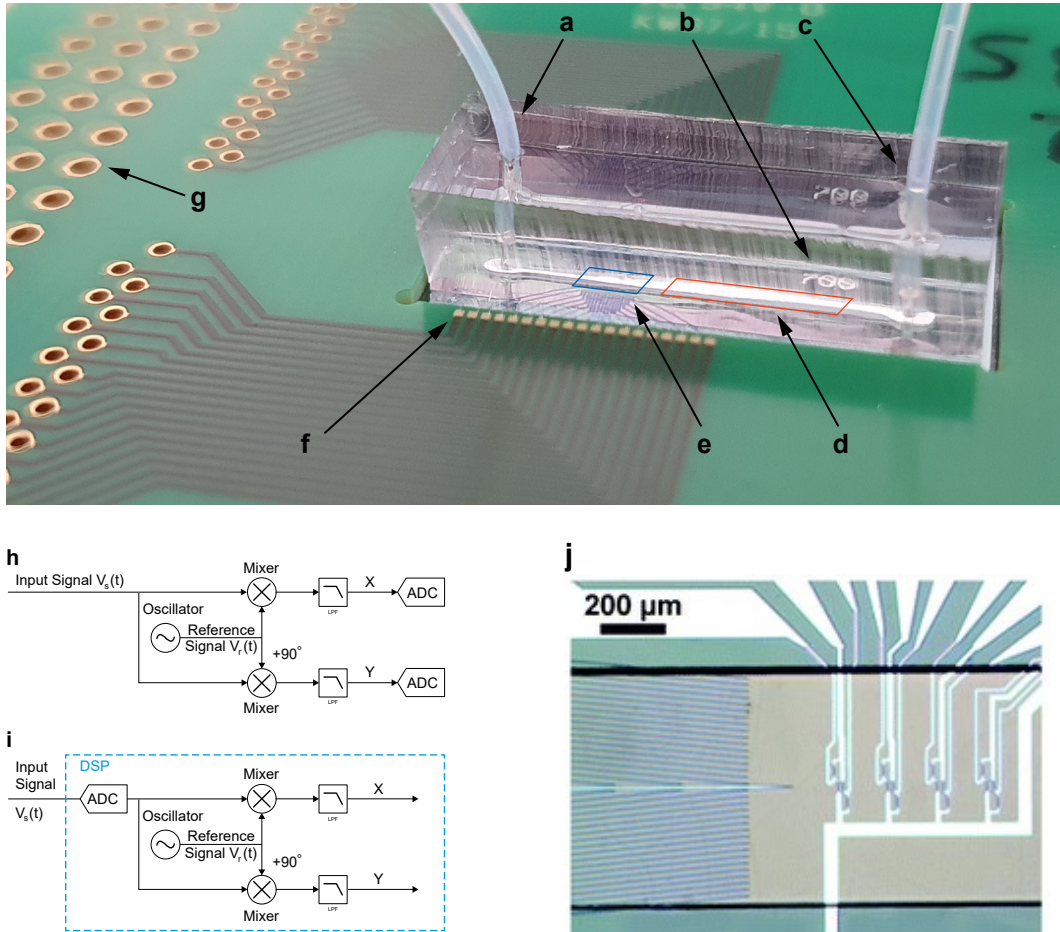


**Figure 10: Overview over the MRCyte Sensor Setup**

(a) Microfluidic outlet connection to waste reservoir. (b) Imprinted channel width. (c) Microfluidic inlet connection to syringe pump. (d) Magnetophoretic focusing region, not visible in this picture. (e) GMR-sensor region, the supply and bridge balancing traces are visible. (f) Gold bondpad: In order to connect the silicon sensor chip with the breakout printed circuit board (PCB), wedge bonds from the chip pads to the PCB pads are forged. (g) Through hole plating for the connection to the lock-in via jumper cables or a soldered connector plug. (h) Typical signal processing flow of a lock-in. The reference signal  $V_r(t)$  is splitted and mixed with the input signal with a phase difference of  $0^\circ$  and  $90^\circ$ . Then, both signals are low-pass filtered and sampled by an analog-to-digital converter (ADC). (i) Accordingly, in a digital signal processing (DSP) device the input signal is digitally converted beforehand, which in turn requires a highly sensitive and fast ADC. In contrast, DSP is more accurate and allows for software-controllable technical opportunities. (j) GMR-sensor bridge circuit inside the microfluidic channel. On the left hand side, magnetophoretic focusing structures are visible. On the right hand side, four Wheatstone bridges on a compliant ground plane can be observed.

a  $90^\circ$  phase-shifted copy of it. After demodulation, the result is constituted from signal components at the sum and the difference of signal and the reference frequency,  $\omega_s$  and  $\omega_r$ , respectively.(Eqs. 3.35 to 3.37) In the resulting signal, the trigonometric functions are Euler transformed and the magnitude  $R = \sqrt{X(t)^2 + Y(t)^2}$  acts as measurand. The high frequency compounds are then filtered digitally by a low-pass filter of varying order  $n$  to increase signal-to-noise ratio (SNR). As described in Eq. 3.39, a low-pass in the frequency domain can be described by a power series of first-order filters.

$$V_s(t) = \sqrt{2}R \cdot \cos(\omega_s t + \Theta) \quad 3.35$$

$$V_r(t) = \sqrt{2}e^{-i\omega_r t} = \sqrt{2} \cos(\omega_r t) - i\sqrt{2} \sin(\omega_r t) \quad 3.36$$

$$Z(t) = X(t) + iY(t) = V_s(t) \cdot V_r(t) \quad 3.37$$

$$= R \left[ e^{i((\omega_z - \omega_r)t + \theta)} + e^{-i[(\omega_z + \omega_r)t + \theta]} \right] \quad 3.38$$

$$H_n(\omega) = H_1(\omega)^n = \left( \frac{1}{1 + i\omega\tau} \right)^n \quad 3.39$$

However, with this measurement principle SNR can not increase infinitely. If the signal strength cannot be increased, the noise has to be reduced or avoided as much as possible. Nevertheless, noise is always caused by different sources in analog signals, for example thermal, shot, and flicker noise. Other sources are of technical origin, as for example ground loops, crosstalk, 50 Hz noise or electromagnetic pick-up. [82]

Now, to characterize a GMR with the lock-in, the easy layer has to be deflected to the full extents. For this, Helmholtz coils impose a high field in the orthogonal direction. The lock-in captures a hysteresis during the sweep from parallel to anti-parallel alignment of the layers at a specific bridge circuit. The steepness hereby indicates the sensitivity of the sensor element in the units  $V T^{-1}$ .

### 3. Materials and Methods

#### 3.1. Magnetic Sensor Device

##### 3.1.1. Assembly of Sensor

The fabrication of a microfluidic device on various substrates and layouts consists of two parallelizable workflows. First, the GMR-sensor chip (Sensitec) is assembled into a custom designed PCB (Piu-Printex) by double sided adhesive tape and a square glass slide (25 mmx25 mm, Thermo Scientific) at the bottom. A connection in between was formed by wedge wire bonding (HB10, TPT) which bonded 25 µm thick gold wire to the respective gold bond pads. The optimal parameters are listed in table 1. However, cru-

Foto of setup with arrows  
necessary parts Microscop  
Stages PEEK holder Helm  
coils Kepco MFL1 DAQ Los  
because of reduced velocit  
and magnetic drag Differen  
produced GMR stacks Wh  
stone Bridge setup Magne  
alignment

Parameters	Bond 1	Bond 2
Ultrasonic Power	250	300
Time / ms	200	200
Force / mN	250	300

Table 1: Wirebonding Parameters

cial for successful wire bonding is the optimal hole shape in the welding tool. Therefore, it was cleaned when bonds failed for no obvious reason by removing the gold wire and dipping the tip of the wedge into isopropanol (IPA). Then, *Test USG* was alternated for several seconds in multiple iterations. Afterwards, the wedge was blown dry from all sides with pressurized air and the wire was loaded back into the tool. After wire bonding, the manufactured sensors were placed in a wafer shipper box and stored in a dust free environment upon further use.

##### 3.1.2. Design and Fabrication of Microfluidics

In the second workflow, a microfluidic channel was manufactured via photo- and soft-lithography and bonded to the produced sensors from 3.1.1.

##### Development of Layout

layout design, hier noch die  
änder und verengungen  
den kapften 150u wafer?

## Patterning of Photoresist

3" (100) silicon wafers (Si-Mat) were dehumidified in a drying oven (UN30, Memmert) for 2 h at 150 °C to 180 °C. Then, immediately after they reached room temperature, they were placed centered inside a wafer spinner (WS-650-23B, Laurell Technologies). For the desired layer thicknesses 2 mL to 3 mL SU8-30XX (Microchem) were poured carefully onto the center of the wafer and the following program was carried out:

1. 500 rpm for 10 s at 100 rpm s<sup>-1</sup>
2. 3000 rpm for 30 s at 300 rpm s<sup>-1</sup>
3. Ramp down at 300 rpm s<sup>-1</sup>

Upon finish, the wafer was gripped outermost with wafer tweezers and soft-baked on a hot plate (super nova+, Thermo Scientific) for 5 min at 65 °C and at least 10 min at 90 °C. The optimal duration was determined if the gently touched resist did not stick to the tweezers. To prevent cracks in the resist caused by a fast temperature change, the wafer was cooled on the hotplate to room temperature. Such processed wafers were stored for a maximum of 4 weeks in a light-tight storage box.

To pattern the resist, the i-Line of a laser lithograph (Dilase 250, Kloe) was used. In preparation of the writing layout a AutoCADz \*.dxf-file with only one layer of polylines was imported to the program "Kloe Design", converted to contours and subsequently to polygons. For the filling a spot-size equivalent to the minimal structure resolution (as measured in Hicsanmaz [83]) and an overlap of at least 50 % was chosen. Departure and End Stabilization were chosen to 0.5 mm in a horizontal infill pattern. Also, flags for *auto-reverse mode*, *apply multiple trigger*, and *detect partial/full overlap* have been set. The writing trajectories were displayed for a last control before the export to ensure only closed contours. Finally the contour and filling were exported into separate files.

Both files were loaded in this order into the program "Dilase 250". Also the preprocessed wafer was placed inside the laser writer and attached to the vacuumed stage. With the integrated camera the global zero was set to the wafer center by finding the horizontal or vertical edges and adding/subtracting the radius of the wafer ( $1.5" \approx \varnothing 38.1\text{ mm}$ ). The focus point was set to the top of the resist and subsequently moved 0.07 mm relative down for thick layers. Then the program was initiated with 100 % laser modulation and 20 mm s<sup>-1</sup> to 40 mm s<sup>-1</sup> writing velocity.

## **Soft Lithography**

The fabricated wafer was placed the center of a 90 cm petri dish. A PDMS mold was created by vigorous mixing of the pre-polymer base with its curing agent (Sylgard 184, Dowsil) in a ratio of 10:1 (w/w). For 3" wafers, thin channels were casted from 15 g, normal channels from 20 g PDMS in the petri dish. Gas bubbles were removed from the mixture in a desiccator for 20 min at 2 hPa , and the clear PDMS was cured in an oven (Um, Memmert) for 1 h at 60 °C. After curing, the PDMS mold was released from the petri dish carefully, taken off the wafer and stored in a clean petri dish upon further processing.

## **Bonding of Microfluidics**

Under laminar flow, crosslinked molds were cut into pieces with the respecting single microfluidic ( $\mu$ F) with a razor blade. Holes for in- and outlet were punched through the containing channels with a biopsy puncher (ID 0.5 mm, WellTech). The substrates and  $\mu$ Fs were sonicated in acetone and deionized water (diH<sub>2</sub>O) for 5 min and dried with filtered nitrogen gas (N<sub>2</sub>) completely. For the bonding of PDMS to various substrates different protocols have been established:

## **PDMS Glueing**

Here, a micron-height layer of uncured PDMS was used as an adhesive layer between  $\mu$ F and substrate. Approx. 3 mL were poured onto a 3" wafer and spun down for 5 min at 6000 min<sup>-1</sup>. The microchannel was placed on the substrate by visual control of a stereo microscope (SMZ800, Nikon) with 8-fold magnification. Subsequently, the bonding process could be finished by a 1 h bake at 60 °C or over-night at room temperature.

## **Plasma Bonding**

The respective parts were activated by the exposure to a controlled O<sub>2</sub>-plasma. Bringing the activated surfaces in contact immediately triggers the formation of covalent bonds. First, the acetone-wiped substrates and the microchannels were centered inside the plasma cleaner (Zepto, Diener). Second, vacuum was applied to a final pressure <0.2 hPa. Third, the chamber was flushed with pure O<sub>2</sub> until a chamber pressure from 0.6 hPa to 0.8 hPa had been stabilized. Fourth, the plasma process was executed with 30 W (Power-Potentiometer: 100) for 45 s to 60 s (Time-Potentiometer: 15-20). Upon finish, the chamber was flushed for 5 s and ventilated. Immediately after, the corresponding workpieces were brought into contact and pressed together gently. To ensure

a durable bond, the assembled structures were baked for 1 h at 60 °C.

### Reversible Bonding

To bond the  $\mu$ F to a substrate reversibly and without residues, the channel can be brought into contact with the bottom part without any adhesinon agent. For low-pressure as well as vacuum driven flows, this method is preferable due to its time and work efficiency.

#### 3.1.3. Peripheral Components and Optical Readout

Each sensor chip was characterized by the hysteresis steepness (equivalent to the sensitivity) and the zero-crossing at half-maximum in a customized setup. Therefore, the underlying 32 x 27 x 5 mm NeFeB magnet (NE3227, IBS Magnet) was adjusted on micromanipulator tables (PT, Thorlabs) in three axes to optimize both parameters. Afterwards, PTFE-tubing (ID 0.5 mm, Reichelt Chemietechnik) was connected on the in- and outlet of the microfluidic. A dispensing tip (OD 0.42 mm, Nordson) was connected to the inlet tubing. Initially a 1 mL syringe (ID 4.72 mm, Terumo) was connected with  $\text{dH}_2\text{O}$  or PBS and flushed with  $100 \mu\text{L min}^{-1}$  to  $200 \mu\text{L min}^{-1}$  by a syringe pump (Fusion 4000, Chemyx).

### Hysteresis Alignment

For any used GMR-sensor, a characterization of its sensitivity ( $\text{V T}^{-1}$ ) was performed. Therefore, its hysteresis was imposed by two Helmholtz coils ( $L_s = 167 \text{ mH}$ ,  $d = 150 \text{ mm}$ , Brockhaus) generating  $7.8 \text{ mT A}^{-1}$  orthogonal to the easy axis of the GMR which were driven by a voltage-controlled current source (BOP 50-8M, Kepco Inc.) with  $\pm 2 \text{ A}$  at a peak-to-peak voltage ( $V_{pp}$ ) of 20 V. The control voltage was supplied by LabView (2018, 32-bit, National Instruments) supplied by a digital I/O card (USB-6351, National Instruments) in the range of -10 V to 10 V. The resulting sensor signal was fed into the current input of a lock-in amplifier ( multi frequency lock-in (MFLI), 5 MHz, Zurich Instruments). Redigitization and processing was carried out by the same digital I/O card and labview program as for the input control.

### Single GMR

The change in resistivity over one whole Wheatstone bridge was measured with a fully-integrated lock-in amplifier ( MFLI, 5 MHz, Zurich Instruments) by a reference peak voltage ( $V_p$ ) of 100 mV to 800 mV. The reference frequency was chosen randomly in a

range of  $100 \pm 25$  kHz such that any harmonics were avoided. The measured differential bridge balance was then demodulated and filtered with a time constant of  $299.7\ \mu\text{s}$  by a third order low-pass filter and amplified by the factor 10 000. Subsequently, the processed signal was sampled at  $53.2\ \text{kS}\ \text{s}^{-1}$ , fed into a digital I/O device (USB-6351, National Instruments) with input range  $-10\ \text{V}$  to  $10\ \text{V}$  and processed in LabView. Additionally, a 40x microscope image (DM2500, Leica Microsystems) was captured by a CCD-camera (Grasshopper3, FLIR) and displayed in real-time to control the experiment.

### Dual GMR

For the measurement of two GMR-sensors simultaneously, the setup from 3.1.3 was duplicated in two different manners. However, the exact same settings in the device control software were crucial for successful measurements. In a first approach, the supply cable of one MFLI was splitted and fed into both sensors, while the bridge balance was evaluated by the same and an additional lock-in, both with the exact same settings. Consequently, the ground pin of the one sensor was the reference also for the other sensor and one ground pin was therefore left floating. This method posed the least cable length and therefore noise, but was also prone to cross-talking between the used BNC-cables respectively -connectors.

circuit/picture of both?

Second, two MFLI's were driven in a master-slave clock synchronization by the Multi-Device Sync function. Therefore, the *trigger out* and *clock out* ports on the backside of the master were connected to the slave's *trigger in* and *clock in* ports. Additionally, the *trigger out* was split by a T-connector piece in order to feed it also back into the master's *trigger in* port.

In both cases, the output of both lock-ins was directed to their respective *AUX 1* ports and connected to another LabView program by the previously mentioned DAQ-card.

### Differential Sensor Setup

In some experiments, two PCBs were stacked with nylon spacers () with various spacings 3 mm, 5 mm and 8 mm between their edges above the permanent magnet. Additionally the outlet tubing of the upper chip was connected to the inlet of the lower chip with the least dead volume possible. The hysteresis was then adjusted for both sensors on various bridges consecutively. Measurements were performed as described in 3.1.3

spacers

with two completely independent lock-in amplifiers.

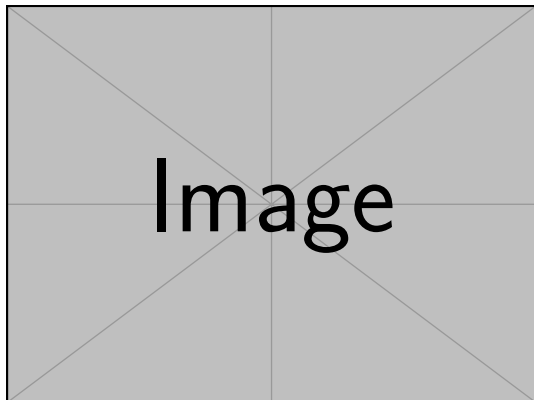


**Figure 11:** Here comes a nice drawing from the stacked pcb setup

### GMR Data Analysis

Subsequent data analysis of the acquired streams from both two and one sensor measurements were modified by a custom labview VI to cut the first sample of the stream which was mandatory for the next step. Next, the characteristic signal patterns were detected in the continuous stream by the *GMR\_Tool\_227* by a rolling-mean thresholding method. The resulting \*\_ana.csv files were then processed by a custom Matlab script, which in turn computed averages and simple parameters of a single detected signal or whole measured, p.e. the total volume or the signal count therein. The Matlab script saved any analyzed data also in the \*.csv format which was finally plotted in Origin (2020b, OriginLab)

## 3.2. Magnetic Beadometry

Magnetic beads were measured in various manners. First, beads were let rolling over functionalized substrates under microscope control (DM6, Leica) and image acquisition for count and trajectory analyses (LAS X, Leica). Second, beads were measured in buffer in whole blood samples magnetically to determine their concentration in the different samples. The previous concentration measurements were then adapted to functionalized surfaces in order to detect a difference in concentration. In all experiments, PTFE-tubing (ID 0.5 mm, Reichelt Chemietechnik), dispensing tips (OD 0.42 mm, Nordson), 1 mL syringes (ID 4.78 mm, Terumo), a syringe pump (Fusion 4000, Chemyx) and a microfluidic channel with dimension 700 µm x 150 µm (width x height) were used.

the block diagram for work-

?

concentration Measurement

e Blood Bead Spiking

### **3.2.1. Bead Capture Assay**

As prerequisite for the bead capture assay, the concentration of different self-biotinylated particles was determined meticulously in a Neubauer Improved counting chamber as well as by flow cytometry and adjusted between  $1 \mu\text{L}^{-1}$  to  $10 \mu\text{L}^{-1}$  in PBS with Tween 20 (PBS). Further, a GMR sensor was fabricated, loaded unspecifically with  $1 \text{ mg mL}^{-1}$  neutravidin, hysteresis aligned and connected in the single GMR setup (see 3.1.3). As first step, the bead adhesion was determined by finding the minimal flow rate at which non-biotinylated beads were still rolling freely and at second, by finding the maximal flow rate at which biotinylated beads were still notably captured, both by microscope observation and sensor signal analysis. The average flow rate of these two was consequently held constant over all experiments. Subsequently, beads with different surface coverages of biotin were pumped alternatingly through the channel and over the sensor. The generated data was analyzed after the standard protocol in 3.1.3.

## **3.3. Surface Bio-Functionalization**

### **3.3.1. Surface Activation**

To functionalize any silicon containing surface with Si—OH groups which the utilized silane could interact with, multiple surface activation pathways were explored. First, substrates were cleaned in hydrochloric acid (HCl):methanol (MeOH) and  $\text{H}_2\text{SO}_4$  before they were immersed in boiling water. Second, surface silanol groups were achieved by piranha immersion. Third a HF dip and fourth a oxygen plasma treatment was tested. For all methods, the following reagents were used: di $\text{H}_2\text{O}$  ( $0.054 \mu\text{S}$ , Merck MilliQ)), acetone ( $>99.9\%$ , VWR), ethanol (EtOH) (absolute, VWR), MeOH (99.8 %, VWR), acetic acid (AcOH) (glacial, VWR), HCl (37 %, Sigma-Aldrich),  $\text{H}_2\text{SO}_4$  (95 % to 98 %, VWR),  $\text{H}_2\text{O}_2$  (30 % (w/w), Sigma-Aldrich), HF (10 %, VWR)

### **Work Safety Remarks**

Before the work with one of the acid solutions was carried out, several safety measures were implemented. As any reacting acid solution becomes very hot immediately due to the exothermic reaction, every container should be placed inside a cooled water or ice bath. Additionally, the beaker as well as concentrated acid flasks should be gripped firmly by a laboratory stand to avoid a tip over. As the reactivity of chemicals is highly temperature-dependent, the solutions was processed further when they had been cooled to  $\leq 80^\circ\text{C}$ . It should be also noted that - as in every chemical reaction, but

especially ones with  $H_2SO_4$  and HF - the acid was always poured into the other reactant to avoid splashing and boiling.

### Plasma Activation

For the plasma activation, process parameters similar to the PDMS bonding technique in ?? were chosen. After initial cleaning via sonication in AcOH and diH<sub>2</sub>O for 5 min each, the substrates were dried in N<sub>2</sub>-gas and placed inside the plasma chamber. The chamber was evacuated to a final pressure <0.2 hPa and then flushed with pure O<sub>2</sub> until a chamber pressure between 0.6 hPa to 0.8 hPa had been stabilized. Fourth, the plasma process was executed with 100 W (Power-Potentiometer: 300) for 300 s (Time-Potentiometer: ). Upon finish, the chamber was flushed for 5 s and ventilated.

poti for hydrophobic sur-

### Hydrochloric-Sulfuric Acid Activation

In order to degrease any glass or Si<sub>3</sub>N<sub>4</sub> surface, a protocol according to Dressick et al. [84] was used. There, the surfaces were first sonicated in acetone and diH<sub>2</sub>O for 5 min. Afterwards these were immersed in a 1:1 (v/v) solution of HCl:MeOH for >30 min, rinsed with diH<sub>2</sub>O copiously and soaked in H<sub>2</sub>SO<sub>4</sub> for >30 min as well. Then, the samples were rinsed again in deionized water. To form silanol groups on the activated surface, the surfaces were finally immersed in >90 °C heated (SuperNova+, Thermo Scientific) diH<sub>2</sub>O for at least 2 h.

### Piranha Activation

In this method, activation was carried out in a 1:7 (v/v) piranha solution at 70 °C for 15 min to 30 min. After treatment, the samples were rinsed carefully with diH<sub>2</sub>O three times.

### Hydrofluoric Acid Activation

For HF activation of Si<sub>3</sub>N<sub>4</sub>, a protocol after Liu et al. [53] was reproduced. Acetone cleaned samples were immersed in 1 % aqueous HF for 2 min and rinsed with diH<sub>2</sub>O extensively afterwards without letting the surface dry at any time.

### 3.3.2. Chemical Surface Functionalization

Chemically activated surfaces were now coupled with APTES covalently. Therefore an aqueous silane solution was prepared from EtOH with volume fractions of 5 % diH<sub>2</sub>O, 0.5 % aqueous AcOH (pH 4.5) and 1 % APTES in this order. The samples were soaked

immediately after their activation in the silane solution. The reaction was carried out for 2 h to 4 h at >40 °C or for 1 h at 70 °C. At finish, all specimens were rinsed with EtOH or sonicated for 5 min in absolute EtOH.

Then, the amine terminated surface modification was enhanced by a carbodiimide conjugation with poly(acrylic) acid (PAA) after Andree et al. [59]. As above, a reaction consisting of 1 mM MES buffer (pH 6) with 1 mg mL<sup>-1</sup> PAA, 6 mM EDC and 3 mM NHS was activated for 15 min on a magnetic stirrer. Subsequently, the prepared samples were immersed in the solution for 1 h on a rotation shaker (VWR). As final cleaning, the slides were rinsed or sonicated for 5 min in diH<sub>2</sub>O and stored in fresh diH<sub>2</sub>O at 4 °C up to 14 d upon further use.

### Tensiometry

All above methods were characterized by a custom built tensiometer and the ImageJ Fiji plugin DropSnake. [85, 86] In an experiment, a substrate was dried by N<sub>2</sub> and placed in the camera focus. Subsequently, a sessile drop of 1 µL was placed in the focus with a micropipette (Eppendorf) without touching the surface. The focus of the camera was adjusted meticulously to gain maximum contrast at the droplet contour and a homogeneously black droplet. Images were then acquired by an USB-microscope pointing in an acute angle onto a drop on the surveyed substrate, while background illumination was provided by a lamp. The images were then cropped, rotated such that the droplet edges were perfectly horizontal and converted to 8-bit grayscale. After preprocessing, the top half contour was outlined by at least 8 points inside the DropSnake plugin and the resulting contact angles were exported.

usb microscope?

Background Illumination

### 3.3.3. Surface Bioconjugation

A functionalized surface from 3.3.2, was now bonded to a 150 µm microfluidic channel as in 3.1.2 and incubated for at least 5 h, but mostly over night at 7 °C. Upon finish, microfluidic PTFE-tubing (ID 0.5 mm, Reichelt Chemietechnik) was connected to the inlet and outlet with precision tweezers. Then, the channel was equilibrated with 100 µL to 300 µL MES buffer in a syringe (1 mL, Terumo) with a syringe pump (Fusion 100, Chemyx) with 100 µL min<sup>-1</sup>. Then, 50 mM, 100 mM and 300 mM of EDC and NHS were flushed into the channel with the same flow rate after an dissociation time of 10 min. The channel bottom was incubated for 30 min and then washed again with 100 µL MES buffer.

Subsequently, a desired protein was loaded in high concentration (Neutravidin ( 31050, Thermo Scientific):  $1 \text{ mg mL}^{-1}$ , Antibody:  $20 \mu\text{g mL}^{-1}$ ,) via the tip of a 1 mL syringe or flushed into the channel by vacuum from a microcentrifuge tube. The functionalized channels were now incubated over night in an ice box. Before use, the  $\mu\text{F}$  was washed with  $100 \mu\text{L}$  PBS with 0.02 % nonionic surfactant (Tween 20, Sigma Aldrich) (PBST) for 2 min. Any unreacted binding sites were blocked by a solution of 500 mM ethanolamine hydrochloride (E6133, Sigma-Aldrich) in  $\text{dH}_2\text{O}$  for 30 min. After another washing step, the functionalized channels were further used for either microscope or magnetic bead-capture experiments.

However, in some experiments focus lay on physisorption rather than on chemisorption. Therefore, after the bonding of a microfluidic channel to a non-functionalized substrate, the channel was equilibrated as mentioned before with MES buffer (cave: without surfactant). Then it was incubated with a solution containing protein in highest concentration, p.e.  $1 \text{ mg mL}^{-1}$  neutravidin, at  $7^\circ\text{C}$  over night, while infusing and withdrawing a small volume fraction (approx.  $50 \mu\text{L}$ ) continuously by a syringe pump. Upon finish, the tubing was exchanged with a drop of water a the connection and channel was flushed with PBS carefully at  $50 \mu\text{L min}^{-1}$  to avoid any gas bubbles inside the fluidic. It was stored up to 10 d without any notable decrease in functionality.

### 3.3.4. Particle Functionalization

Micro- and nanobeads from different suppliers were used in functionalization experiments but modified after the same procedure according to their surface charge. A positive partial charge from an amine-terminated bead and a negative partial charge from a carboxyl-terminated bead was used to promote different electrostatic interactions with a microchannel's surface. A list of all used particles and their respective parameters are depicted in table 2.

#### Amine-terminated Beads

For amine beads, NHS-Biotin (203118, Sigma Aldrich) was used for a covalent attachment after the previously mentioned carbodiimide chemistry. Initially, the biotin was dissolved to a concentration of ( $50 \text{ mg mL}^{-1}$ ) in water-free dimethyl sulfoxide (DMSO) and stored upon further use at  $-25^\circ\text{C}$ . The attachment to microbeads was titrated by the molar weight ratio of both reagents and ranged from 10-fold molar excess to a

Supplier	Brand Name	d ( $\mu\text{m}$ )	Functionalization	Surface Charge ( $\mu\text{mol g}^{-1}$ )	Magnetic Particle Momentum ( $\text{A m}^2$ )
micromod	micromer	8	amine	2.0	0
micromod	micromer-M	8	amine	1.0	$>1.12 \times 10^{-12}$
micromod	micromer	8	carboxyl	2.0	0
micromod	micromer-M	8	carboxyl	1.0	$>1.12 \times 10^{-12}$
invitrogen	Dynabead M280	2.8	streptavidin	0.65-0.90	N.A.
invitrogen	Dynabeads MyOne C1	1.05	streptavidin	>2.5	N.A.
Ocean Nanotec	SV0050	0.05	streptavidin	N.A.	N.A.
micromod	BNF-Dextran-redF	0.1	streptavidin	0.2	$>1.27 \times 10^{-16}$
micromod	nanomag-D-spio	0.1	streptavidin	0.02-0.04	$>5.5 \times 10^{-17}$

**Table 2:** Properties of the used microbeads and magnetic nanoparticles (MNPs).

10 000-fold deficit of biotin over the amine.

In most cases, 20  $\mu\text{L}$  of micromer beads were aliquoted in several microcentrifuge tubes (1.5 mL, Eppendorf) to generate a standard curve of functionalization density later on. NHS-Biotin was diluted to a concentration of 0.5 mg  $\text{mL}^{-1}$  with PBST and vortexed. Then, beads and biotinylation reagent were mixed in the desired ratio thoroughly and incubated for 1.75 h at 8 °C in a shaker (Thermomixer, Eppendorf) at 1400  $\text{min}^{-1}$ .

### Carboxyl-terminated Beads

The surface of carboxyl-terminated beads was esterified by EDC-NHS chemistry and covalently bound to amine-PEG<sub>2</sub>-biotin (EZ Link, Thermo Scientific). First, the bead buffer was exchanged to MES buffer with Tween 20 (MES) with one washing step by centrifugation (as in 3.3.4) to a final bead concentration of 5 mg  $\text{mL}^{-1}$ . 100 mM EDC in diH<sub>2</sub>O and 50 mM NHS in DMSO were prepared and added to the bead solution to

a final concentration of 25 mM and 12.5 mM each. The suspension was reacted for 30 min on a shaker at 1400 min<sup>-1</sup> and washed once with MEST buffer. Then, amine-PEG<sub>2</sub>-biotin was added from 10-fold molar excess to a 10 000-fold deficit of biotin over the amine and volume adjusted. The samples were incubated on a shaker for 1.75 h at 8 °C in a shaker at 1400 min<sup>-1</sup>.

### Post-Processing and Characterization of Beads

After the incubation, the beads were washed either magnetically or via pelleting. Magnetic washing was carried out in a magnet stand (), where the beads were separated for 2 min and then washed 3 times with 500 µL to 1000 µL PBST. Pellet washing was conducted three times in a table centrifuge (Fresco 17, Thermo Scientific) at 800 x g to 1200 x g for 10 min. The supernatant was discarded and the pellet was dissolved in 500 µL to 1000 µL PBST. After both washing procedures, the beads were resuspended in 100 µL MACS running buffer (MACS) or PBST and stored at 4 °C.

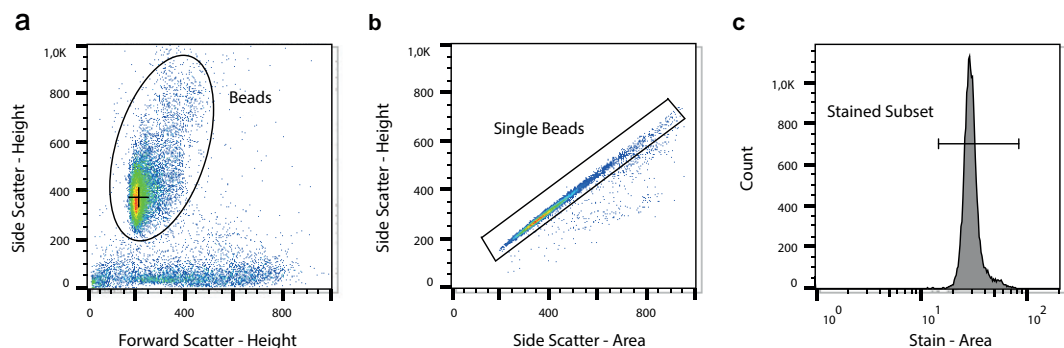


**Figure 12: Gating Strategy for Biotinylated Beads**

a, In the forward-side-scatter plot, the general bead population with high side scatter is selected from the background. b, Single beads are differentiated by their sphericity, their ratio of height:area in the side scatter. Points on the line through the origin are spherical. c, The stained subset in the respective color is now selected and the median fluorescence intensity (MFI) as well as the coefficient of variance (CV) is computed.

Characterization of any surface modification was done via fluorescence-flow cytometry or -microscopy. 30 000 beads to 60 000 beads were diluted to 20 µL and incubated with 100 ng streptavidin-atto488 (49937, Sigma Aldrich) or Anti-Biotin-PE ( Miltenyi) for 30 min at 8 °C in a shaker. The beads were then diluted to a final volume of 100 µL, transferred to a 96-well plate (TPP) and measured in the autosampler of a flow cytometer (MACS Quant Analyzer 10, Miltenyi). Following parameters were held constant over all measurements: *Flow Rate*: High, *Mix Sample*: Strong, *Mode*: Standard, *Uptake/Sample Volume*: 100 µL. The photomultiplier voltages of forward and side scatter

were lowered in most experiments by 10 V and 120 V respectively due to the homogeneous and reflective nature of the particles. Data analysis was performed by FlowJo (10.6.2, Becton Dickinson) after a gating strategy which is depicted in Fig. 12. For fluorescence microscopy, the beads were stained with streptavidin-atto488 after the same procedure and imaged statically on a covered microscope slide at an exposure time of  $>100\,000\,\mu\text{s}$  and a gain  $>15$ . Images were then processed by Fiji. In both measurements, the resulting data was plotted in Origin (2020b, OriginLab).

#### **Coating of Biofunctionalized Non-Magnetic Beads with Magnetic Nanoparticles**

The biotinylated, non-magnetic microbeads (Table 2) were coated covalently with different MNPs in order to establish a bead-side titration of binding sites. Therefore,  $5\,\text{mg mL}^{-1}$  biotinylated beads in PBST were equilibrated for 10 min and mixed with  $7.5\,\mu\text{g}$  BNF-dextran-redF-streptavidin / nanomag-D-spio,  $6\,\mu\text{g}$  of SV0050 or  $10\,\mu\text{g}$  Dynabeads C1 over night on a shaker. Afterwards, the supernatants were exchanged twice by careful centrifugation to avoid sedimentation of the nanoparticles.

## 4. Results

### 4.1. Virtual Prototyping of Cell Signals

During the course of this thesis, numerical simulations for the microchannel have been carried out. On the one side, a simulation about the shape of a GMR-sensor signal of cells was performed, where the magnetic momentum was conveyed through MNPs bound to their surface. On the other side, cell aggregates have been looked at in the same manner with different angles respective to the sensor. Both simulations were then correlated to a reference dipole, with the equivalent magnetic momentum distributed in the center of mass.

Additionally, the flow and shear field inside the channel was simulated numerically for the channel cross-section as well as for a particle near the walls. A force equilibrium simulation was also established in a basic manner.

Every simulation was captured in a MATLAB class “MRCyte”, which contains material parameters and constants for all simulations above.

#### 4.1.1. Numerical investigation of immunomagnetic label density and size on quantitative magnetoresistive sensing of single cells and cell aggregates

In order to mimic a immunomagnetically labeled cell flowing over the sensor half bridge, the planar integral of the respective magnetic flux density ( $\mathbf{B}$ ) was solved analytically. Here,  $\mathbf{r}_i$  specifies the distance vector of a single MNP from the sensor plane. The magnetic flux density was converted by the GMR to a resistive change  $\mathbf{R}_{sig}$  by scaling it with the GMR-sensitivity  $S$  and subsequently into a signal voltage  $\mathbf{V}_{sig}$  inside the bridge branch.(Eqs. 1.1 to 1.3)

In the numerical approach, MNPs were randomly sampled on a sphere surface with an equivalent diameter of  $4\text{ }\mu\text{m}$  or  $8\text{ }\mu\text{m}$ . Then, the signal was computed for every MNP during every timestep. Additionally, the MNP distribution was rotated in every iteration to resemble a rolling motion. The computed signals were then cross-correlated to the signal of a reference flux density  $\mathbf{B}_{ref}$  caused by a point-like magnetic moment located

in the geometric center of the same sphere.

$$\mathbf{B}(t) = \sum_{i=1}^N \frac{1}{A_{\text{Sensor}}} \int_{-\frac{l}{2}}^{\frac{l}{2}} \int_{-\frac{w}{2}}^{\frac{w}{2}} \frac{\mu_0}{4\pi} \left( \frac{3\mathbf{r}_i(t) (\mathbf{r}_i(t) * \mathbf{m}_i)}{|\mathbf{r}_i(t)|^5} - \frac{\mathbf{m}_i}{|\mathbf{r}_i(t)|^3} \right) dx dy \quad 1.1$$

$$\mathbf{R}_{sig}(t) = -\mathbf{B}(t) * \frac{S}{100} * R + R \quad 1.2$$

$$\mathbf{V}_{sig}(t) = \frac{\mathbf{R}_{sig}(t)}{R + \mathbf{R}_{sig}(t)} * V_p - \frac{V_p}{2} \quad 1.3$$

By its formula, cross-correlation  $R_{xy}(\tau)$  yields a displacement dependent signal through its convolution of the complex conjugated reference signal  $\mathbf{V}_{ref}^*(t)$  with the sample signal  $\mathbf{V}_{sig}(t + \tau)$ . (Eq. 1.4) Therefor, only the maximal correlation of this function was considered in further analyses.

$$\max\{R_{xy}(\tau)\} = \max \left\{ \int_{-\infty}^{\infty} \mathbf{V}_{ref}^*(t) \mathbf{V}_{sig}(t + \tau) dt \right\} \quad 1.4$$

Signal Similarity For Cells With Varying Bead Coverages, Cross-Correlation between single dipole with sum magentic moment and surface covered with randomly distributed magnetic particles, simulation of cell rolling velocity and forces

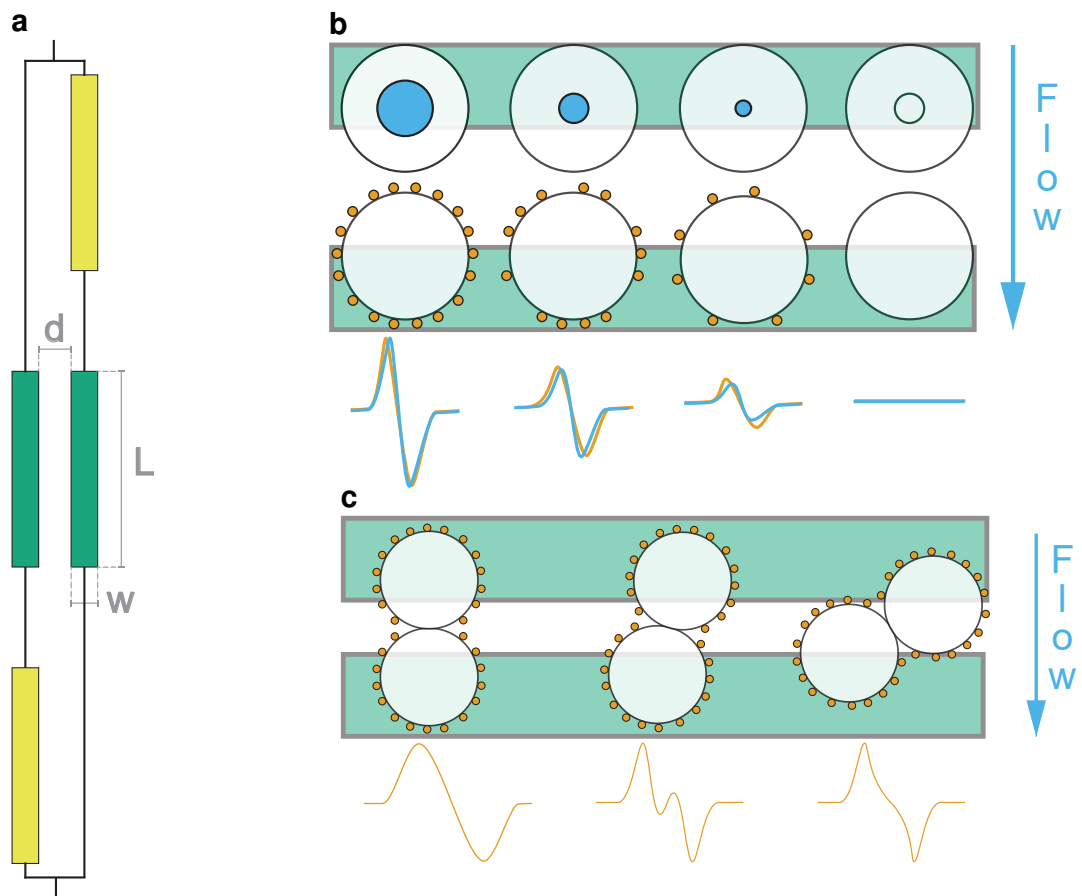


**Figure 13: Particle Coverage Simulation**

(a) Dimensions of the GMR Wheatstone bridge sensor: Distance  $d$  between both variable bridges (green), width  $w$  of a GMR-sensor, length  $L$  of a sensor. (b) Scheme of single cell simulation: The ideal magnetic dipole in the geometric center of a sphere (●) causes a signal deviation from the real cell signal with magnetic moment distributed on the cell surface. (●) (c) Signal shapes of different angles of two-particle aggregates lead to differing signal shapes.

Parameter	Unit	Value	Explanation
w	m	$2.0 \times 10^{-6}$	GMR width
l	m	$30.0 \times 10^{-6}$	GMR length
d	m	$14.0 \times 10^{-6}$	Distance between two sensors
R	$\Omega$	250	GMR Resistance
$V_p$	mV	100	Supply voltage
$t_{free\ layer}$	m	$7.0 \times 10^{-9}$	Thickness of free layer
M	$A\ m^{-1}$	$2.0 \times 10^4$	Volume Magnetization
$V_{noise,rms}$	V	$2.5 \times 10^{-6}$	Artifical noise
Sim. Space	m	$[-25 \times 10^{-6}, 25 \times 10^{-6}]$	Interval around sensor center

**Table 3: Magnetic Simulation Parameters**

Constants used inside the framework for the simulation of the magnetic field inside the GMR Wheatstone half bridge. The volume magnetization was adapted according to the simulated particle size.

#### 4.1.2. Single Cell Signal

Aim of these simulations is to find a measure of how magnetic labeling of a cell affects signal shape and its subsequent analysis. A single cell with a surface coverage of 5 % to 99 % of a densely packed sphere was loaded randomly with MNPs at different sizes. Then, the previously explained rolling motion over the sensor bridge was simulated with the parameters specified in Table 3. After correlation of the resulting signal voltage to the reference dipole signal (Fig. 13b, ●) with three randomly MNP distributions, the dependency on the coverage was evaluated. As shown in the schematic Fig. 13b, an increase in signal peak amplitude but also in full width at half maximum (FWHM) at growing coverage was expected .

The expected behavior matches the data analysis (Fig. 14). Each two analyzed sphere diameters 4  $\mu\text{m}$  and 8  $\mu\text{m}$  with MNP sizes ranging from 20 nm to 2  $\mu\text{m}$ , show a great standard error of the mean (SEM) at low coverage. This very probably is subjected to the momenta of single particles which play a greater individual role and hence influence the signal shape significantly because the overall dipole momentum in the sensor loses homogeneity.

Another observable effect is related to the MNP size. Absolute correlation differs from

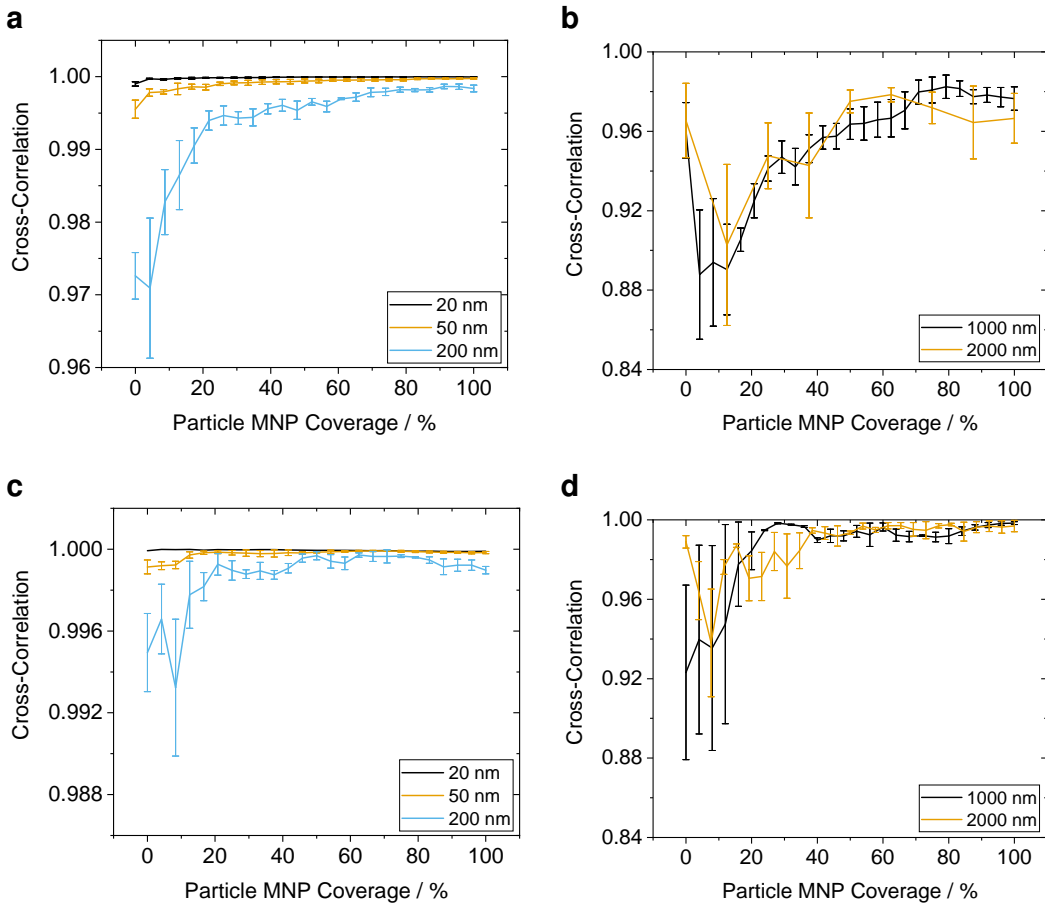


**Figure 14: Coverage Dependent Signal Correlation**

MNP coverage of a sphere with 4  $\mu\text{m}$  (**a**, **b**) and 8  $\mu\text{m}$  diameter (**c**, **d**) covered by magnetic particles ranging from 20 nm to 2000 nm. A cross-correlation increase which is inversely proportional to the MNP size can be observed.

20 nm to the ten and hundred fold diameter significantly. This can be related to the magnetic momentum per MNP as it is dependent on the volume - thus  $r^3$ . However, for bigger magnetic particles this does not hold true because the composition changes from pure magnetite to a polymer shell with embedded oxide core at around 150 nm. Nevertheless, larger particles carry also greater magnetic momentum which brings also the aforementioned influence of single MNPs into consideration for that effect.

Also, the densely packed sphere surface can evidently carry more smaller than larger MNPs. This ranges from 641 600 MNP at 20 nm to 81 at 2  $\mu\text{m}$  for a sphere radius of 4  $\mu\text{m}$  and limits the maximum achievable momentum.

In reality, a maximum immunomagnetic label density depends not on the densely packed sphere but rather on the present antigens, and association or dissociation constants. Therefore, a complete saturation coverage is not achievable under physiological conditions. This leads to the fact that any possible momentum by deposition of 20 nm and 50 nm on a cell surface cannot be resolved from noise by this sensing setup.

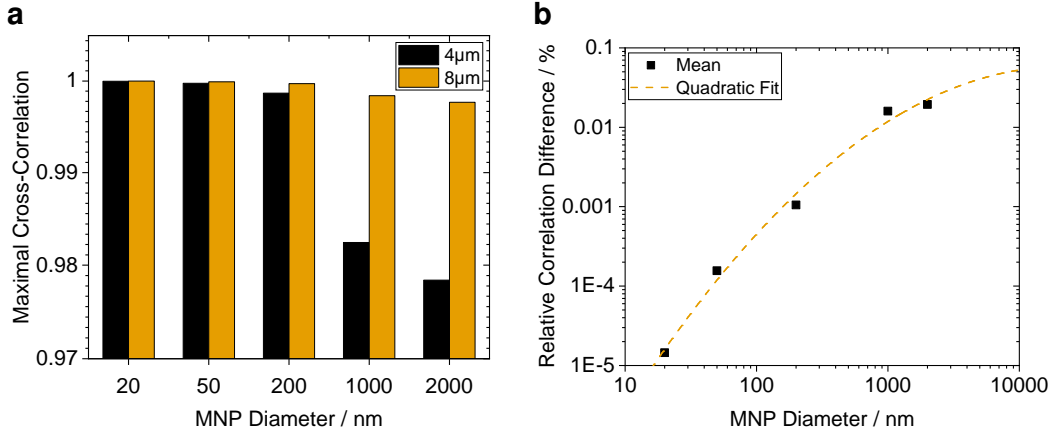


**Figure 15: Maximal Cross-Correlation Differences**

(a) Mean coverage at 99% for 4  $\mu\text{m}$  and 8  $\mu\text{m}$  spheres. A negative dependency on the MNP size can be explained by the ratio of magnetic momentum per unit surface and its homogeneous distribution across the whole surface.  
 (b) Relative correlation error between 4  $\mu\text{m}$  and 8  $\mu\text{m}$  spheres with a quadratic fit. The quadratic behavior could be related to the relative surface area which can be occupied by magnetic momentum. (Adj.  $R^2 = 0.992\,09$ )

Also, it can be seen that the correlation approaches a maximum obtainable value for every MNP size. Referenced for both simulated sphere diameters in (Fig. 15a), a inverse proportionality between correlation and MNP diameter is visible. The trend in respective maxima can be related to differences the magnetic momentum amplitude and coverage inhomogeneity.

Inter-sphere compared, maximum correlation shows also a significant decrease in for higher MNP sizes as the particle diameter itself increases. The relative error between both sizes - as computed in Eq. 1.5 - is depicted in Fig. 15b. Assuming a dependency on the available particle surface and subsequently the fraction which can be occupied by MNPs, a quadratic fit seems appropriate.(Eq. 1.6) The fit could indicate that a reference dipole cannot be discriminated from a cell at small MNP diameters while the correlation error becomes nearly constant at great MNPs.

$$\text{Relative Correlation Difference} = 1 - \frac{\max\{\text{Cross-Correlation}(d = 4 \mu\text{m})\}}{\max\{\text{Cross-Correlation}(d = 8 \mu\text{m})\}} \quad 1.5$$

$$\text{Relative Correlation Difference} = -0.385\,32 d_{MNP}^2 + 3.345\,74 d_{MNP} - 8.496\,29 \quad 1.6$$

#### 4.1.3. Cell Aggregates

In another simulation, two 200 nm-MNP-covered spheres were attached to each other in differing angles and simulated flowing over the sensor. Signal similarity to a magnetic

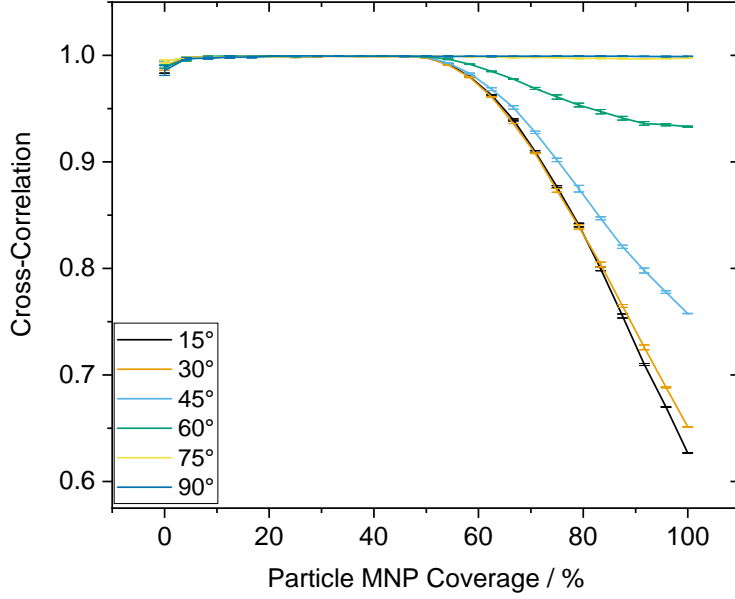


**Figure 16: Signal Correlation between Two-Cell Aggregates At Shifting Angles**

Two-Sphere aggregates are covered with 200 nm MNPs and simulated flowing over the sensor at differing respective angles. The SEM indicates a difference in cross-correlation of three truly random MNP distributions. For low yaw angles and high coverages, the aggregate's signal reflects rather two single dipoles in superposition than one quite homogeneous dipole. This causes a high signal deviation from the reference and thus a low degree of correlation.

dipole in the center of a single reference sphere was computed by cross-correlation. As can be observed in Fig. 16, correlation is identical to a single sphere at low coverages when the magnetic momentum is high enough to form a uniform magnetic field. At occupancies greater than 50 %, the two attached cells have to be considered as individual dipoles in superposition and thus show a signal that carries small peaks in the center. This is shown schematically in Fig. 13c. In term, this causes a high signal deviation from the reference and thus a low degree of correlation.

## 4.2. The MRCyte Simulation Framework

In this work, also a analytical simulation framework that is capable of simulating the synergy of multiple microfluidic effects was developed. The comprehensive framework features magnetic, fluid dynamic and biochemical processes inside the utilized microfluidic channel which act on a particle. Foremost, material parameters was stored inside the “MRCyte” class, which range from channel and particle properties to binding and friction constants. Basic velocity, shear and magnetic field computations build the core of the presented program. Additionally, several dimensionless parameters such as the Stokes or  $Re$  or particle properties can be computed.

With that, simulations of the fluid dynamics that influence a single microbead as well as force-equilibrium computations for the same bead were carried out.

Capabilities - Simulation  
over sensor, particle distribution on surface, analysis of GMRTTool data single and differential, magnetic field per-

### 4.2.1. Fluid Fields inside the Microchannel

The simulation framework provided a quantitative generation of the Hagen-Poiseuille flow profile inside the microchannel with the numerical solution of Eq. 1.11. The simulated channel had dimensions ( $w \times h \times L$ )  $700\text{ }\mu\text{m} \times 150\text{ }\mu\text{m} \times 15\,800\text{ }\mu\text{m}$ . The flow rate was chosen at  $80\text{ }\mu\text{L min}^{-1}$ .<sup>1</sup> Tubing as well as time dependent effects were neglected. The simulated flow field ( $\mathbf{u}$ ) for the whole channel cross-section can be observed in Fig. 17a. Due to the no-slip boundary condition,  $\mathbf{u}$  is zero on the margin while the maximum of is reached in the geometric center. mean fluid velocity ( $\bar{\mathbf{u}}$ ) in the channel ensues  $12\,670.84\text{ }\mu\text{m s}^{-1}$ .

In contrast, computation of the flow gradient in vertical direction and scaling with  $\eta$  yield the shear stress field.(Fig. 17c) As the curvature of  $\mathbf{u}$  is zero in the channel center and maximal at the edges, the shear stress reaches highest values symmetrically at the horizontal edges of the channel.<sup>2</sup> Resulting, the net viscous shear  $\tau_{viscous} = \frac{\partial u}{\partial z}$  cancels out over the whole channel cross-section.

Additionally,  $\mathbf{u}$  and  $\tau_{viscous}$  acting on a  $8\text{ }\mu\text{m}$  diameter bead on the channel bottom were analyzed.(Figs. 17b and 17d). In the proximity to a wall and due to the applied boundary conditions,  $\tau_{viscous}$  enclosed by the bead surface is non-linear. Thus, the mean fluid velocity exposed to the bead amounts in  $\bar{\mathbf{u}}_p = 2241.59\text{ }\mu\text{m s}^{-1}$ , whereas  $\tau_{viscous,p}$  strains with  $4.93\text{ dyne cm}^{-2}$ .

<sup>1</sup> in accordance with the experimentally determined value

<sup>2</sup> Because the horizontal components of the gradients were neglected graceless

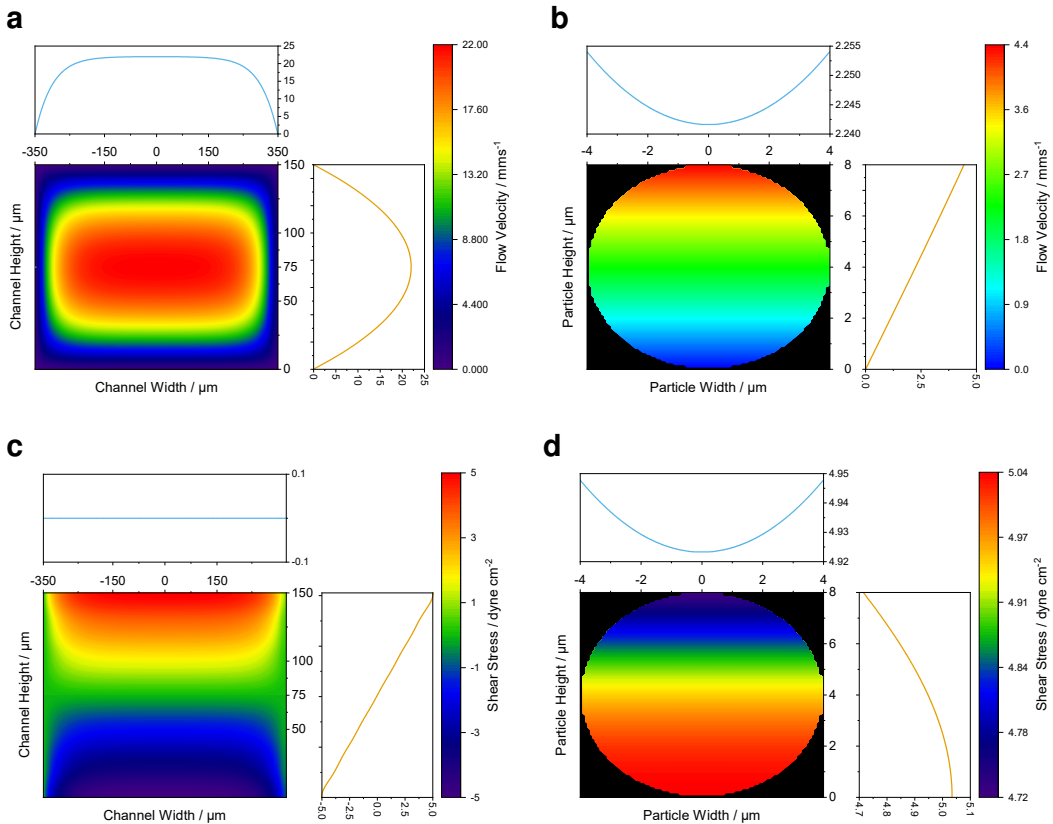


**Figure 17: Flow Field and Shear Stress Simulation of the utilized Microchannel**

Flow (a) and vertical shear (c) field inside the microchannel with dimensions ( $w \times h \times L$ )  $700 \mu\text{m} \times 150 \mu\text{m} \times 15800 \mu\text{m}$  for a flow rate of  $80 \mu\text{L min}^{-1}$  and with neglected tubing effects. The subplots on the right and top side show the mean horizontal and vertical profile in  $0 \mu\text{m}$  width and  $75 \mu\text{m}$  height, respectively. (vertical: —, horizontal: —) Due to the no-slip condition, the velocity at the walls equals zero and the shear is maximal. The maximum of the Hagen-Poiseuille profile is located in the channel center. Over the cross-section the mean flow velocity  $\bar{u}$  equals  $12670.83 \mu\text{m s}^{-1}$ . Resultingly, the net horizontal viscous shear  $\tau_{viscous} = \frac{\partial u}{\partial z}$  cancels out over the whole channel cross-section.

Flow (d) and vertical shear (d) field acting on a  $8 \mu\text{m}$  diameter bead on the channel bottom. The mean fluid velocity trapped by the bead profile results in  $\bar{u}_p = 2241.59 \mu\text{m s}^{-1}$ , whereas the viscous shear strains with  $\tau_{viscous} = 4.93 \text{ dyne cm}^{-2}$

## 4.2.2. Modelling the Force-Equilibrium of a Rolling Bead over a Biofunctionalized Surface

nice intro

With the supplier's parameters of a  $8\text{ }\mu\text{m}$  micromer-M bead (micromod Partikeltechnologie GmbH, Rostock) the corrected drag force on a bead on the bottom of the standard utilized microchannel resultes in  $463.65\text{ pN}$  for  $80\text{ }\mu\text{L min}^{-1}$ .

If the bead was functionalized with biotin under negligence of the differential equations for the association constants, the number of interacting groups would result in the present surface charges. Surface charge density resultes in  $1\text{ }\mu\text{mol g}^{-1}$  of carboxyl and amine beads as of the supplier's datasheet. Hence, a fully saturated bead is covered in 177 500 biotin molecules.

The streptavidin coverage of the channel floor was modeled in excess over the biotin ligands. The penetration depth was estimated by the size of several monolayers protein. As described by Wu and Voldman [9], an approach of  $30\text{ nm}$  is a reasonable quantity. In turn, the surfaces were in contact with  $1.51\text{ }\mu\text{m}^2$  which constitutes  $0.75\%$  of the  $8\text{ }\mu\text{m}$  bead surface. This reveals that 1329 biotin molecules can interact with the floor. A summation of the protein-bond force ( $\mathbf{F}_{protein}$ ) at  $5\text{ pN}$  to  $150\text{ pN}$  per streptavidin-biotin bond yields the resulting adhesion force with a magnitude of  $6.7\text{ nN}$  to  $199\text{ nN}$ .[74]

The binding force is in the same range as the perpendicular magnetophoretic force caused by the permanent magnet under the sensor chip ( $\nabla\mathbf{B} = 10\text{ T m}^{-1}$ ) as well as by the nickel-iron chevron structures on the chip ( $\nabla\mathbf{B} \approx 5\text{ kT m}^{-1}$ ). Clearly, in the near-field approximation the nickel-iron structures dominate  $\mathbf{F}_{mag}$  (Eq. 1.22). With the manufacturer given saturation momentum of one particle ( $1.12\text{ pA m}^2$ ), the magnetic attraction force eventuates in  $5.6\text{ nN}$ .

$$\mathbf{F}_{\parallel} = \mathbf{F}_{drag} - C_{rr} \cdot (\mathbf{F}_{mag} + \mathbf{F}_{protein} + \mathbf{F}_{grav} - \mathbf{F}_{shear}) \quad 2.7$$

$$C_{rr} = \sqrt{\frac{z}{d}} = \sqrt{\frac{30\text{ nm}}{8\text{ }\mu\text{m}}} = 0.0612 \quad 2.8$$

In order to merge this analytic force balance, all remaining forces have to be projected into the direction of Stoke's drag force ( $\mathbf{F}_{drag}$ ). (Eq. 2.7) This is achieved by the introduction of the rolling resistance factor ( $C_{rr}$ ) for a perfectly elastic surface. (Eq. 2.8) In

a first order approximation, the factor depends only on the approach ( $z$ ) and the bead diameter ( $d$ ). However, scientific literature about the rolling resistance of microbeads on microfluidic or protein covered surfaces does not exist yet to confirm this macroscopic factor for the microscale.

Scaling all orthogonal forces to the Stoke's drag force with  $C_{rr}$  yields a net positive result (154.08 pN) for an unfunctionalized surface ( $\mathbf{F}_{protein} \stackrel{!}{=} 0$ ) which indicates a rolling motion in flow direction. Notwithstanding, above a critical interaction number of 16 to 503 biotin-streptavidin bonds - for the respective release forces of 5 pN to 150 pN per linkage - the particle resists Stoke's drag force and adheres to the surface.

This behavior will be exploited in further measurements for "bead loss experiments" in order to measure a concentration difference with different degrees of biotinylated beads.

### 4.3. Reference Bead Surface Functionalization

After simulation of their respective coverages, biotin was titrated on 8  $\mu\text{m}$  reference beads with two different surface terminations in order to selectively bind MNPs with the counter-agent streptavidin to the surface. First, amine-microbeads were modified by sulfo-NHS-biotin. Second, carboxyl-beads were coated by amine-PEG<sub>2</sub>-biotin via EDC-NHS-activation. On the same beads Anti-IgG1-PE antibodies were titrated after the same coupling chemistry.

Subsequently, biotin-coated beads were analyzed in the flow cytometer in the by staining with Atto-488 (Ex: 500 nm, Em: 520 nm) coupled streptavidin. The antibody was already industrially modified with phycoerythrin (PE) and measured at 488 nm excitation and 585 nm emission wavelength. The gating was standardized by the strategy found in Sec. 3.3.4, Fig. 12. Subsequently, the MFI was computed and fitted with a Hill-function.(??) Stability of carboxylated and aminated beads and subsequently their respective modification protocols was evaluated for 12 days.

#### 4.3.1. Amine-Surface Biotinylation

As first approach, polystyrene copolymer microbeads with 8  $\mu\text{m}$  diameter were functionalized by (sulfo-)NHS-biotin after a standard protocol. A titration of the biotin reactant yielded a varying surface coverage as shown in Fig. 19a. During this one-pot-reaction, the water-soluble sulfo-NHS-biotin forms an amide linkage with the primary amine and 1-hydroxy-2,5-dioxopyrrolidine-3-sulfonate splits off as byproduct.

As can be seen from the SEM error-bars from the plot 19a, which were constructed from three true biological replicates, this process is highly reproducible. Therefore, an surface coverage in different grades of biotinylation could be obtained accurately with a adjusted coefficient of determination (adj.  $R^2$ ) of 0.981 for the resulting Hill fit ( - - - ).

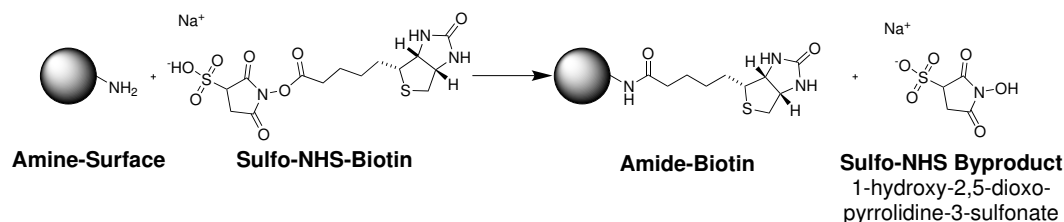


**Figure 18: Amine Bead Modification with Sulfo-NHS-Biotin**

An amine terminated bead brought into reaction with sulfo-NHS-biotin. Both form an amide linkage and bind biotin covalently to the surface. As byproduct the sulfo-NHS-ester splits off.

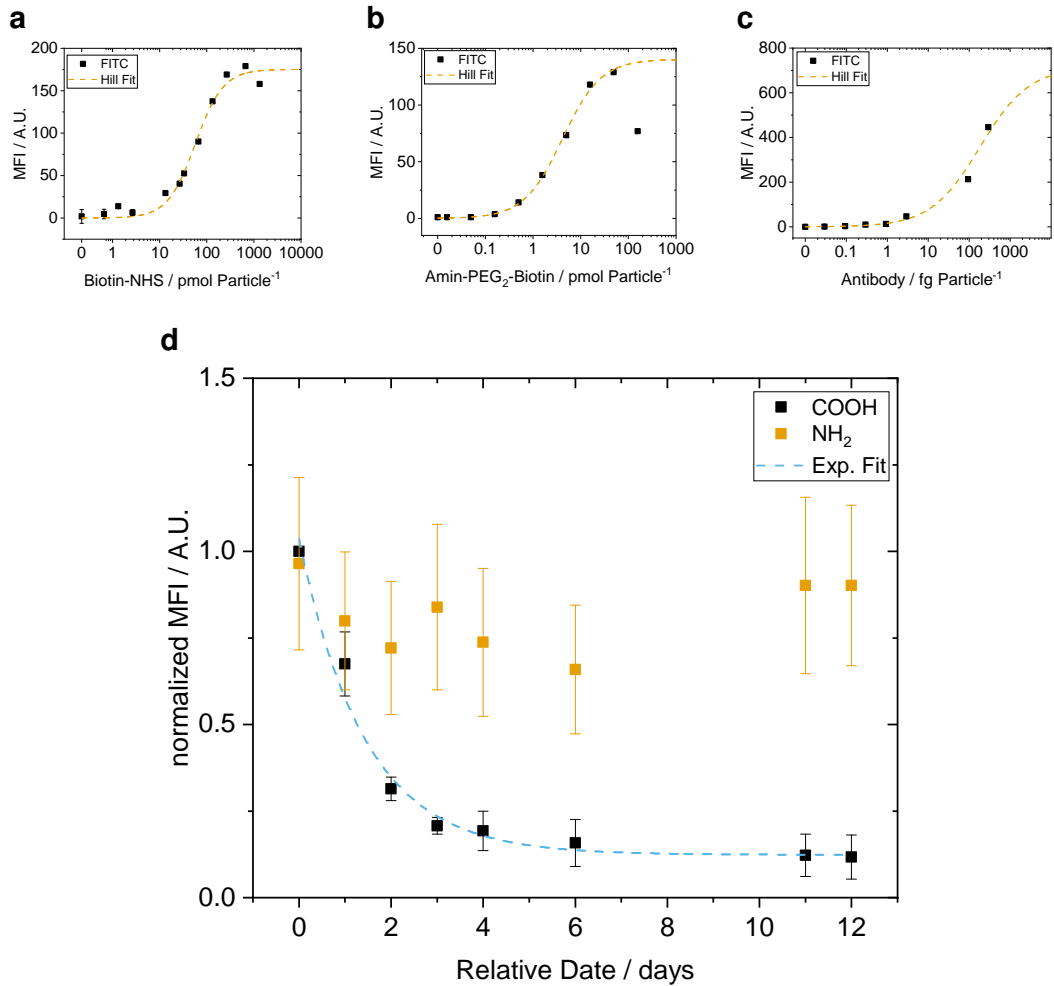


**Figure 19: Titration of Biofunctional Molecules on 8  $\mu\text{m}$  Particles**

Titration curves of NHS-biotin (a), Amin-PEG<sub>2</sub>-Biotin (b), and Anti-IgG1 (c) with their respective Hill fits. The corresponding fit parameters as well as the goodness factor are shown in Table 4a. (d) Stability analysis of functionalized carboxyl and amine beads over 12 days. The carboxylate particles show a exponential decrease with a half-life of 1.43 days as determined by the exponential fit. The respective parameters are shown in Table 4b.

a				b		
Param.	Hill 19a	Hill 19b	Hill 19c	Param.	Exp. 19d	
$V_{max}$	175.216 19	140.391 53	713.836 43	$A$	0.912 63	
$k$	57.367 13	4.126 61	182.830 11	$\tau_{decay}$	1.425 57	
$n$	1.474 88	1.074 93	0.724 58	$y_0$	0.123 69	
Adj. $R^2$	0.981 21	0.997 22	0.992 26	Adj. $R^2$	0.966 55	

**Table 4: Fit Parameters of Biotinylation**

(a) Coefficients for the Hill fits in Figs. 19a to 19c (b) Exponential fit coefficients for the stability analysis in Fig. 19d

### **Carboxylate-Surface Functionalization**

In a second approach, particles with opposite partial surface charge, mediated through carboxyl groups, have been functionalized. In turn, particles were pre-activated in EDC and NHS in MES/MEST buffer. There are two distinct reasons for the usage of MES based buffers rather than PBS or MACS. First, EDC has its reactive maximum at pH 5 to 6. Second, buffers containing primary amines (TRIS / glycine) or carboxyls (acetate / citrate) will quench the reaction and therefore limit the efficacy.

Afterwards, the beads were washed carefully and incubated with amine-PEG<sub>2</sub>-biotin. Here, poly(oxyethylene) (PEG) indicates a hydrophilic spacer arm between both functional groups and in this case has length of a two units. The full functionalization procedure is explained in more detail in Fig. 8.

As shown in Fig. 19b, particles were functionalized equally compared to carboxamide surfaces. However, the stability of carboxyl particles yields 1.43 days half-life in a continuous measurement over 12 days with a subsequent exponential fit. Additionally, both procedures show an outlier at high concentrations which could not be explained during the course of this thesis.

Third, carboxylated particles have been also functionalized with the Anti-IgG1-PE antibody. Again, a Hill-shaped titration curve was achieved, but due to the costly reagent a saturated surface coverage was not reached. (Fig. 19c)

Therefor, the fit curve has to be interpreted cautiously. Although it converged and represents the data with an adj.  $R^2$  of 99.2 %, the goodness of fit determined by the reduced  $\chi^2$  statistic results in a value of 278.1 which indicates an underestimation of the error variance.

#### 4.4. Concentration Measurements in MRCyte

Driving factor for the concentration measurement is the absolute count of immunomagnetically labeled cells in diluted or whole blood which is not possible in today's optics-based devices due to the excess of RBCs.[87] Therefore, with the in Sec. 2.3 described sensor setup, absolute concentrations of magnetic reference beads were attempted to measure.

Consequently, beads with acrylate surface were pumped through a microfluidic channel with a permanent magnet underneath. The magnet drew every magnetic particle to the ground, where they were focused on the sensor bridge and subsequently measured there. From the received signal several parameters such as peak amplitudes, locations, zero-crossings, and relative distances between each other were computed. (Fig. 20) However, for a concentration measurement mostly the correct detection of a signal from the noisy stream or from a superposition of multiple simultaneously measured particles was critical. The related error sources and countermeasures will be elaborated in Sec. 4.4.1.

By measuring the absolute concentration with a commercially available flow cytometer (MacsQuant 10, Miltenyi), a reference bead count was established. In a pre-test, beads were taken directly from the microcentrifuge tube, after pumping through a syringe, and after pumping through a syringe with 10 cm of connected through tubing (ID 0.5 mm, RS Chemicals). Afterwards, they were counted in the flow cytometer in equal volumes. Additionally, two different buffers - MACS and PBS - and two different surface terminations were used. Both buffers are based on phosphate buffered saline (PBS). Notwithstanding MACS contains 2,2',2'',2'''-(ethane-1,2-diyl)dinitrilo)tetraacetic acid (EDTA) as chelator for divalent ions, Tween 20 - a non-ionic surfactant -, and an azide-based stabilizer. Hence, the wetting of surfaces and the electrostatic interactions of these buffers differ. The same properties were varied on the bead surface by choosing acrylate- and biotin-terminated beads.

In Fig. 21, a trend (without statistical confidence) can be observed that shows a decrease in particle counts after every additional surface which beads could potentially interact with. In term, a correct count in absolute numbers seems out of range. However, a calibration of the system with the flow profile inside the channel to compensate for losses subjected to connectors and magnetic enrichment structures was carried out

successfully.

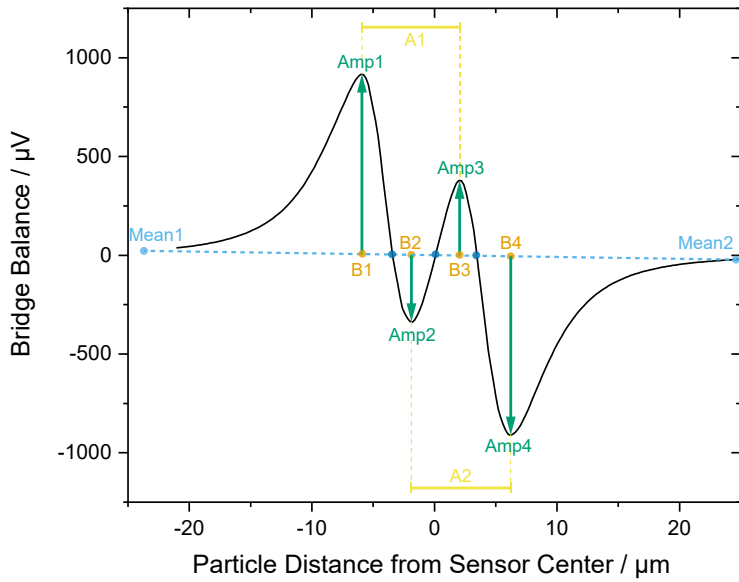


**Figure 20: Example Signal of Magnetic Measurement**

Signals generated from the Wheatstone bridge sensor setup feature a certain shape which allows for several measures. In case the overall signal stream carries a constant or linear offset, it is scaled to the means before and after the detected peak pattern. (Mean1, Mean2) The x- and y-positions of each peak are denominated by B1-4 and Amp1-4, respectively. The crossings of the signal through the linear connection of both means are denominated by n1-3 (in the figure by ●). Further, the difference between the equally oriented peaks B3-B1 and B4-B2 give a measure for the homogeneous movement of the measured object and are called A1 and A2 each. From these values the overall velocity  $v$  can be approximated because the GMR bridge distance ( $d_{GMR}$ ) and sampling frequency ( $f_s$ ) is fixed precisely. Analogously, the magnetic diameter of a dipole is computed by the mean of the differences B2-B1 and B4-B3.

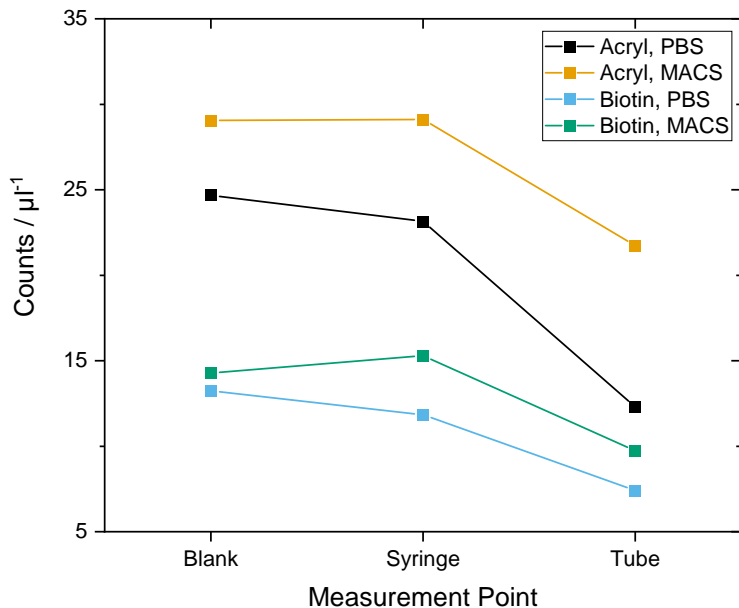


**Figure 21: Bead Loss Evaluation in Connectors**

Bead concentrations measured in equal volumes in the flow cytometer after being pumped through a syringe or a syringe with connected tubing. The blank sample was measured directly from the stock solution. Additionally, electrostatic and surface tension related effects were resolved by the usage of different buffers and bead surfaces.

#### 4.4.1. Measurement Error Sources and Calibration of Flow Field

In order to account for the bead losses due to the tubing connectors, the Hagen-Poiseuille flow profile, and magnetophoretic enrichment structures, the measured bead concentration was corrected in two different approaches.(Eq. 4.9) On the one hand side, the typical assay correction to the ground truth by a constant linear fit correction factor ( $C_{const}$ ) computed from the blank population was established. On the other side, a velocity correction factor ( $C_{velocity}$ ) compared the mean fluid velocity ( $\bar{u}$ ) to the bead velocity ( $v_c$ ).

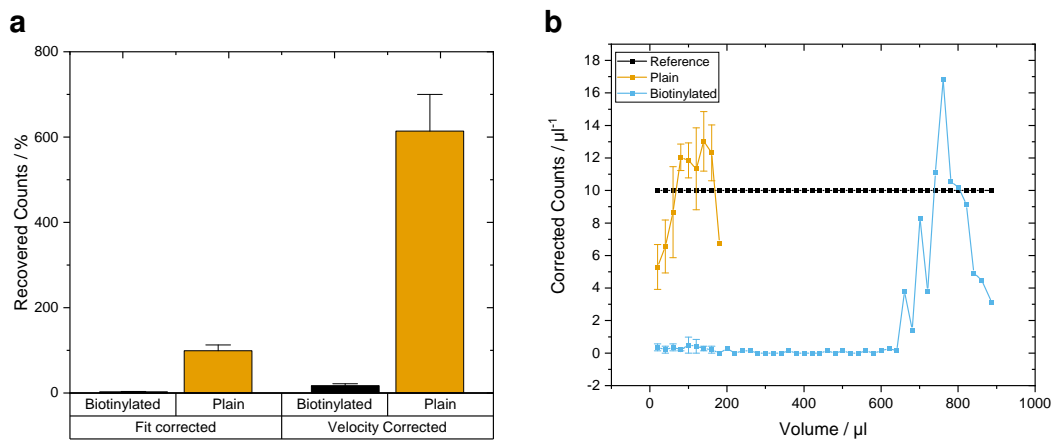
$$c_{beads, expected} = c_{beads, measured} \cdot C \quad 4.9$$

The  $C_{const}$  relates a reference count in the optical flow cytometer to the measurement in the magnetic flow cytometer.(Eq. 4.10) Equally-adjusted bead concentrations in the samples allow for a correction to the reference system. However, for an assay usage the initial concentration of beads either has to be known precisely or has to be irrelevant, for example in regards of a standardized measurement procedure. Besides,  $C_{const}$  provides a reliable and generalizable option for correction.

$$C_{const} = \frac{c_{beads, standard\ procedure}}{c_{beads, MRCyte}} \quad 4.10$$

$$v_c = 2 d_{gmr} \frac{f_s}{n_3 - n_1} \quad 4.11$$

$$C_{velocity} = \frac{\bar{u}}{v_c} = \frac{Q}{A \cdot v_c} \quad 4.12$$



The  $C_{velocity}$  relates the effective particle velocity to the total fluid velocity in order to eradicate flow profile provoked effects.(Eq. 4.12) Whereas  $\bar{u}$  was determined by flow rate ( $Q$ ) through a cross-sectional area ( $A$ ) of the channel,  $v_c$  was analyzed from the measured signal stream. Here, the intrinsic GMR bridge distance ( $d_{GMR}$ ) was divided by the time difference where the bead passed exactly over a GMR-element.(Eq. 4.11) These specific timepoints are visible as dimensionless zero-crossings  $n_1$  and  $n_3$  in the signal and can be converted by scaling with the sampling frequency ( $f_s$ ) into the time domain.

However, if the bead velocity is not solely dependent on fluid dynamic effects - espe-

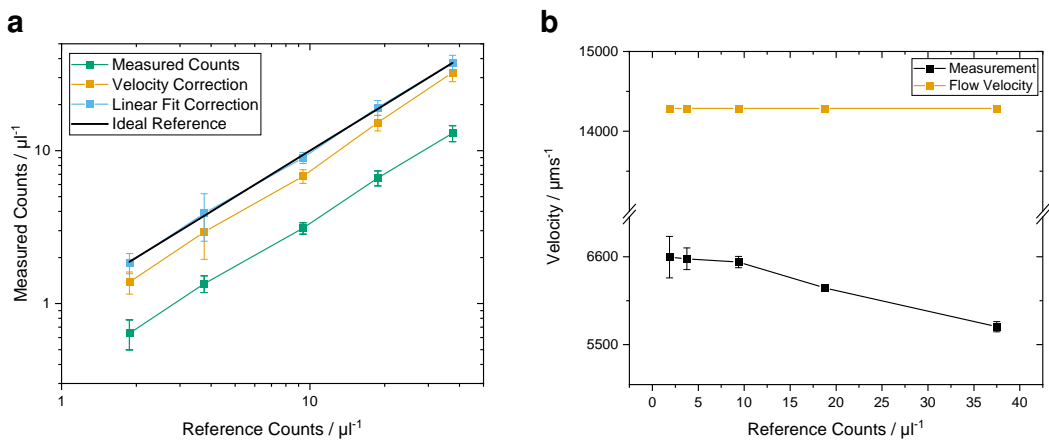


**Figure 23: Absolute Concentration Measurements**

(a) Mean and standard deviation of the concentration measurement from three independent measurements. The uncorrected measurement shows a highly reproducible and linear count over the dynamic range of almost two decades. (—■—) The ideal reference from the flow cytometer is depicted in (—). Correction with  $C_{velocity}$  (—□—) yields at a factor of 2.261 09 which is 21.7 % more imprecise than  $C_{const}$  at  $2.888\ 33 \pm 0.080\ 75$ . (—△—) (b) Mean and SEM of the  $v_c$  estimation from the signal. For higher concentrations, the measured velocity becomes inaccurate thus distorts the correction factor.

cially in the light of surface functionalizations -  $C_{velocity}$  can not be applied to experiments robustly. This is depicted in a sample experiment with a protein covered surface in Fig. 23a. By definition, the  $C_{const}$  can not be well above than 100 % whereas the count correction by  $C_{velocity}$  differs by 600 % through variations in the velocity measurement.

An adaptation of these corrections to real measurements are depicted in Fig. 23. In a measurement where 300  $\mu\text{L}$  were dispensed into the magnetic flow cytometer with a defined particle concentration the counts were analyzed and corrected according to above. This time, the channel had a cross-section of 700  $\mu\text{m} \times 50 \mu\text{m}$  (w x h) and  $Q$  was set to 30  $\mu\text{L min}^{-1}$ .

Apart from a reproducible count over the dynamic range of almost two decades, both

correction factors ameliorated the present data.  $C_{const}$  amounted in an optimum  $2.89 \pm 0.08$  while  $C_{velocity}$  centered around a mean of 2.26. Consequently, the velocity correction was misguided by 21.7 % for the advantage of requiring no *a priori* knowledge about the measurement.

Another peculiarity of  $C_{velocity}$  can be observed in Fig. 23b. While the analyzed velocity is stable for less than  $10 \mu\text{L}^{-1}$ , a linear decrease is visible for higher concentrations. This is a consequence when signals of beads start overlapping if these are flowing over the sensor in a close vicinity. Hence, the disturbed signal sensitizes the parameter reconstruction to errors such as false peak-identification.

#### 4.4.2. Concentration Measurement in Diluted Whole Blood

The same concentration measurements from before were now carried out in whole blood samples. Here, the reference count can be attained only below the experimentally determined critical concentration around  $10 \mu\text{L}^{-1}$ . (Fig. 24) An insignificant discrepancy could be perceived in different volumetric blood to buffer dilutions of 1:1 and 1:20, respectively. This provides evidence for the measurement's independence from the blood concentration in buffer.

However, a significant difference between counts was discovered between a  $150 \mu\text{m}$  high channel, where  $C_{velocity}$  can be determined accurately, and a  $50 \mu\text{m}$  high channel, where the correction yields a great error to the reference. This may be subjected to an increased probability of collisions from beads with blood cells and hence a decreased velocity which in turn leads to a higher correction factor. Another explanation approach could be the transition from *Newtonian* to *Non-Newtonian* fluid dynamics in smaller cross-sections, which could likewise be influenced by the Fåræus effects mentioned in Sec. 2.1.3.

#### 4.4.3. Surface Magnetization of Biofunctionalized Beads

Here, the previously surface-modified polystyrene beads were magnetized with MNPs and counted in the magnetic flow cytometer. Originally, four different magnetic nanoparticles have been tested. Albeit, both nanomag-D-spio 100 nm (micromod Partikeltechnologie GmbH, Rostock) and dynabeads MyOne Streptavidin C1  $1 \mu\text{m}$  (ThermoFisher scientific, Waltham, USA) showed inconclusive results.

First, BNF-Dextran-redF-streptavidin 100 nm MNPs (micromod Partikeltechnologie GmbH, Rostock) were attached to the non-magnetic beads after the protocol in Sec. 3.3.4.

Then the magnetizability was examined qualitatively in a magnet stand. Thereby, the particles were considered magnetically labelled if a pellet was visible after 10 min. Afterwards, the concentrations were measured with the optical flow cytometer and adjusted to  $10 \pm 1 \mu\text{L}^{-1}$  accordingly.

The subsequent measurement of  $300 \mu\text{L}$  in the magnetic flow cytometer is shown in Fig. 25. In Fig. 25a the peak difference C1 (= Amp2 - Amp1, Fig. 20) is presented against the biotinylation degree. Independent experiments of 100 % and 68 % biotinylation show a certain amplitude difference. The respective fluid and particle velocities in Fig. 25b provide an explanation for the behavior. The fluid velocity had to be adapted during the course of the experiments from  $80 \mu\text{L min}^{-1}$  to  $10 \mu\text{L min}^{-1}$  in order to receive stable counts.

Keeping this in mind leads to the fact that - although only two biotinylation coverages were measured - four distinct magnetizations are represented here. Both 100 % samples show slow but plausible velocities and can therefore be correlated with differing magnetic momentum. Beads with 68 % show an exceptional velocity and can hence either be considered as noisy background or a very weakly magnetized particles that are not pulled to the channel bottom completely. This could also explain the decline in amplitude, which can be correlated to magnetic dipole moment as well.

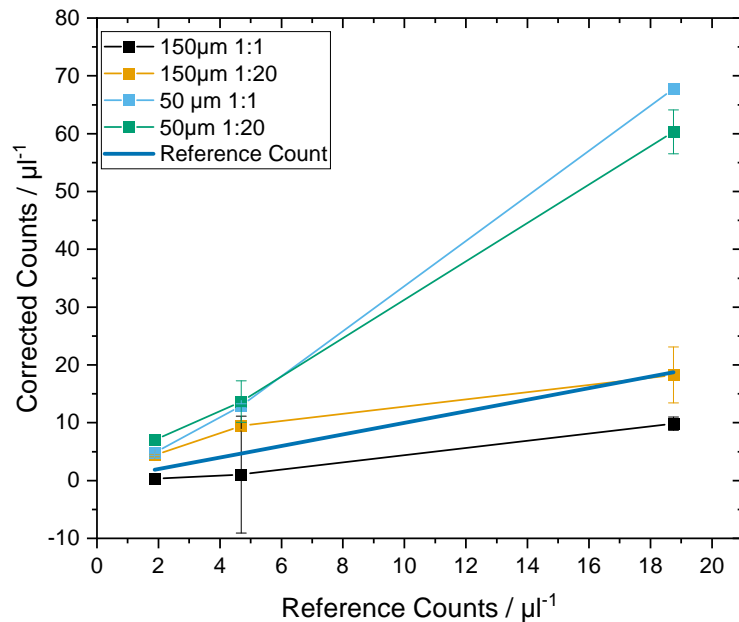


**Figure 24: Absolute Concentration Measurement in Blood Samples Under Varying Channel Height**

Velocity corrected concentration measurements for two different blood dilutions and channel heights. While  $C_{velocity}$  works for high channels in all tested concentrations, it does not work for high concentrations in  $50 \mu\text{m}$  high channels. This is probably a result of bead-cell collisions and the resulting path interruption.

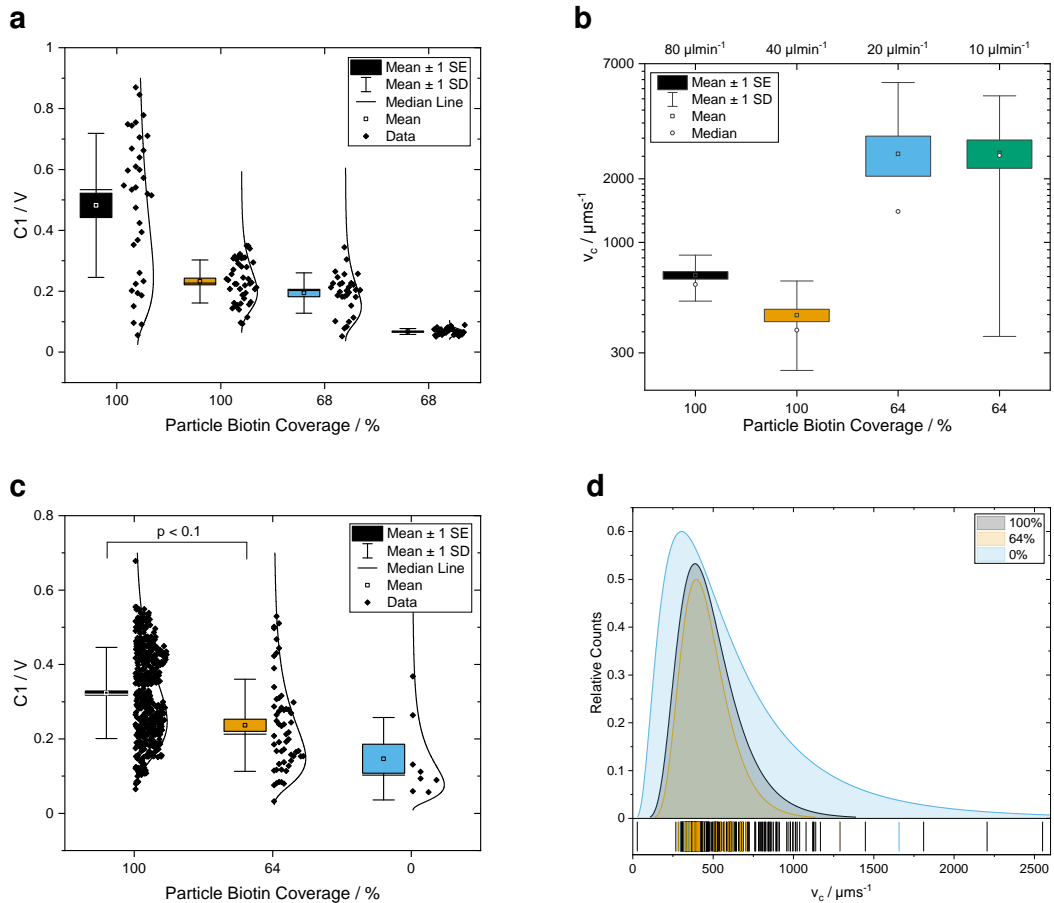


**Figure 25: Bead Coverage Assay with Magnetic Streptavidin Nanoparticles**

Magnetic flow cytometry data from  $8\text{ }\mu\text{m}$  polystyrene sphere which were biotinylated in different degrees and subsequently coated with BNF-Dextran-redF-streptavidin 100 nm MNPs (a,b) or SV0050 50 nm streptavidin MNPs (c,d). (a) Signal amplitude of the counts with various flow rates 1.  $80\text{ }\mu\text{L min}^{-1}$  2.  $40\text{ }\mu\text{L min}^{-1}$  3.  $20\text{ }\mu\text{L min}^{-1}$  4.  $10\text{ }\mu\text{L min}^{-1}$  (b) Reconstructed velocities of the respective populations. The 100 % biotinylation shows plausible velocities, whereas the 68 % sample can either be considered as noisy background or very weakly magnetized particles. (c) Signal amplitude with  $80\text{ }\mu\text{L min}^{-1}$ . A correlation between biotinylation degree and magnetic momentum can be assumed at a p-value  $p < 0.1$  (d) Velocity distributions of the samples. As postulated, the mean velocities do not differ, moreover, are enveloped by the blank sample.

Second, SV0050 50 nm streptavidin MNPs (OceanNanotech, San Diego, USA) were deposited after the equal procedure on  $8\text{ }\mu\text{m}$  polystyrene beads. These experiments show the expected result of declining peak amplitude at lower biotinylation and constant velocity throughout. (??) At a p-value smaller than 10 %, the high populations differ significantly from each other while the log-normal fits match the histograms with a adj.  $R^2$  of 0.94.

Two hypotheses can be drawn now from this result. On the one side, OceanNanotech MNPs could posses more magnetic momentum per particle, which favors the robust measurement. On the other side, streptavidin or MNP size could influence the saturation of all available biotin sites of the particle.

#### 4.4.4. Count Stability

In this section the results of beads rolling a neutravidin-covered channel surface will be discussed. In order to measure the interaction properties diligently, beads were functionalized with biotin at several saturation degrees ranging from 0 % to 100 % total coverage of the available surface charges. Measurements for absolute counts as well as their time stability were carried out at  $80 \mu\text{L min}^{-1}$  in a microchannel with cross-section  $700 \mu\text{m} \times 150 \mu\text{m}$  (w x h). Fig. 26a shows the absolute, linearly corrected counts determined by the magnetic flow cytometer, with a defined particle concentration of  $7.8 \mu\text{L}^{-1}$  to  $10 \mu\text{L}^{-1}$ . Clearly, a significant yes-no answer can be established by fully- vs. non-functionalized beads. Also, this measurement was highly reproducible with three different chip setups and measurement days. For approximately  $\frac{2}{3}$  biotinylated beads, a gradation in counts can also be observed. However, due to the instability of the channel surface over the course of many sequential measurements, additional experiments have to be conducted to reinforce these results.

An evaluation of the time-domain distribution of the counted beads shows a very stable baseline for fully biotinylated beads with a recovery in the single digit range per unit volume. In the negative control of unbiotinylated beads, also a noisy mean count around 100 % can be observed.<sup>3</sup>

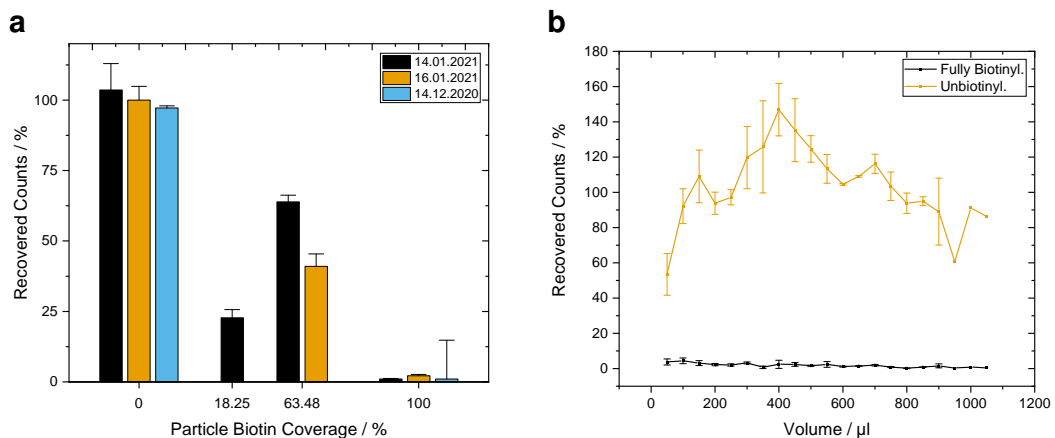


**Figure 26: Reproducibility of Concentration Measurements with Saturated Neutravidin Surfaces**

Biological replicates of concentration measurements with the magnetic flow cytometer. The channel surface was modified with  $1 \text{ mg mL}^{-1}$  neutravidin over night. (a) Mean and SEM of  $C_{const}$  adjusted counts for various biotinylation degrees. (b) Time series of the mean from the three measurements on the left. Biotin-beads are captured completely, thus very few counts are detected. (—) The unbiotinylated sample shows the initial ascent due to the in Sec. 4.4.1 discussed error which is related to the filling of the magnetophoretic structures. (—)

Say something about velocity

<sup>3</sup> The shown data corresponds to the mean of three measurements from Fig. 26a

#### 4.4.5. Differential Counting Setup

With regard to the necessity of correction factors in order to resolve the ground truth of a concentration measurement, a different magnetic flow cytometer setup has been evaluated. Here, two fully assembled sensors with PCBs were stacked on top of each other and connected in series. This was expected to yield two beneficial effects.

First, one permanent magnet underneath the lower sensor chip should supply both chips with enough gradient field to pull beads to the respective channel bottom. Second, simultaneous signal acquisition should act on the one side as a time-of-flight detector with a relatively long transport distance. On the other side, a differential concentration measurement was envisioned between both chips. Therefor, the hypothetical optimum parameter set could be reached when the relative concentration measurement yielded identity:

$$\frac{c_{\text{top sensor}}}{c_{\text{bottom sensor}}} = 1 \quad 4.13$$

The system comprises of two separately assembled sensor PCBs with nylon spacers between the positional screws.(Fig. 27) A 3 mm hole was drilled into the top PCB carefully between the strip lines to minimize the tubing length from the top chip outlet to the bottom chip inlet. After the build-up of the differential counting system,<sup>4</sup> the hysteresis of both sensor elements was maximized for sensitivity and the concentration was measured against a reference from the optical flow cytometer.

#### Sensitivity Calibration

Initially, the permanent magnet was adjusted in three linear directions in order to maximize the magnetic sensitivity of both Wheatstone bridges. Schematically, this can be envisioned as a placement of the whole top as well as the whole bottom bridge configuration into the operational range of the magnet, which is indicated by the blue triangle.

Then, the hysteresis of both outermost and one centered sensor was optimized for their full coverage and sensitivity. The recorded values for a sole optimization of the top or bottom sensor array with a height variation of the utilized nylon spacers are shown in Figs. 27b and 27c. Apparently, the optimized sensor exhibits a monotonously higher magneto-resistive effect (MR effect) than the disregarded bridge. Nevertheless, the complete sensor setup features a MR effect well above 7.2% which is acceptable both

---

<sup>4</sup> as described in Sec. 3.1.3

for measuring immunomagnetically labeled cells and magnetic microbeads. Furthermore, the homogeneity of the interspersing magnetic field can be monitored in the triangular shape of every acquired curve in the sensitivity plots. As the field vectors of  $\mathbf{B}$  start to disperse at the outsides of the illustrated blue area in Fig. 27c, the outer sensor regions are not located completely inside a uniform field and get distracted by non-perpendicular field components.

Additionally, no influence of any spacer height could be discovered. The difference in MR effect varied insignificantly in  $0.14 \pm 0.60\%$  of MR effect.

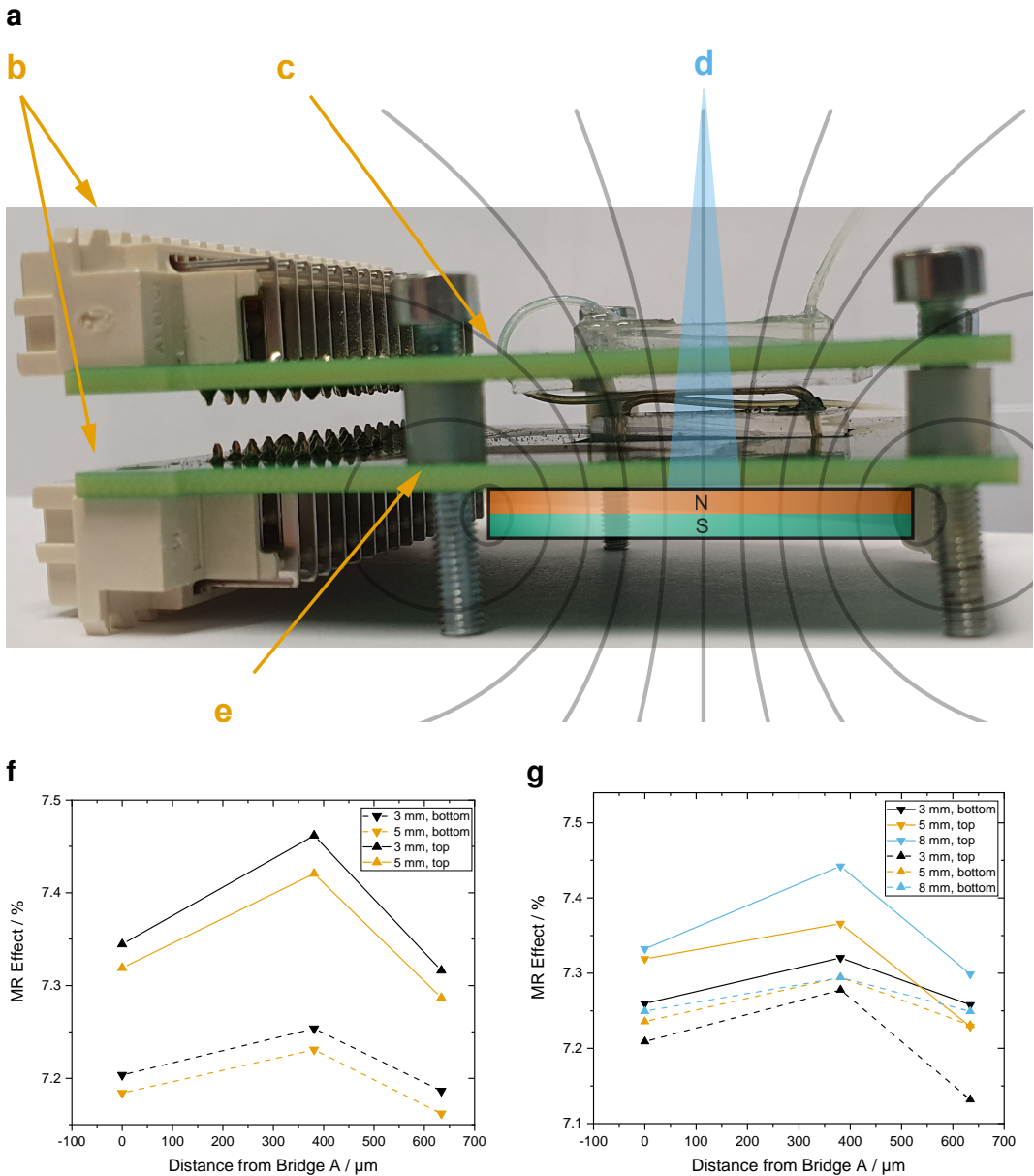


**Figure 27: Hysteresis Calibration for Stacked PCB Setup**

(a) Differential measurement setup: the system comprises of two separately assembled sensor PCBs (b) with nylon spacers (e) between the positional screws. (f) A hole with 3 mm diameter was drilled between the strip lines to connect the top chip outlet to the bottom chip inlet and minimize tubing length thereby. Schematically, a permanent magnet is placed below the bottom PCB.(d) The field line density respectively the area with negligibly differing field vectors is shown in the blue triangle. Because the adjustment is always carried out for a single bridge at once, this causes a systematic error.

The magneto-resistive effects of both sensors, calculated from their hystereses, are depicted for top and bottom sensors, respectively. Whereas the hysteresis was optimized for the centered sensor bridge (D or E) on the top sensor in (f), it was optimized for the bottom sensor in (g). Additionally, the height of the nylon spacers was varied from 3 mm to 8 mm but showed no statistical correlation.

## Concentration Measurement in Buffer Solution

Due to the single utilized permanent magnet for two sensors, another field related issue arose during concentration measurements. This requires a step back inside the general functionality of the magnetophoretic enrichment:

Any bead flowing at an arbitrary position in the microchannel experiences a positive magnetic force by the gradient of the magnetic flux density caused by the permanent magnet which pulls perpendicular to the bottom surface. Upon coming in close proximity to the lower boundary, a gradient provoked by the lithographic nickel-iron structures starts to gain strength with the third power of the distance. This causes the beads to attach to the bottom firmly and enforces their rolling behavior. However, a fragile equilibrium between magnetophoresis and drag has to be maintained slightly in favor of Stoke's drag force for a continuous rolling motion. This ideal state is a narrow space in between two boundary cases.

First, if drag force outnumbers magnetophoresis, the beads will not migrate to the channel bottom in the top chip and hence cause a depressed concentration measurement on top. Second, if magnetophoresis outnumbers drag so that particles flow steadily in the top channel, the beads in the lower channel will stop rolling and adhere statically. In effect, the lower concentration measurement is compromised.

In order to find the flow rate for the optimal ratio between drag and magnetic force, mea-

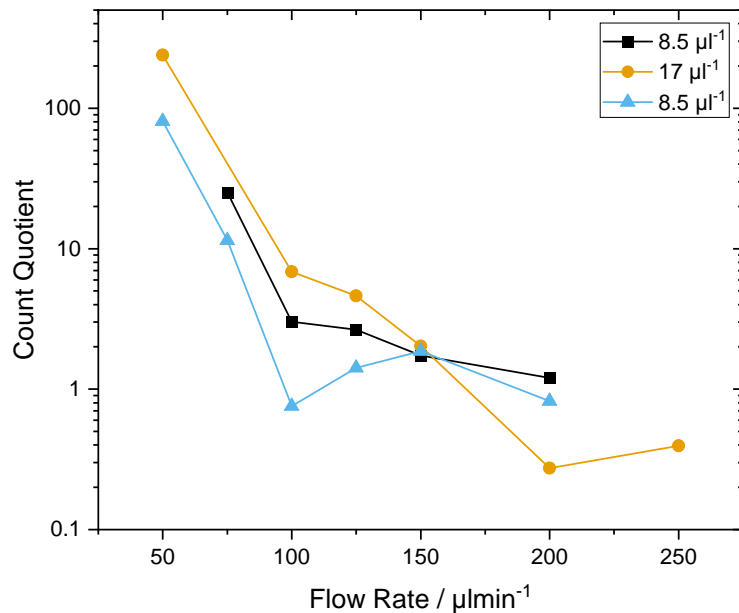


**Figure 28: Optimal Differential Counting Flow Rate**

Losses in different buffers and bead surfaces.

surements were performed with bead concentrations ranging from  $6.5 \mu\text{L}^{-1}$  to  $34 \mu\text{L}^{-1}$ .<sup>5</sup> The quotient of both measured concentration was determined after Eq. 4.13 and plotted in Fig. 28. Although, the optimal quotient value would have been 1 theoretically, an ideal overlap was found for a flow rate of  $150 \mu\text{L min}^{-1}$ . However, the difficulties in assembly and operation inhibited a further usage in experiments.

---

<sup>5</sup> The raw data is shown in Fig. 33

## 4.5. Surface Modification and Biofunctionalization of the Sensor Chip Substrate

In consideration of the problems of surface instability analyzed in Sec. 4.4.1 and to avoid additional uncertainties in the experimental validation of the model from Sec. 4.2.2, a covalent functionalization of the sensor surface with neutravidin was carried out. Initially, a plate reader experiment for a qualitative statement about the shear-force stability of protein adsorption was performed. Then, different functionalization approaches with piranha and HF were tested with pure glass, PDMS, and eventually  $\text{Si}_3\text{N}_4$ . As sophisticated chemical analyses were hardly available, the validation of these procedures was limited to indirect measurements such as tensiometry, fluorescence microscopy, and quantitative bead capture assays.

### 4.5.1. Physisorption

In order to quantify the adsorption stability for fluorescently-labeled, physisorbed streptavidin molecules, sensor chips were cut into  $10 \text{ mm}^2$  pieces and glued to the bottom of a 96-well plate. Subsequently, they were equilibrated with PBS and incubated with  $1 \text{ mg mL}^{-1}$  over night. Each measurement was corrected for a blank substrate as well as the negative control with plain PBS buffer and normalized subsequently.

Each measurement in the plate reader showed a significant surface decrease to a mean level of 28 % from the original fluorescence.(Fig. 29) Whereas proteins desorbed from both crystals after the first washing steps equally,  $\text{Si}_3\text{N}_4$  outperformed  $\text{Al}_2\text{O}_3$  as more stable in steady state. (34.8 % vs. 27.5 %) However, no quantitative hypothesis can be formulated by these numbers due to the nature of their indirect measurement. Hence, the protein activity which is the crucial quantity for any bead rolling remains questionable. Nevertheless, a qualitative proposition is strongly confirmed that unspecifically adsorbed proteins are removed from any of both surfaces rapidly.

### 4.5.2. Covalent Attachment

Now, the results of several covalent surface modification procedures with various substrates are presented. Foremost, glass was used as main carrier material. On glass established protocols were then brought onto PDMS and  $\text{Si}_3\text{N}_4$  chips. As main functionalization protocol, an activation in 7:1 piranha was carried out for 30 min. Then, the substrate was rinsed, incubated in 2 % APTES solution and in PAA subsequently after the protocol described in Sec. 3.3.2. Then a  $150 \mu\text{m}$  microfluidic channel was

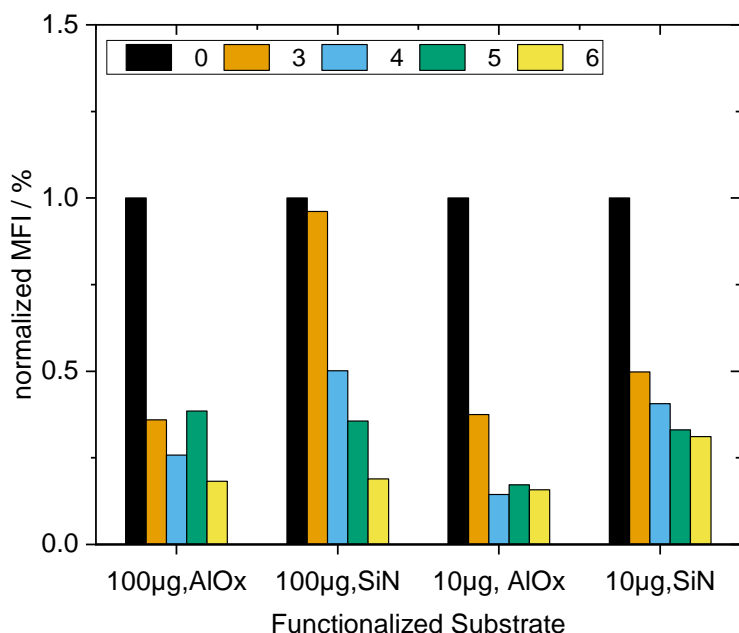


**Figure 29: Surface Adsorption Stability of Neutravidin on  $\text{Si}_3\text{N}_4$  and Aluminium oxide ( $\text{Al}_2\text{O}_3$ )**

Plate reader measurement with  $3 \text{ mm} \times 3 \text{ mm}$   $\text{Si}_3\text{N}_4$  and  $\text{Al}_2\text{O}_3$  samples which were incubated with  $100 \mu\text{g}$  and  $10 \mu\text{g}$  streptavidin-atto488, respectively. The samples were subsequently washed with  $200 \mu\text{L}$  PBS carefully. Fluorescence intensities were corrected with a blank substrate, the autofluorescence of PBS, and normalized eventually. Every surface reaches a mean fluorescence level of 28 % after few washing steps.

glued to the functionalized substrate and eventually filled with  $1 \text{ mg mL}^{-1}$  of neutravidin or streptavidin-atto488, if fluorescent labeling was intended. A constant flow rate of  $80 \mu\text{L min}^{-1}$  was selected for the bead capture assays under the light microscope. The general process chain is depicted in Fig. 30.

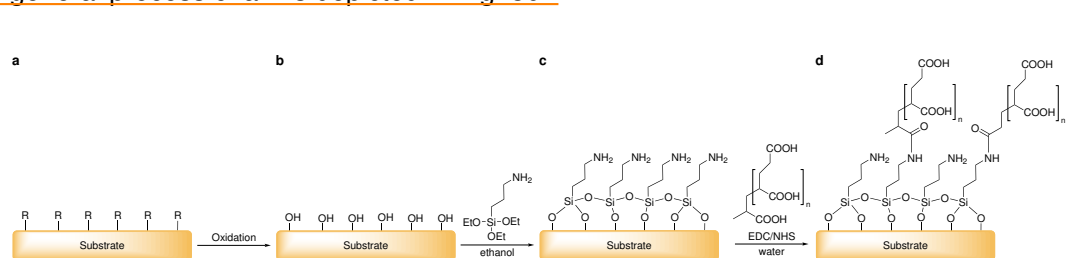


**Figure 30: General process chain of chemical surface modification**

Any substrate with various surface groups R (a) is oxidized to exhibit hydroxyl groups.(b). Then a silane SAM is attached (c) and subsequently modified by carbodiimide chemistry with PAA. (d)

However, too few chemical replicates have been generated so that a substantial prediction could be established.

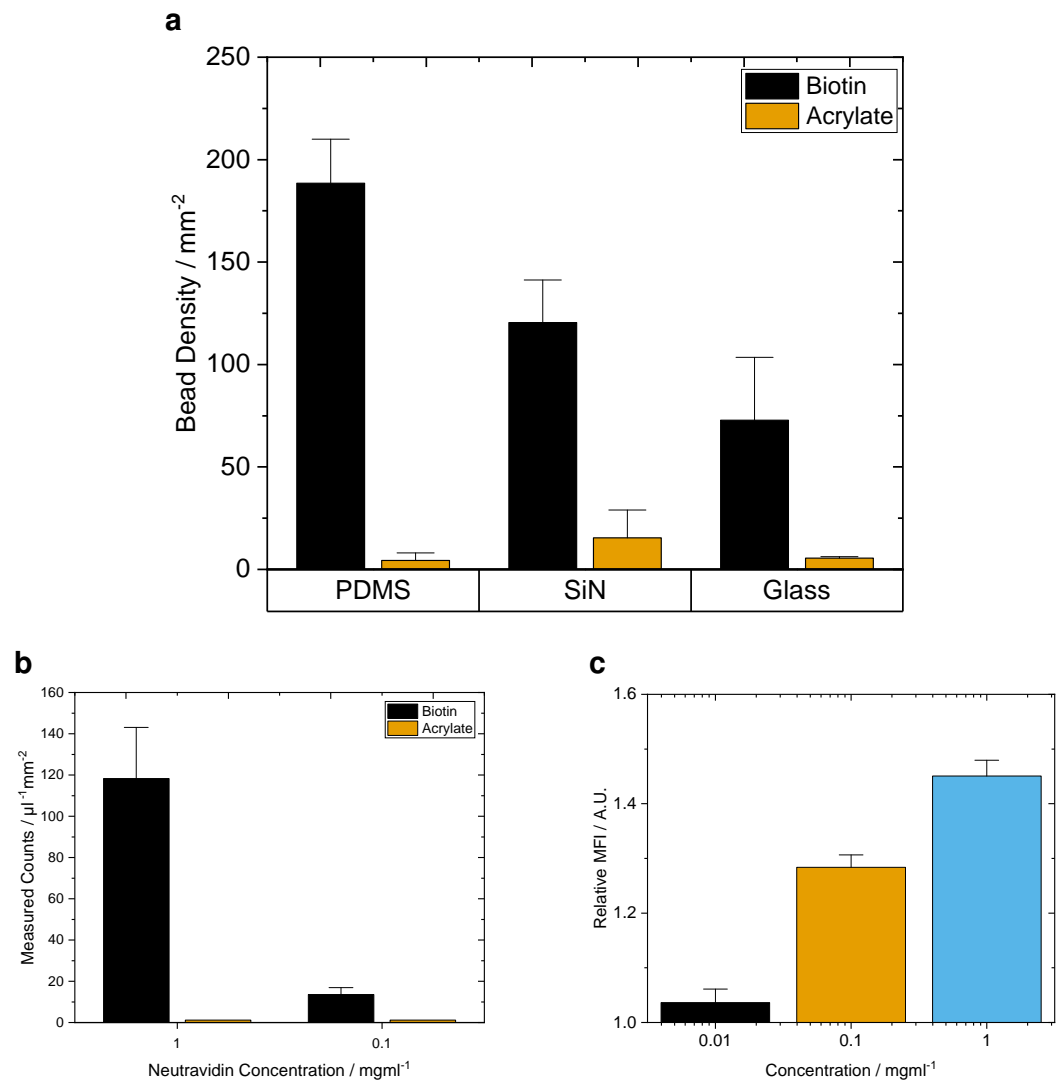


**Figure 31: Optical Bead Capture Assay and Titration Fluorescence Analysis**

(a) Density measurement of captured beads on the covalently functionalized surfaces of PDMS,  $\text{Si}_3\text{N}_4$  and glass. PDMS shows the most promising density. (b) Titration of neutravidin on covalently functionalized glass with a subsequent analysis by a bead capture assay. (c) Titration of streptavidin-atto488 on covalently functionalized glass with subsequent fluorescence microscope imaging.

## 5. Discussion

Start by briefly summarizing your major findings, but without repeating exact data from the Results. This makes your novel information clear to peer reviewers and, later on, readers. It also forces you to decide which findings you should focus on in the Discussion. Thereafter, discuss possible underlying mechanisms. Why did you get these results, what is happening? Mechanisms, particularly molecular mechanisms, have very high “impact” in the natural sciences.

Next, compare your findings to those of other relevant publications and attempt to explain any discrepancies. If your findings disagree with those of others in the area, compare their publication to your own manuscript in minute detail, looking for any differences (especially in methodology) that might explain the discrepancy.

Consider the possible limitations of your own study—paradoxically, most reviewers consider an awareness and openness about potential weaknesses as a strength. However, do not forget to emphasize strengths as well.

Discuss the possible consequences of your observations and/or future investigations required or motivated. Be as concrete as possible about future perspectives. As in the abstract, writing the equivalent of “more research is needed” is meaningless—more research is always needed. Describe the hypotheses, questions or mechanisms that need to be investigated and/or methods that should be applied, concretely and concisely. And, of course, if your research findings have potential practical implications, discuss these in some detail as well.

Finally, state your conclusions—have you supported or rejected the hypothesis you posed, or obtained an answer to your research question?

Deriving Navier-Stokes equation by the Cauchy momentum equation is complex and harbors several sources of error. First, an incompressible Newtonian fluid as well as channel boundary is assumed. The used water suspensions are approximated with negligible compressibility, which is not true for the real case. Also, for blood or other shear-thinning fluids these deviations are prone for high errors.

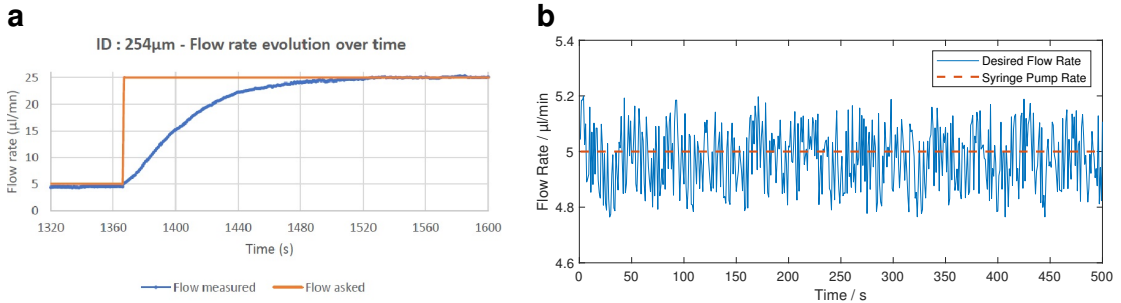


**Figure 32: Syringe Pump error sources**

Set flow rate: , Real Flow Rate: a Transient step answer of a syringe pump through a microtube with 254  $\mu\text{m}$  inner diameter. b Steady state flow rate error around the desired  $5 \mu\text{L min}^{-1}$  dispensing rate. A sinusoidal behaviour caused by the microstepping can be observed. [88]

Then, the divergence relation of the respective viscous stress (eq. 1.7) does not hold for non-uniform viscosity  $\eta$ .

For later studies in a matlab model, the flow velocity and shear stress computations were carried out with the error sources considered.

→ signal analysis with wavelet analysis

Third, the transient term (eq. 1.8) was neglected in all simulations, but a connected syringe pump possesses a slow rise time (Fig. 32a) and a remaining “pulsation error” in steady state (Fig. 32b). In effect, another error adds to the simulation, which is only valid after several ten seconds of the last flow rate change.

Second, the channel height varies in reality as a result of fabrication inaccuracies.

modification of nh<sub>2</sub> with paa and protein like cooh

Contact angle for silanization of surface methods more useful → should be 1st approach for characterization

Anti-Biotin-PE working? BNF-Dextran-Streptavidin unspecific binding? electrostatic surface interaction evidence covalent binding?

gas bubbles, adsorption decrease, tubing exchange activity of protein

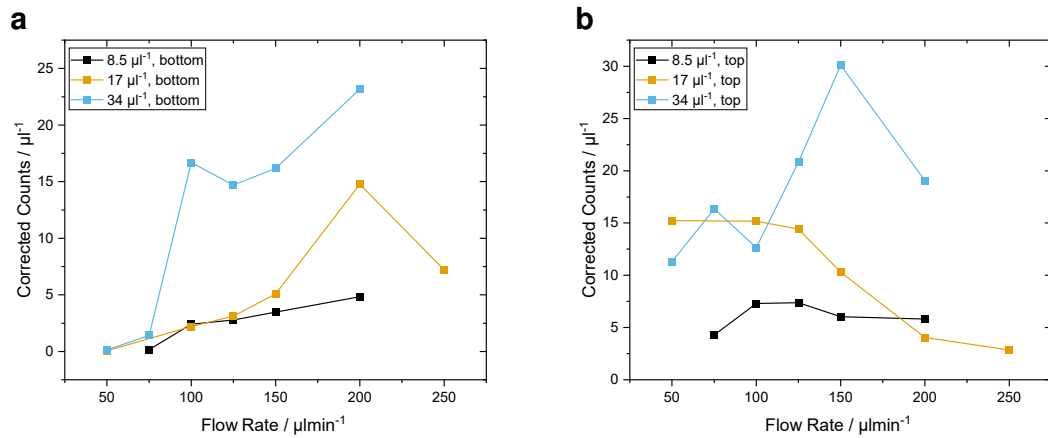
bead rolling with biotin-cooh, biotin-nh<sub>2</sub>, plain-cooh, plain-nh<sub>2</sub> → velocity correction

factor

concentration of beads in differential setup too high, maybe better results with lower.

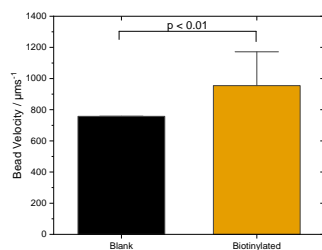
## 6. Outlook

## 7. Appendix



**Figure 34: Measured Bead Velocity**

Not sure what to say about velocity itself. Maybe remove completely,  $p < 0.01$



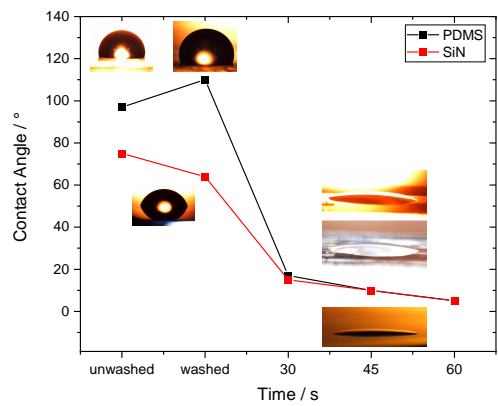


**Figure 35: Hydrophobicity Analysis of PDMS under Plasma Exposure**

For an optimal plasma bond to glass,  $\text{Si}_3\text{N}_4$  and PDMS, the contact angle was measured after treatment. The initial decrease until 45 s declares the optimum around this time. Longer times should be avoided consequently to prohibit further surface damages by reactive ions.

# List of Figures

## Figure 1 Particle Drag and Lift Behavior

(a) Bulk Drag: Force acts on a particle caused by the displacement of fluid stream lines. (b) Wall-lift Drag Force: In a special case of drag, where streamlines cannot be displaced further, a pressure gradient forms in front of the sphere. This forces a motion directed perpendicularly from the wall. (c) Shear-induced force: The curvature of the flow profile exhibits a translation and rotation due to inhomogeneously distributed shear on the surface.[11]..... 6

## Figure 2 Particle Rotation Behavior

(a) Direction of rotation of a sphere settling in eccentric position between parallel walls. (b) Direction of rotation of a sphere settling in the presence of a single plane wall far from the other side.[10]..... 7

## Figure 3 Magnus Effect on a Particle in Laminar Flow

The intrinsic rotation of a particle inside a laminar flow field causes a pressure gradient to the side whose tangential rotation vector is parallel to the stream lines. ..... 9

## Figure 4 Rolling Mechanics of a Sphere

Penetration model of a sphere with radius  $r$  adapted from Azad and Featherstone [25] and Waters and Guduru [26]. The top body moves into the elastic bottom body for an approach ( $z$ ) and a contact area  $\pi a^2$ . 12

## Figure 5 Membrane Adhesion and Detachment Models

**a** Adhesion Model after Dembo et al. [29]: Every interaction is viewed as spring-damper-model in superposition. **b** Surface Coverage Assay Model: In a stochastic approach, analyte molecules and their interactions are modeled between a planar and a spherical surface. Adapted from Wu and Voldman [9] ..... 14

**Figure 6 Different Substrate Surfaces: Glass, PDMS and Si<sub>3</sub>N<sub>4</sub>**

Surface groups and internal structure of quartz glass (**a**), PDMS (**b**), and silicon nitride (**c**). After an oxidation step, the methyl groups are converted to hydroxyl. .... 17

**Figure 7 Surface Oxidation and Modification by APTES**

(**a**) Structure of a typical trialkoxysilane, X: hydrolyzable group, R: non-hydrolyzable organic radical, n: methylene chain-length. (**b**) Before the condensation reaction, the oxidized surface has formed hydrogen bonds with water molecules while the silane molecules are in the bulk solution. The hydrolyzed silanol group adsorbs onto the surface and forms hydrogen bridges with the silicon bound oxygen atom. In a condensation reaction, under the loss of water, a covalent bond to the surface forms. After the SAM assembly the surface is saturated with a covalent-bound, crosslinked silane film.[58] (**c**) Proposed oxidation of Si<sub>3</sub>N<sub>4</sub> with HF: Due to similar activation energies water can displace HF in a competitive manner effectively above a temperature above 70 °C. 19

**Figure 8 Carboxyl bead modification with EDC/NHS**

The carboxy groups bead are activated with EDC to an active O-acylisourea intermediate. This can then either be nucleophilicly attacked by a primary amine of the amine-PEG<sub>2</sub>-biotin reactant or - due to its instability - hydrolzed back to a regenerated carboxyl surface. A present NHS-ester can also displace the O-acylisourea to form a considerably more stable intermediate which then itself reacts with any primary amine..... 21

**Figure 9 Functional Structures of Biotin and Streptavidin**

(**a**) Two- and three dimensional chemical structure of the biotin molecule. (**b**) Homotetrameric streptavidin with four subunits and four bound biotin-ligands. The molecule is attached with the anchor point at one terminus to a surface.[75]..... 23

**Figure 10 Overview over the MRCyte Sensor Setup**

(a) Microfluidic outlet connection to waste reservoir. (b) Imprinted channel width. (c) Microfluidic inlet connection to syringe pump. (d) Magnetophoretic focusing region, not visible in this picture. (e) GMR-sensor region, the supply and bridge balancing traces are visible. (f) Gold bondpad: In order to connect the silicon sensor chip with the breakout PCB, wedge bonds from the chip pads to the PCB pads are forged. (g) Through hole plating for the connection to the lock-in via jumper cables or a soldered connector plug. (h) Typical signal processing flow of a lock-in. The reference signal  $V_r(t)$  is splitted and mixed with the input signal with a phase difference of  $0^\circ$  and  $90^\circ$ . Then, both signals are low-pass filtered and sampled by an analog-to-digital converter (ADC). (i) Accordingly, in a digital signal processing (DSP) device the input signal is digitally converted beforehand, which in turn requires a highly sensitive and fast ADC. In contrast, DSP is more accurate and allows for software-controllable technical opportunities. (j) GMR-sensor bridge circuit inside the microfluidic channel. On the left hand side, magnetophoretic focusing structures are visible. On the right hand side, four Wheatstone bridges on a compliant ground plane can be observed. .... 25

**Figure 11 Here comes a nice drawing from the stacked pcb setup..... 32**

**Figure 12 Gating Strategy for Biotinylated Beads**

a, In the forward-side-scatter plot, the general bead population with high side scatter is selected from the background. b, Single beads are differentiated by their sphericity, their ratio of height:area in the side scatter. Points on the line through the origin are spherical. c, The stained subset in the respective color is now selected and the MFI as well as the CV is computed. .... 38

### Figure 13 Particle Coverage Simulation

(a) Dimensions of the GMR Wheatstone bridge sensor: Distance d between both variable bridges (green), width w of a GMR-sensor, length L of a sensor. (b) Scheme of single cell simulation: The ideal magnetic dipole in the geometric center of a sphere (●) causes a signal deviation from the real cell signal with magnetic moment distributed on the cell surface. (●) (c) Signal shapes of different angles of two-particle aggregates lead to differing signal shapes. ..... 42

### Figure 14 Coverage Dependent Signal Correlation

MNP coverage of a sphere with 4  $\mu\text{m}$  (a, b) and 8  $\mu\text{m}$  diameter (c, d) covered by magnetic particles ranging from 20 nm to 2000 nm. A cross-correlation increase which is inversely proportional to the MNP size can be observed. ..... 44

### Figure 15 Maximal Cross-Correlation Differences

(a) Mean coverage at 99 % for 4  $\mu\text{m}$  and 8  $\mu\text{m}$  spheres. A negative dependency on the MNP size can be explained by the ratio of magnetic momentum per unit surface and its homogeneous distribution across the whole surface. (b) Relative correlation error between 4  $\mu\text{m}$  and 8  $\mu\text{m}$  spheres with a quadratic fit. The quadratic behavior could be related to the relative surface area which can occupied by magnetic momentum. (Adj.  $R^2 = 0.992\,09$ ) ..... 45

### Figure 16 Signal Correlation between Two-Cell Aggregates At Shifting Angles

Two-Sphere aggregates are covered with 200 nm MNPs and simulated flowing over the sensor at differing respective angles. The SEM indicates a difference in cross-correlation of three truly random MNP distributions. For low yaw angles and high coverages, the aggregate's signal reflects rather two single dipoles in superposition than one quite homogeneous dipole. This causes a high signal deviation from the reference and thus a low degree of correlation. ..... 46

**Figure 17 Flow Field and Shear Stress Simulation of the utilized Microchannel**

Flow (a) and vertical shear (c) field inside the microchannel with dimensions ( $w \times h \times L$ )  $700 \mu\text{m} \times 150 \mu\text{m} \times 15800 \mu\text{m}$  for a flow rate of  $80 \mu\text{L min}^{-1}$  and with neglected tubing effects. The subplots on the right and top side show the mean horizontal and vertical profile in  $0 \mu\text{m}$  width and  $75 \mu\text{m}$  height, respectively. (vertical: —, horizontal: —) Due to the no-slip condition, the velocity at the walls equals zero and the shear is maximal. The maximum of the Hagen-Poiseuille profile is located in the channel center. Over the cross-section the mean flow velocity  $\bar{u}$  equals  $12670.83 \mu\text{m s}^{-1}$ . Resultingly, the net horizontal viscous shear  $\tau_{viscous} = \frac{\partial u}{\partial z}$  cancels out over the whole channel cross-section. Flow (d) and vertical shear (d) field acting on a  $8 \mu\text{m}$  diameter bead on the channel bottom. The mean fluid velocity trapped by the bead profile results in  $\bar{u}_p = 2241.59 \mu\text{m s}^{-1}$ , whereas the viscous shear strains with  $\tau_{viscous} = 4.93 \text{ dyne cm}^{-2}$  ..... 48

**Figure 18 Amine Bead Modification with Sulfo-NHS-Biotin**

An amine terminated bead brought into reaction with sulfo-NHS-biotin. Both form an amide linkage and bind biotin covalently to the surface. As byproduct the sulfo-NHS-ester splits off..... 51

**Figure 19 Titration of Biofunctional Molecules on  $8 \mu\text{m}$  Particles**

Titration curves of NHS-biotin (a), Amin-PEG<sub>2</sub>-Biotin (b), and Anti-IgG1 (c) with their respective Hill fits. The corresponding fit parameters as well as the goodness factor are shown in Table 4a. (d) Stability analysis of functionalized carboxyl and amine beads over 12 days. The carboxylate particles show a exponential decrease with a half-life of 1.43 days as determined by the exponential fit. The respective parameters are shown in Table 4b. ..... 52

## Figure 20 Example Signal of Magnetic Measurement

Signals generated from the Wheatstone bridge sensor setup feature a certain shape which allows for several measures. In case the overall signal stream carries a constant or linear offset, it is scaled to the means before and after the detected peak pattern. ([Mean1](#), [Mean2](#)) The x- and y-positions of each peak are denominated by [B1-4](#) and [Amp1-4](#), respectively. The crossings of the signal through the linear connection of both means are denominated by [n1-3](#) (in the figure by ●). Further, the difference between the equally oriented peaks [B3-B1](#) and [B4-B2](#) give a measure for the homogeneous movement of the measured object and are called [A1](#) and [A2](#) each. From these values the overall velocity  $v$  can be approximated because the  $d_{GMR}$  and  $f_s$  is fixed precisely. Analogously, the magnetic diameter of a dipole is computed by the mean of the differences [B2-B1](#) and [B4-B3](#). ..... 56

## Figure 21 Bead Loss Evaluation in Connectors

Bead concentrations measured in equal volumes in the flow cytometer after being pumped through a syringe or a syringe with connected tubing. The blank sample was measured directly from the stock solution. Additionally, electrostatic and surface tension related effects were resolved by the usage of different buffers and bead surfaces. ..... 56

## Figure 22 Error Sources in Concentration Measurements

(a) Robustness evaluation of the both correction factors  $C_{const}$  and  $C_{velocity}$  for protein coated surfaces. The mean and SEM of plain and biotinylated measurements show a high deviation from physically reasonable expectations when corrected for the velocity (right). In contrast,  $C_{const}$  can intrinsically correct only well below 100 %. (b) Mean and SEM of a fit-corrected bead capture experiment with several error sources. Initially, the magnetophoretic structures have to be filled and thus decrease the plain count for the first 100  $\mu\text{L}$ . (—) Additionally, the high deviation offsets the correction factor so that the stable measurement from 100  $\mu\text{L}$  to 200  $\mu\text{L}$  lies now above the ideal reference. In contrast, the biotinylated beads are captured by the surface functionalization and hence a very low concentration is measured. However, a steep rise with pulsations can be observed when the surface is saturated with beads and the particles begin to flow over the sensor in bursts. (—) The abrupt decline to the end of the measured volume is most probably related to sedimentation effects inside the emptying syringe..... 58

## Figure 23 Absolute Concentration Measurements

(a) Mean and standard deviation of the concentration measurement from three independent measurements. The uncorrected measurement shows a highly reproducible and linear count over the dynamic range of almost two decades. (■) The ideal reference from the flow cytometer is depicted in (—). Correction with  $C_{velocity}$  (—) yields at a factor of 2.261 09 which is 21.7 % more imprecise than  $C_{const}$  at  $2.888\,33 \pm 0.080\,75$ . (■) (b) Mean and SEM of the  $v_c$  estimation from the signal. For higher concentrations, the measured velocity becomes inaccurate thus distorts the correction factor..... 59

**Figure 24 Absolute Concentration Measurement in Blood Samples Under Varying Channel Height**

Velocity corrected concentration measurements for two different blood dilutions and channel heights. While  $C_{velocity}$  works for high channels in all tested concentrations, it does not work for high concentrations in 50 µm high channels. This is probably a result of bead-cell collisions and the resulting path interruption. .... 61

**Figure 25 Bead Coverage Assay with Magnetic Streptavidin Nanoparticles**

Magnetic flow cytometry data from 8 µm polystyrene sphere which were biotinylated in different degrees and subsequently coated with BNF-Dextran-redF-streptavidin 100 nm MNPs(a,b) or SV0050 50 nm streptavidin MNPs (c,d). (a) Signal amplitude of the counts with various flow rates 1. 80 µL min<sup>-1</sup> 2. 40 µL min<sup>-1</sup> 3. 20 µL min<sup>-1</sup> 4. 10 µL min<sup>-1</sup> (b) Reconstructed velocities of the respective populations. The 100 % biotinylation shows plausible velocities, whereas the 68 % sample can either be considered as noisy background or very weakly magnetized particles.(c) Signal amplitude with 80 µL min<sup>-1</sup>. A correlation between biotinylation degree and magnetic momentum can be assumed at a p-value p < 0.1 (d) Velocity distributions of the samples. As postulated, the mean velocities do not differ, moreover, are enveloped by the blank sample. .... 62

**Figure 26 Reproducibility of Concentration Measurements with Saturated Neutravidin Surfaces**

Biological replicates of concentration measurements with the magnetic flow cytometer. The channel surface was modified with 1 mg mL<sup>-1</sup> neutravidin over night. (a) Mean and SEM of  $C_{const}$  adjusted counts for various biotinylation degrees. (b) Time series of the mean from the three measurements on the left. Biotin-beads are captured completely, thus very few counts are detected.(—) The unbiotinylated sample shows the initial ascent due to the in Sec. 4.4.1 discussed error which is related to the filling of the magnetophoretic structures.(—) .... 63

**Figure 27 Hysteresis Calibration for Stacked PCB Setup**

(a) Differential measurement setup: the system comprises of two separately assembled sensor PCBs (b) with nylon spacers (e) between the positional screws. (f) A hole with 3 mm diameter was drilled between the strip lines to connect the top chip outlet to the bottom chip inlet and minimize tubing length thereby. Schematically, a permanent magnet is placed below the bottom PCB.(d) The field line density respectively the area with negligibly differing field vectors is shown in the blue triangle. Because the adjustment is always carried out for a single bridge at once, this causes a systematic error. The magneto-resistive effects of both sensors, calculated from their hystereses, are depicted for top and bottom sensors, respectively. Whereas the hysteresis was optimized for the centered sensor bridge (D or E) on the top sensor in (f), it was optimized for the bottom sensor in (g). Additionally, the height of the nylon spacers was varied from 3 mm to 8 mm but showed no statistical correlation..... 66

**Figure 28 Optimal Differential Counting Flow Rate**

Losses in different buffers and bead surfaces..... 67

**Figure 29 Surface Adsorption Stability of Neutravidin on Si<sub>3</sub>N<sub>4</sub> and Al<sub>2</sub>Ox<sub>3</sub>**

Plate reader measurement with 3 mm x 3 mm Si<sub>3</sub>N<sub>4</sub> and Al<sub>2</sub>Ox<sub>3</sub> samples which were incubated with 100 µg and 10 µg streptavidin-atto488, respectively. The samples were subsequently washed with 200 µL PBS carefully. Fluorescence intensities were corrected with a blank substrate, the autofluorescence of PBS, and normalized eventually. Every surface reaches a mean fluorescence level of 28 % after few washing steps..... 70

**Figure 30 General process chain of chemical surface modification**

Any substrate with various surface groups R (a) is oxidized to exhibit hydroxyl groups.(b). Then a silane SAM is attached (c) and subsequently modified by carbodiimide chemistry with PAA. (d) ..... 70

<b>Figure 31 Optical Bead Capture Assay and Titration Fluorescence Analysis</b>	
(a) Density measurement of captured beads on the covalently functionalized surfaces of PDMS, Si <sub>3</sub> N <sub>4</sub> and glass. PDMS shows the most promising density. (b) Titration of neutravidin on covalently functionalized glass with a subsequent analysis by a bead capture assay. (c) Titration of streptavidin-atto488 on covalently functionalized glass with subsequent fluorescence microscope imaging.....	71
<b>Figure 32 Syringe Pump error sources</b>	
Set flow rate:  , Real Flow Rate:  a Transient step answer of a syringe pump through a microtube with 254 µm inner diameter. b Steady state flow rate error around the desired 5 µL min <sup>-1</sup> dispensing rate. A sinusoidal behaviour caused by the microstepping can be observed. [88] .....	73
<b>Figure 33 Flow Rate Dependency of Differential Counting Setup</b>	
(a) Optimized for top sensor (b) Optimized for bottom sensor .....	76
<b>Figure 34 Measured Bead Velocity</b>	
Not sure what to say about velocity itself. Maybe remove completely, p < 0.01 .....	76
<b>Figure 35 Hydrophobicity Analysis of PDMS under Plasma Exposure</b>	
For an optimal plasma bond to glass, Si <sub>3</sub> N <sub>4</sub> and PDMS, the contact angle was measured after treatment. The initial decrease until 45 s declares the optimum around this time. Longer times should be avoided consequently to prohibit further surface damages by reactive ions. ....	77

# List of Tables

Table 1 Wirebonding Parameters.....	27
Table 2 Properties of the used microbeads and MNPs .....	37
<b>Table 3 Magnetic Simulation Parameters</b>	
Constants used inside the framework for the simulation of the magnetic field inside the GMR Wheatstone half bridge. The volume magnetization was adapted according to the simulated particle size.....	43
<b>Table 4 Fit Parameters of Biotinylation</b>	
(a) Coefficients for the Hill fits in Figs. 19a to 19c (b) Exponential fit coef- ficients for the stability analysis in Fig. 19d .....	52

# Bibliography

- [1] Michael Helou. "Magnetic Flow Cytometry". PhD Thesis. 2014.
- [2] Mathias Reisbeck. "Integration und quantitative Analyse in der magnetischen Durchflusszytometrie". Thesis. 2019.
- [3] Esther Räth. "Affinity-based Cell Rolling Assays in Magnetic Flow Cytometry". Thesis. 2020.
- [4] Johann Brenner. "Superparamagnetic Nanoparticles in Picoliter Droplets for Measurements with Spin Valves". Bachelor Thesis. 2018.
- [5] Brian Kirby. *Micro- and Nanoscale Fluid Mechanics*. 2010. ISBN: 9780511760723. DOI: 10.1017/cbo9780511760723.
- [6] Henrik Bruus. *Theoretical Microfluidics*. Technical University of Denmark: Oxford University Press, 2008. ISBN: 978–0–19–923508–7.
- [7] Hyungoo Lee and S. Balachandar. "Drag and lift forces on a spherical particle moving on a wall in a shear flow at finite  $Re$ ". In: *Journal of Fluid Mechanics* 657 (2010), pp. 89–125. ISSN: 0022-1120. DOI: 10.1017/s0022112010001382.
- [8] Cheng Dong and Xiao X. Lei. "Biomechanics of cell rolling: shear flow, cell-surface adhesion, and cell deformability". In: *Journal of Biomechanics* 33.1 (2000), pp. 35–43. ISSN: 00219290. DOI: 10.1016/s0021-9290(99)00174-8.
- [9] Dan Wu and Joel Voldman. "An integrated model for bead-based immunoassays". In: *Biosensors and Bioelectronics* 154 (2020). ISSN: 09565663. DOI: 10.1016/j.bios.2020.112070.
- [10] D. Di Carlo et al. "Continuous inertial focusing, ordering, and separation of particles in microchannels". In: *Proceedings of the National Academy of Sciences* 104.48 (2007), pp. 18892–18897. ISSN: 0027-8424. DOI: 10.1073/pnas.0704958104.
- [11] Joseph M. Martel and Mehmet Toner. "Inertial Focusing in Microfluidics". In: *Annual Review of Biomedical Engineering* 16.1 (2014). PMID: 24905880, pp. 371–396. DOI: 10.1146/annurev-bioeng-121813-120704.
- [12] Howard Brenner. "The slow motion of a sphere through a viscous fluid towards a plane surface". In: *Chemical Engineering Science* 16.3-4 (Dec. 1961), pp. 242–251. DOI: 10.1016/0009-2509(61)80035-3.

- [13] John Happel and Howard Brenner. *Low Reynolds number hydrodynamics*. Mechanics of fluids and transport processes. 1981. ISBN: 978-94-009-8352-6. DOI: 10.1007/978-94-009-8352-6.
- [14] Rune Barnkob et al. “Acoustic radiation- and streaming-induced microparticle velocities determined by microparticle image velocimetry in an ultrasound symmetry plane”. In: *Physical Review E* 86.5 (2012). ISSN: 1539-3755. DOI: 10.1103/physreve.86.056307.
- [15] Lanying Zeng et al. “Forces on a finite-sized particle located close to a wall in a linear shear flow”. In: *Physics of Fluids* 21.3 (2009), p. 033302. ISSN: 1070-6631. DOI: 10.1063/1.3082232.
- [16] Jun Zhang et al. “Fundamentals and applications of inertial microfluidics: a review”. In: *Lab on a Chip* 16.1 (2016), pp. 10–34. ISSN: 1473-0197. DOI: 10.1039/c5lc01159k.
- [17] Ewa Guzniczak et al. “Deformability-induced lift force in spiral microchannels for cell separation”. In: *Lab on a Chip* 20.3 (2020), pp. 614–625. ISSN: 1473-0197. DOI: 10.1039/c9lc01000a.
- [18] Albert J. Mach and Dino Di Carlo. “Continuous scalable blood filtration device using inertial microfluidics”. In: *Biotechnology and Bioengineering* 107.2 (June 2010), pp. 302–311. DOI: 10.1002/bit.22833.
- [19] Robin Fåhræus. “THE SUSPENSION STABILITY OF THE BLOOD”. In: *Physiological Reviews* 9.2 (Apr. 1929), pp. 241–274. DOI: 10.1152/physrev.1929.9.2.241.
- [20] Robin Fåhræus and Torsten Lindqvist. “THE VISCOSITY OF THE BLOOD IN NARROW CAPILLARY TUBES”. In: *American Journal of Physiology-Legacy Content* 96.3 (Mar. 1931), pp. 562–568. DOI: 10.1152/ajplegacy.1931.96.3.562.
- [21] G. Segré and A. Silberberg. “Radial Particle Displacements in Poiseuille Flow of Suspensions”. In: *Nature* 189.4760 (Jan. 1961), pp. 209–210. DOI: 10.1038/189209a0.
- [22] Rachid Chebbi. “Dynamics of blood flow: modeling of the Fåhræus–Lindqvist effect”. In: *Journal of Biological Physics* 41.3 (Feb. 2015), pp. 313–326. DOI: 10.1007/s10867-015-9376-1.
- [23] Koffi Espoir Koumi, Thibaut Chaise, and Daniel Nelias. “Rolling contact of a rigid sphere/sliding of a spherical indenter upon a viscoelastic half-space containing

- an ellipsoidal inhomogeneity". In: *Journal of the Mechanics and Physics of Solids* 80 (July 2015), pp. 1–25. DOI: 10.1016/j.jmps.2015.04.001.
- [24] Bo Jacobson and Joost J. Kalker, eds. *Rolling Contact Phenomena*. Springer Vienna, 2000. DOI: 10.1007/978-3-7091-2782-7.
- [25] M. Azad and R. Featherstone. "Modeling the contact between a rolling sphere and a compliant ground plane". In: 2010.
- [26] Julie F. Waters and Pradeep R. Guduru. "Mode-mixity-dependent adhesive contact of a sphere on a plane surface". In: *Proceedings of the Royal Society A: Mathematical, Physical and Engineering Sciences* 466.2117 (Dec. 2009), pp. 1303–1325. DOI: 10.1098/rspa.2009.0461.
- [27] Gokul P. Krishnan and David T. Leighton. "Inertial lift on a moving sphere in contact with a plane wall in a shear flow". In: *Physics of Fluids* 7.11 (1995), pp. 2538–2545. ISSN: 1070-6631. DOI: 10.1063/1.868755.
- [28] R. P. McEver and C. Zhu. "Rolling cell adhesion". In: *Annu Rev Cell Dev Biol* 26 (2010), pp. 363–96. ISSN: 1530-8995 (Electronic) 1081-0706 (Linking). DOI: 10.1146/annurev.cellbio.042308.113238.
- [29] M. Dembo et al. "The reaction-limited kinetics of membrane-to-surface adhesion and detachment". In: *Proceedings of the Royal Society of London. Series B. Biological Sciences* 234.1274 (1997), pp. 55–83. ISSN: 0080-4649 2053-9193. DOI: 10.1098/rspb.1988.0038.
- [30] Pavel I. Kitov and David R. Bundle. "On the Nature of the Multivalency Effect: A Thermodynamic Model". In: *Journal of the American Chemical Society* 125.52 (2003), pp. 16271–16284. ISSN: 0002-7863. DOI: 10.1021/ja038223n.
- [31] Krishna K. Sarangapani et al. "Low Force Decelerates L-selectin Dissociation from P-selectin Glycoprotein Ligand-1 and Endoglycan\*". In: *Journal of Biological Chemistry* 279.3 (2004), pp. 2291–2298. ISSN: 0021-9258. DOI: <https://doi.org/10.1074/jbc.M310396200>.
- [32] Bryan T. Marshall et al. "Direct observation of catch bonds involving cell-adhesion molecules". In: *Nature* 423.6936 (2003), pp. 190–193. ISSN: 0028-0836. DOI: 10.1038/nature01605.
- [33] H. Cumhur Tekin, Matteo Cornaglia, and Martin A. M. Gijs. "Attomolar protein detection using a magnetic bead surface coverage assay". In: *Lab on a Chip* 13.6 (2013), p. 1053. ISSN: 1473-0197. DOI: 10.1039/c3lc41285g.

- [34] Li-Chong Xu, James W. Bauer, and Christopher A. Siedlecki. "Proteins, platelets, and blood coagulation at biomaterial interfaces". In: *Colloids and Surfaces B: Biointerfaces* 124 (2014), pp. 49–68. ISSN: 0927-7765. DOI: 10.1016/j.colsurfb.2014.09.040.
- [35] S. Prentner et al. "Effects of channel surface finish on blood flow in microfluidic devices". In: *Microsystem Technologies* 16.7 (2010), pp. 1091–1096. ISSN: 0946-7076. DOI: 10.1007/s00542-009-1004-1.
- [36] Sushanta K. Mitra and Auro Ashish Saha. "Surface Modification, Methods". In: *Encyclopedia of Microfluidics and Nanofluidics*. Springer US, 2014, pp. 1–9. DOI: 10.1007/978-3-642-27758-0\_1503-2.
- [37] R.A. Williams and H.W. Blanch. "Covalent immobilization of protein monolayers for biosensor applications". In: *Biosensors and Bioelectronics* 9.2 (1994), pp. 159–167. ISSN: 0956-5663. DOI: 10.1016/0956-5663(94)80108-8.
- [38] William Putzbach and Niina Ronkainen. "Immobilization Techniques in the Fabrication of Nanomaterial-Based Electrochemical Biosensors: A Review". In: *Sensors* 13.4 (2013), pp. 4811–4840. ISSN: 1424-8220. DOI: 10.3390/s130404811.
- [39] R. Funari et al. "Single Molecule Characterization of UV-Activated Antibodies on Gold by Atomic Force Microscopy". In: *Langmuir* 32.32 (2016), pp. 8084–8091. ISSN: 0743-7463. DOI: 10.1021/acs.langmuir.6b02218.
- [40] A. Ymeti et al. "Integration of microfluidics with a four-channel integrated optical Young interferometer immunosensor". In: *Biosensors and Bioelectronics* 20.7 (2005), pp. 1417–1421. ISSN: 0956-5663. DOI: <https://doi.org/10.1016/j.bios.2004.04.015>.
- [41] María-José Bañuls, Rosa Puchades, and Ángel Maquieira. "Chemical surface modifications for the development of silicon-based label-free integrated optical (IO) biosensors: A review". In: *Analytica Chimica Acta* 777 (2013), pp. 1–16. ISSN: 0003-2670. DOI: 10.1016/j.aca.2013.01.025.
- [42] N. Lange. "Selective Chemical Modification of Silicon Nitride Surfaces for Novel Biosensor Application". Thesis. 2017. DOI: <http://dx.doi.org/10.17169/refubium-11275>.
- [43] Marine Brunet et al. "Etching and Chemical Control of the Silicon Nitride Surface". In: *ACS Applied Materials & Interfaces* 9.3 (2017), pp. 3075–3084. ISSN: 1944-8244. DOI: 10.1021/acsami.6b12880.

- [44] K. Sekine et al. "Highly robust ultrathin silicon nitride films grown at low-temperature by microwave-excitation high-density plasma for giga scale integration". In: *IEEE Transactions on Electron Devices* 47.7 (2000), pp. 1370–1374. ISSN: 0018-9383. DOI: 10.1109/16.848279.
- [45] M. K. Chaudhury and G. M. Whitesides. "Correlation Between Surface Free Energy and Surface Constitution". In: *Science* 255.5049 (1992), pp. 1230–1232. ISSN: 0036-8075. DOI: 10.1126/science.255.5049.1230.
- [46] H. Hillborg et al. "Crosslinked polydimethylsiloxane exposed to oxygen plasma studied by neutron reflectometry and other surface specific techniques". In: *Polymer* 41.18 (2000), pp. 6851–6863. ISSN: 0032-3861. DOI: [https://doi.org/10.1016/S0032-3861\(00\)00039-2](https://doi.org/10.1016/S0032-3861(00)00039-2).
- [47] A. N. Ermakov et al. "The thermodynamic characteristics of hydrogen peroxide in H<sub>2</sub>SO<sub>4</sub>-H<sub>2</sub>O solutions". In: *Russian Journal of Physical Chemistry A* 80.12 (2006), pp. 1895–1901. ISSN: 0036-0244. DOI: 10.1134/s0036024406120041.
- [48] Masatomo Yashima, Yoshiaki Ando, and Yasunori Tabira. "Crystal Structure and Electron Density of  $\alpha$ -Silicon Nitride: Experimental and Theoretical Evidence for the Covalent Bonding and Charge Transfer". In: *The Journal of Physical Chemistry B* 111.14 (2007), pp. 3609–3613. ISSN: 1520-6106. DOI: 10.1021/jp0678507.
- [49] Marine Brunet et al. "Etching and Chemical Control of the Silicon Nitride Surface". In: *ACS Applied Materials & Interfaces* 9.3 (2017), pp. 3075–3084. ISSN: 1944-8244. DOI: 10.1021/acsami.6b12880.
- [50] Ahmed Arafat et al. "Covalent Biofunctionalization of Silicon Nitride Surfaces". In: *Langmuir* 23.11 (2007), pp. 6233–6244. ISSN: 0743-7463 1520-5827. DOI: 10.1021/la7007045.
- [51] Michel Rosso. *Modification of Silicon Nitride and Silicon Carbide Surfaces for Food and Biosensor Applications*. 2009. ISBN: 978-90-8585-379-4.
- [52] David J. Michalak et al. "Nanopatterning Si(111) surfaces as a selective surface-chemistry route". In: *Nature Materials* 9.3 (2010), pp. 266–271. ISSN: 1476-1122. DOI: 10.1038/nmat2611.
- [53] L. H. Liu et al. "Surface etching, chemical modification and characterization of silicon nitride and silicon oxide-selective functionalization of Si<sub>3</sub>N<sub>4</sub> and SiO<sub>2</sub>". In: *J Phys Condens Matter* 28.9 (2016), p. 094014. ISSN: 1361-648X (Electronic) 0953-8984 (Linking). DOI: 10.1088/0953-8984/28/9/094014.

- [54] Johan Gustavsson et al. "Surface modifications of silicon nitride for cellular biosensor applications". In: *Journal of Materials Science: Materials in Medicine* 19.4 (2008), pp. 1839–1850. ISSN: 0957-4530. DOI: 10.1007/s10856-008-3384-7.
- [55] A. Pizzi and K.L. Mittal. *Handbook of Adhesive Technology, Revised and Expanded*. Taylor and Francis, 2003. ISBN: 9780203912225.
- [56] Brian Seed. "Silanizing Glassware". In: *Current Protocols in Cell Biology* 8.1 (2000), A.3E.1–A.3E.2. ISSN: 1934-2500. DOI: 10.1002/0471143030.cba03es08.
- [57] GELEST. *Silane Coupling Agents*. Catalog. 2014.
- [58] Hossein Khanjanzadeh et al. "Application of surface chemical functionalized cellulose nanocrystals to improve the performance of UF adhesives used in wood based composites - MDF type". In: *Carbohydrate Polymers* 206 (2019), pp. 11–20. ISSN: 0144-8617. DOI: <https://doi.org/10.1016/j.carbpol.2018.10.115>.
- [59] K. C. Andree et al. "Capture of Tumor Cells on Anti-EpCAM-Functionalized Poly(acrylic acid)-Coated Surfaces". In: *ACS Appl Mater Interfaces* 8.23 (2016), pp. 14349–56. ISSN: 1944-8252 (Electronic) 1944-8244 (Linking). DOI: 10.1021/acsami.6b01241.
- [60] Solange Magalhães et al. "Brief Overview on Bio-Based Adhesives and Sealants". In: *Polymers* 11.10 (2019), p. 1685. ISSN: 2073-4360. DOI: 10.3390/polym11101685.
- [61] Robert M. Pasternack, Sandrine Rivillon Amy, and Yves J. Chabal. "Attachment of 3-(Aminopropyl)triethoxysilane on Silicon Oxide Surfaces: Dependence on Solution Temperature". In: *Langmuir* 24.22 (2008), pp. 12963–12971. ISSN: 0743-7463. DOI: 10.1021/la8024827.
- [62] Nina Bjørk Arnfinnsdottir et al. "Impact of Silanization Parameters and Antibody Immobilization Strategy on Binding Capacity of Photonic Ring Resonators". In: *Sensors* 20.11 (2020). ISSN: 1424-8220. DOI: 10.3390/s20113163.
- [63] M. J. Banuls et al. "Selective chemical modification of silicon nitride/silicon oxide nanostructures to develop label-free biosensors". In: *Biosens Bioelectron* 25.6 (2010), pp. 1460–6. ISSN: 1873-4235 (Electronic) 0956-5663 (Linking). DOI: 10.1016/j.bios.2009.10.048.
- [64] Dean W. Sindorf and Gary E. Maciel. "Solid-state NMR studies of the reactions of silica surfaces with polyfunctional chloromethylsilanes and ethoxymethylsilanes". In: *Journal of the American Chemical Society* 105.12 (1983), pp. 3767–3776. ISSN: 0002-7863. DOI: 10.1021/ja00350a003.

- [65] *Bioconjugate Techniques*. Elsevier, 2013. DOI: 10.1016/c2009-0-64240-9.
- [66] D.G. Hoare and D.E. Koshland. “A Method for the Quantitative Modification and Estimation of Carboxylic Acid Groups in Proteins”. In: *Journal of Biological Chemistry* 242.10 (May 1967), pp. 2447–2453. DOI: 10.1016/s0021-9258(18)95981-8.
- [67] ThermoFisher Scientific. *User Guide: NHS and Sulfo-NHS*. 2021.
- [68] D. W. Woolley and L. G. Longsworth. “Isolation of an antibiotic factor from egg white.” In: *Journal of Biological Chemistry* 142 (1942), pp. 285–290.
- [69] T. Sano and C. R. Cantor. “Expression of a cloned tavidin gene in Escherichia coli.” In: *Proceedings of the National Academy of Sciences* 87.1 (1990), pp. 142–146. ISSN: 0027-8424. DOI: 10.1073/pnas.87.1.142.
- [70] Claire E Chivers et al. “A streptavidin variant with slower biotin dissociation and increased mechanostability”. In: *Nature Methods* 7.5 (2010), pp. 391–393. ISSN: 1548-7091. DOI: 10.1038/nmeth.1450.
- [71] P. Weber et al. “Structural origins of high-affinity biotin binding to streptavidin”. In: *Science* 243.4887 (1989), pp. 85–88. ISSN: 0036-8075. DOI: 10.1126/science.2911722.
- [72] Bruno Miroux and John E. Walker. “Over-production of Proteins in Escherichia coli: Mutant Hosts that Allow Synthesis of some Membrane Proteins and Globular Proteins at High Levels”. In: *Journal of Molecular Biology* 260.3 (1996), pp. 289–298. ISSN: 0022-2836. DOI: 10.1006/jmbi.1996.0399.
- [73] Shuichi Miyamoto and Peter A. Kollman. “Absolute and relative binding free energy calculations of the interaction of biotin and its analogs with streptavidin using molecular dynamics/free energy perturbation approaches”. In: *Proteins: Structure, Function, and Bioinformatics* 16.3 (1993), pp. 226–245. ISSN: 0887-3585. DOI: 10.1002/prot.340160303.
- [74] H., B. Heymann, and P. Tavan. “Ligand Binding: Molecular Mechanics Calculation of the Streptavidin-Biotin Rupture Force”. In: *Science* 271.5251 (1996), pp. 997–999. ISSN: 0036-8075. DOI: 10.1126/science.271.5251.997.
- [75] Steffen M. Sedlak et al. “Streptavidin/biotin: Tethering geometry defines unbinding mechanics”. In: *Science Advances* 6.13 (2020). DOI: 10.1126/sciadv.aay5999.
- [76] Carmen-Gabriela Stefanita. *Magnetism*. Springer Berlin Heidelberg, 2012. DOI: 10.1007/978-3-642-22977-0.

- [77] Alberto P. Guimarães. *Principles of Nanomagnetism*. Springer International Publishing, 2017. DOI: 10.1007/978-3-319-59409-5.
- [78] K. H. J. Buschow and F. R. de Boer. *Physics of Magnetism and Magnetic Materials*. Springer US, 2003. DOI: 10.1007/b100503.
- [79] Hugo Dr. van den Berg. “Magnetoresistance sensor using multi-layer system - has intermediate layer between measuring layer and bias layer with perpendicular magnetisation”. DE4232244A1. May 14, 1998.
- [80] Michael Helou et al. “Time-of-flight magnetic flow cytometry in whole blood with integrated sample preparation”. In: *Lab on a Chip* 13.6 (2013), p. 1035. DOI: 10.1039/c3lc41310a.
- [81] Mathias Reisbeck et al. “Magnetic fingerprints of rolling cells for quantitative flow cytometry in whole blood”. In: *Scientific Reports* 6.1 (Sept. 2016). DOI: 10.1038/srep32838.
- [82] *Principles of lock-in detection and the state of the art*. 2016. URL: <https://www.zhinst.com/others/en/resources/principles-of-lock-in-detection>.
- [83] Rojda Hicsanmaz. “Setup and Assessment of Laser Lithography for the Fabrication and Integration of Biosensor and Microfluidic Devices”. Technical University Munich, 2020.
- [84] Walter J. Dressick et al. “Covalent Binding of Pd Catalysts to Ligating Self-Assembled Monolayer Films for Selective Electroless Metal Deposition”. In: *Journal of the Electrochemical Society* 141.1 (1994), pp. 210–220. ISSN: 0013-4651. DOI: 10.1149/1.2054686.
- [85] Johannes Schindelin et al. “Fiji: an open-source platform for biological-image analysis”. In: *Nature Methods* 9.7 (2012), pp. 676–682. ISSN: 1548-7091. DOI: 10.1038/nmeth.2019.
- [86] A.F. Stalder et al. “A Snake-Based Approach to Accurate Determination of Both Contact Points and Contact Angles”. In: *Colloids And Surfaces A: Physicochemical And Engineering Aspects* 286.1-3 (Sept. 2006), pp. 92–103.
- [87] Bruce Alberts et al. *Molecular Biology of the Cell*. ISBN: 0815345240.
- [88] *Syringe pumps*. 2021. URL: <https://www.fluigent.com/resources/microfluidic-expertise/what-is-microfluidic/system-comparison-for-microfluidic-applications/>.

# Statement

I declare that I have authored this thesis independently, that I have not used other than the declared sources / resources, and that I have explicitly marked all material which has been quoted either literally or by content from the used sources.

---

Munich, December 4<sup>th</sup>, 2020, Signature